

Spring 2022

Catalytic Cracking of Oxygenated Polymer Waste Via Zeolite Catalysts

Andrew Jaeschke

Follow this and additional works at: <https://scholarcommons.sc.edu/etd>

 Part of the [Chemical Engineering Commons](#)

Recommended Citation

Jaeschke, A. (2022). *Catalytic Cracking of Oxygenated Polymer Waste Via Zeolite Catalysts*. (Master's thesis). Retrieved from <https://scholarcommons.sc.edu/etd/6724>

This Open Access Thesis is brought to you by Scholar Commons. It has been accepted for inclusion in Theses and Dissertations by an authorized administrator of Scholar Commons. For more information, please contact digres@mailbox.sc.edu.

CATALYTIC CRACKING OF OXYGENATED POLYMER WASTE VIA ZEOLITE CATALYSTS

by

Andrew Jaeschke

Bachelor of Science
University of Kansas, 2019

Submitted in Partial Fulfillment of the Requirements

For the Degree of Master of Science in

Chemical Engineering

College of Engineering and Computing

University of South Carolina

2022

Accepted by:

Jochen Lauterbach, Director of Thesis

Alex Katz, Reader

Andreas Heyden, Reader

Monirosadat Sadati, Reader

Tracey L. Weldon, Interim Vice Provost and Dean of the Graduate School

© Copyright by Andrew Jaeschke, 2022
All Rights Reserved.

ABSTRACT

Plastic recycling has been a prevalent issue since the commercialization of plastics due to lack of adoption and insufficient technology. There are many different types of plastics used in modern day society; however, majority of recycling efforts are focused solely on polyethylene terephthalate (PET) and polyethylene plastics. Some of these overlooked plastics include polyols and polyurethanes, which can be found in a variety of applications including furniture stuffing, adhesives, and insulation foams. Recently, plastic research has turned to catalytic cracking units as a means of plastic recyclability. Catalytic cracking of hydrocarbons is a field dominated by zeolites catalysts, especially ZSM-5. Despite a heavy research focus on the catalytic cracking reactions of PET and polyethylene, there exists preliminary research efforts in the field of pyrolysis and catalytic cracking of polyols and polyurethanes. As such, a reactor and analytical system was built to investigate the catalytic cracking of polypropylene glycol (PPG) using zeolite catalysts. Based on preliminary testing, the primary seven products of interest were propionaldehyde; 1,4-dioxane, 2,5-dimethyl; 1-propanol; 1,3-dioxolane, 2-ethyl-4-methyl; acetone; 2-ethyl-trans-2-butenal; and propylene glycol. Based on an economic evaluation of the process, it was decided that the maximization of the selectivity of propionaldehyde would be the overall goal of the project.

Numerous zeolite catalysts containing varying crystalline structures, silica to alumina ratios, and porosities were tested within this reactor system. ZSM-5 with a silica to alumina ratio of 50:1 was found to be the best microporous catalyst for this reaction.

However, upon varying porosities within the catalyst, mesoporous structured zeolite-Y catalyst with a 30:1 silica to alumina ratio was shown to outperform all microporous catalysts. 2-D MFI zeolites and Pt-H-ZSM-5 catalysts were also synthesized and tested. Although Pt-H-ZSM-5 showed very low conversion, likely due to catalyst deactivation, the synthesized 2-D MFI zeolites showed very high levels of selectivity toward propionaldehyde, ~70%. After preliminary catalyst testing, the reaction conditions within the system were optimized. The steam percentage in the carrier gas, the reaction temperature, and the catalyst to polyol ratio for the catalytic cracking of polypropylene glycol were tested in a Box-Behnken type design of experiment (DOE). Based on the DOE results, the reaction temperature was the most important parameter for this reaction, which allowed correlations between temperature and the seven products of interest to be drawn. Characterization of fresh and spent catalysts were also investigated through numerous characterization techniques including TGA, XRD, SEM, PALS, and nitrogen physisorption. Through these characterization techniques, the existence of coke on/in the spent zeolite samples was evident.

TABLE OF CONTENTS

Abstract	iii
List of Tables	vi
List of Figures	viii
List of Symbols	xiii
List of Abbreviations	xiv
CHAPTER 1: ISSUES AND POTENTIAL SOLUTIONS FOR PLASTIC WASTE	
RECYCLING.....	1
1.1 Issues Facing Modern Recycling Processes	2
1.2 Catalytic Cracking via Zeolite Catalysts	6
1.3 Polyols and Polyurethane	17
1.4 2-D Mordenite Framework Inverted (MFI) Zeolite Nanosheets	20
CHAPTER 2: EXPERIMENTAL METHODOLOGY	
2.1 Reactor System Setup.....	26
2.2 Reaction Materials.....	37
2.3 Product Gas Analysis	37
2.4 Catalyst Characterization Methods	53
2.5 Catalyst Synthesis Methodology	59
2.6 Reaction Conversion and Selectivity Methodology via Liquid Chromatography-Mass Spectrometer	64
2.7 General Economic Evaluation	67

CHAPTER 3: EXPERIMENTAL RESULTS AND DISCUSSION	71
3.1 Design of Experiment (DOE) Using Reactor Setup Version 1.0	71
3.2 Design of Experiment (DOE) Using Reactor Setup Version 3.0	79
3.3 Temperature Impact on Product Selectivity	86
3.4 Initial Zeolite Testing	87
3.5 ZSM-5 Silica to Alumina Ratio Testing	90
3.6 Meso-porous Zeolite-Y Testing	92
3.7 Thermal Cracking of PPG	95
3.8 H-ZSM-5 vs. NH ₄ -ZSM-5	97
3.9 Pt-H-ZSM-5 vs. H-ZSM-5	99
3.10 2-D MFI Zeolite Testing	100
3.11 Additional Polyols Tested	102
3.12 Spent Catalyst Characterization	103
CHAPTER 4: CONCLUSIONS AND FUTURE DIRECTIONS	122
References	128

LIST OF TABLES

Table 2.1: Physical Mass Balance Closure of Version 2.0	44
Table 2.2: The area percentages of the GC-MS chromatogram of the vapor, aqueous, and organic phases of the condenser in version 2.0.....	46
Table 2.3: The adjusted selectivity of the primary seven products in the standard reaction run.....	52
Table 2.4: Nitrogen physisorption data for microporous and mesoporous zeolite Y sample	60
Table 2.5: The 2019 global market value and 2016 chemical price of the seven primary products.....	68
Table 3.1: The experimental parameters used for the DOE runs and their resulting propionaldehyde selectivity.....	74
Table 3.2: Individual run parameters and propionaldehyde selectivity for the DOE of reactor version 3.0	81
Table 3.3: The selectivity of the primary seven products for different zeolites and gamma-phase Al oxide	88
Table 3.4: The selectivity of the primary seven products for NH ₄ -ZSM-5 of varying silica to alumina ratios	91
Table 3.5: The selectivity of the primary seven products for the various zeolite-Y samples	93
Table 3.6: The selectivity of the primary seven products via NH ₄ -ZSM-5 catalyst and thermal cracking.....	96
Table 3.7: The selectivity of the primary seven products via H-ZSM-5 and NH ₄ -ZSM-5 catalysts	98
Table 3.8: The selectivity of the primary seven products via H-ZSM-5 and Pt-H-ZSM-5 catalysts.....	100

Table 3.9: The selectivity of the primary seven products via the non-mixed and mixed MFI zeolites as well as H-ZSM-5	101
Table 3.10: PAL results for the four ZSM-5 samples with source correction	115
Table 3.11: Average PAL results for the four ZSM-5 samples with source correction	116
Table 3.12: The relative change in PAL values compared to the fresh ZSM-5 sample.....	117
Table 3.13: The chemical formula and structure for PPG and the primary seven products	119

LIST OF FIGURES

Figure 1.1: The global production and outcome of plastic products	2
Figure 1.2: SEM image of a PP:PET (85 : 15 wt%) mixture.....	4
Figure 1.3: Structural representation of various zeolites	7
Figure 1.4: Solid-state IR spectrum of HY zeolite (solid line) and H-Y zeolite having adsorbed pyridine (dotted line)	8
Figure 1.5: Catalytic cracking mechanism of long-chained hydrocarbons.....	9
Figure 1.6: IR spectra of H-ZSM-5 samples with varying Si/Al ratios	11
Figure 1.7: XRD patterns of natural zeolite (A) and zeolite supported metals: Ni-zeolite (B), Ni-Mo-zeolite (C), Co-zeolite (D), and Co-Mo-zeolite (E)	13
Figure 1.8: XRD patterns for ZSM-5 and ZSM-5 doped with Gd, Pt, and Pt/Gd	14
Figure 1.9: Average product gas (PG) versus the number of cracking and regeneration cycles for ZSM-5 and ZSM-5 doped with Gd, Pt, and Pt/Gd.....	15
Figure 1.10: The schematic for the dealumination of a zeolite.....	16
Figure 1.11: IR spectra of decomposing polyurethane at 300 °C (A) and 397 °C (B) in N ₂ atmosphere at 30 °C/min.....	18
Figure 1.12: The products of the catalytic cracking of polypropylene glycol in an FCC unit.....	20
Figure 1.13: Pyrolysis of propylene glycol reaction schematic	21
Figure 1.14: Characterization of 2-D MFI zeolite nanosheets A) small-angle PXRD patterns B) wide-angled PXRD patterns C) N ₂ adsorption isotherms (C) pore size distributions of MFI zeolite nanosheets	22
Figure 1.15: MFI nanosheet crystalline structure changes throughout the four 12-hour cycles	23
Figure 1.16: FTIR spectra of ZSM-5 and MFI nanosheets at various synthesis times.....	23

Figure 1.17: Selectivity of Alkyltoluene versus the concentration of Brønsted acid sites on the MFI nanosheets throughout the four 12-hour cycles; note that ZNS-MW-6T and ZNS-MW-6 zeolite nanosheets were nanosheets synthesized through microwave irradiation	24
Figure 1.18: SEM images of 2-D MFI zeolites.....	25
Figure 2.1: Side view of the reactor.....	27
Figure 2.2: Reactor Setup version 1.0.....	31
Figure 2.3: Reactor setup version 2.0	35
Figure 2.4: Reactor setup version 3.0	37
Figure 2.5: Analytical setup for version 1.0 of the reactor setup.....	38
Figure 2.6: TCD and FID chromatogram of preliminary data from the GC analytical setup used in version 1.0 of the reactor	39
Figure 2.7: The GC-MS chromatogram for the product gas of version 1.0 of the reactor system	40
Figure 2.8: GC-MS chromatogram for the condensate of version 1.0 of the reactor system	41
Figure 2.9: GC calibration curves for propionaldehyde and nitrogen used in version 1.0 of the reactor setup	42
Figure 2.10: Propionaldehyde (propanal) calibration curve (left) and adjusted propanal calibration curve (right)	46
Figure 2.11: GC-MS chromatogram of a standard catalytic cracking run.....	49
Figure 2.12: Calibration curves for the primary seven products	51
Figure 2.13: Calibration curve for the external standard	53
Figure 2.14: TGA of PPG	54
Figure 2.15: TechnoAP Digital Instrumentation for PALS along with the fast scintillator detectors and the sample source.....	56

Figure 2.16: PAL measurements of ZSM-5 reacted with polyurethane pellets (left) and ZSM -5 with polypropylene glycol pellets (right)	58
Figure 2.17: Nitrogen physisorption data for microporous and mesoporous zeolite Y samples.....	60
Figure 2.18: PXRD pattern of the synthesized MFI zeolite nanosheets	63
Figure 2.19: SEM images of synthesized 2-D MFI zeolites	64
Figure 2.20: LCMS data for PPG a) the m/z from the mass spectrometer b) the LC-MS chromatogram.....	65
Figure 2.21: LC-MS calibration curve for PPG Mn ~425	66
Figure 2.22: The yearly, global market value forecast for propionaldehyde.....	70
Figure 3.1: The preliminary testing of reaction temperature, the catalyst to polyol ratio, and the steam percentage in the carrier gas on the selectivity of propionaldehyde.....	72
Figure 3.2: Visual representation of the DOE experimental points	74
Figure 3.3: Pareto Chart for DOE results.....	75
Figure 3.4: The main effects plot for the DOE	76
Figure 3.5: The Contour Plots for the DOE.....	77
Figure 3.6: The Surface Plot for the catalyst to polyol ratio vs. temperature vs. propionaldehyde selectivity	78
Figure 3.7: Preliminary results for the reactor setup version 3.0 DOE.....	80
Figure 3.8: The design space for the DOE conducted on version 3.0 of the reactor system	82
Figure 3.9: The Pareto chart for the DOE conducted on version 3.0 of the reactor system	82
Figure 3.10: The main effects plot for the DOE in version 3.0 of the reactor setup	83
Figure 3.11: The contour plots for the DOE in version 3.0 of the reactor setup	84
Figure 3.12: The Surface Plot for the catalyst to polyol ratio vs. temperature vs. propionaldehyde selectivity.....	85

Figure 3.13: The effect of temperature on the selectivity of the primary seven products	86
Figure 3.14: Propionaldehyde selectivity for different zeolites and gamma-phase Al oxide	88
Figure 3.15: Pictures of the different catalysts tested and their respective condenser fluid.....	89
Figure 3.16: Propionaldehyde selectivity for varying silica to alumina ratios of NH ₄ -ZSM-5 catalysts.....	91
Figure 3.17: Pictures of the ZSM-5 catalysts tested with varying silica to alumina ratios and their respective condenser fluid	92
Figure 3.18: Propionaldehyde selectivity for various zeolite-Y samples	94
Figure 3.19: Pictures of the zeolite-Y catalysts tested with varying porosity and silica to alumina ratios and their respective condenser fluid.....	95
Figure 3.20: The LC-MS chromatogram for the catalytic and thermal cracking samples.....	97
Figure 3.21: GC-MS chromatogram of the catalytic cracking of polyurethane reaction.....	102
Figure 3.22: PXRD pattern for the 5x reacted ZSM-5 sample and a fresh ZSM-5 sample	104
Figure 3.23: Baseline adjusted IR spectrum of 5x reacted ZSM-5	106
Figure 3.24: TGA for the 5x reacted ZSM-5 catalyst in argon and air	107
Figure 3.25: TGA mass loss of spent NH ₄ -ZSM-5 samples with varying steam percentages	107
Figure 3.26: TGA curves for various spent catalysts.....	109
Figure 3.27: Normalized TGA mass loss of various spent catalysts	109
Figure 3.28: TGA curves for spent NH ₄ -ZSM-5 catalysts with varying silica to alumina ratios	110
Figure 3.29: Normalized TGA mass loss for spent NH ₄ -ZSM-5 catalysts with varying silica to alumina ratios	111

Figure 3.30: TGA curves for the spent meso-porous and microporous zeolite-Y catalysts	112
Figure 3.31: Normalized TGA mass loss for spent meso-porous and microporous zeolite-Y catalysts.....	112
Figure 3.32: Spent Pt-H-ZSM-5 catalyst	114
Figure 3.33: PAL results for the four ZSM-5 catalysts normalized to ZSM-5 for I_2 , τ_3 (T_3), and I_3	118
Figure 3.34: Proposed reaction mechanism of the catalytic and thermal cracking of polypropylene glycol	121

LIST OF SYMBOLS

σ	Standard deviation
τ	The trapping and o-Ps pickoff lifetime values

LIST OF ABBREVIATIONS

ABS	Acrylonitrile/Butadiene/Styrene
AMOC.....	Age Momentum Coincidence Spectroscopy
BET	Brunauer–Emmett–Teller
CDB	Coincidence Doppler Broadening
DOE	Design of Experiments
DRIFTS	Diffuse Reflectance for Infrared Fourier Transform Spectroscopy
EDS	Energy Dispersive Spectroscopy
EDS	Energy Dispersive Spectroscopy
FCC	Fluidized Catalytic Cracking
FID	Flame Ionization Detector
GC	Gas Chromatograph
GC-MS	Gas Chromatography-Mass Spectrometer
HDPE	High-Density Polyethylene
HPLC	High-Performance Liquid Chromatography
ICP-MS	Inductively Coupled Plasma Mass Spectrometry
ID	Inner Diameter
INL.....	Idaho National Lab
IUPAC.....	International Union of Pure and Applied Chemistry
LC-MS	Liquid Chromatography-Mass Spectrometer

LDPE.....	Low-Density Polyethylene
MAS NMR.....	Magic Angle Spinning Nuclear Magnetic Resonance
MCT.....	Mercury Cadmium Telluride
MFI.....	Mordenite Framework Inverted
MFC.....	Mass Flow Controller
NDA.....	Non-Destructive Analysis
NST.....	Nuclear Science and Technologies
OD.....	Outer Diameter
PAL.....	Positron Annihilation Lifetime
PALS.....	Positron Annihilation Lifetime Spectroscopy
PAS.....	Positron Annihilation Spectroscopy
PET.....	Polyethylene Terephthalate
PG.....	Product Gas
PP.....	Polypropylene
PS.....	Polystyrene
PTFE.....	Polytetrafluoroethylene
PVC.....	Polyvinyl Chloride
PXRD.....	Powder X-Ray Diffraction
SE2.....	Type II Secondary Electrons
SEM.....	Scanning Electron Microscopy
TCD.....	Thermal Conductivity Detector
TGA.....	Thermogravimetric Analysis
UofSC.....	University of South Carolina

XRD	X-Ray Diffraction
ZSM-5	Zeolite Socony Mobil-5

CHAPTER 1

ISSUES AND POTENTIAL SOLUTIONS FOR PLASTIC WASTE

RECYCLING

Recycling has been an overarching issue facing the planet for many decades. The management of waste plastic is essential for building sustainable and livable societies¹. However, a lack of proper recycling implementation, uncontrolled disposal, and a general lack of public awareness has led to severe environmental consequences. In fact, approximately 78% (4.9 billion tonnes) of all the plastic ever made has been disposed of in landfills or continues to persist elsewhere in the environment^{1,2}. Large-scale plastic production has been around since ~1950, yet end-of-life plastic treatment methods are still quite limited^{2,3}. In the year 2015, for example, a mere 8.8% of the commercially produced plastic was recycled in the United States³. Through current means of recycling, this trend is projected to increase into the near future². In fact, the difference between the amount of waste recycled and the amount of waste produced globally is expected to increase drastically over the next few decades². Given the large degradation time of these plastics, the potential threat of microplastic, tiny plastic pieces formed because of plastic degradation, to human and environmental health remains. Thus, it is important that innovative, recycling technologies are developed and implemented to close the gap between the amount of plastic produced vs. the amount of plastic waste recycled. The 1950-2015 data displayed in Figure 1.1 is based on historical data while the 2015-2050 data have

been extrapolated based on said historical data on a global scale. Based on Figure 1.1, innovative technology needs to be implemented to close the gap between waste generated and waste recycled².

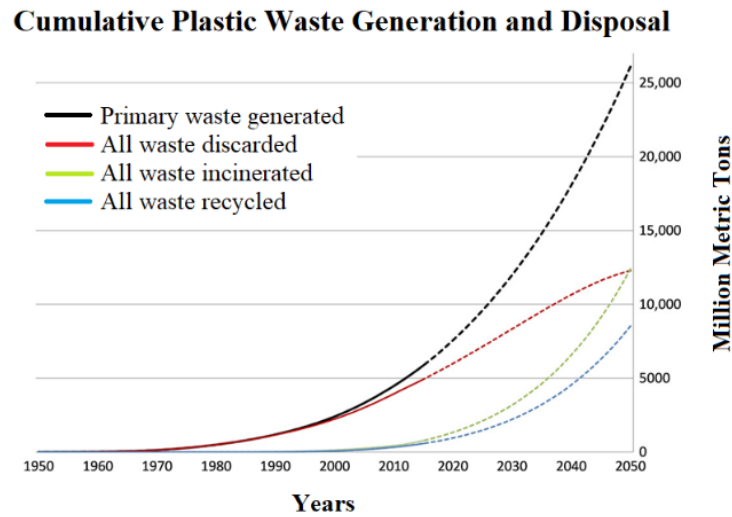


Figure 1.1: The global production and outcome of plastic products²

1.1 Issues Facing Modern Recycling Processes

Plastics fall under one of two categories, thermoplastic polymers: polyethylene terephthalate (PET), high-density polyethylene (HDPE), polyvinyl chloride (PVC), low-density polyethylene (LDPE), polypropylene (PP), polystyrene (PS), acrylonitrile/butadiene/styrene (ABS), etc. and thermosetting polymers: phenolic, polyurethane, unsaturated polyester, etc^{3,4}. Despite the large variety of plastics, polyethylene terephthalate (PET) and polyethylene are the only plastics that are commercially recycled at a rate greater than 1% of their production. PET and polyethylene make about 9% and 37%, respectively, of the total plastic produced in the United States annually². Therefore, there are little to no recycling methods for over half of the plastic produced in the United States. One such example of these overlooked plastics are polyols

and polyurethanes. Polyols and polyurethane can be found in abundance within modern society; they have uses in insulation, coatings, adhesives, foams for mattresses, footwear, and car seats⁵. Despite their abundance of useful applications, implementations of polyol and polyurethane recycling are quite rare^{6,7}

Modern day recycling methods primarily consist only of mechanical recycling approaches, regarding industrial methodologies. These approaches first consist of sorting the plastic into their respective categories, which is then followed by washing them to remove organic residue, melting, shredding, and finally recasting of said plastics. Additionally, virgin plastic is added to these recycled plastics, prior to recasting, in order to ensure chemical and mechanical properties are satisfied for manufacturing^{3,8}. Despite their simplicity, mechanical recycling approaches have many limitations. Not only are there economic and time constraints associated with mechanical processes, but temperature-sensitive plastics cannot be recycled through the means described previously, as they will lose their chemical properties and decompose beyond suitability^{3,8}. Additionally, general degradation throughout the lifetime of a plastic as well as the inability to process complex mixtures pose large issues for mechanical processes^{8,9}. This phenomenon of incompatibility can be seen in the scanning electron microscopy (SEM) image below in Figure 1.2. Figure 1.2 shows that PET particles, the smaller lighter/darker circles, are almost adhering to the surface of the PP instead of uniformly mixing, which results in the inability to process said mixture⁹.

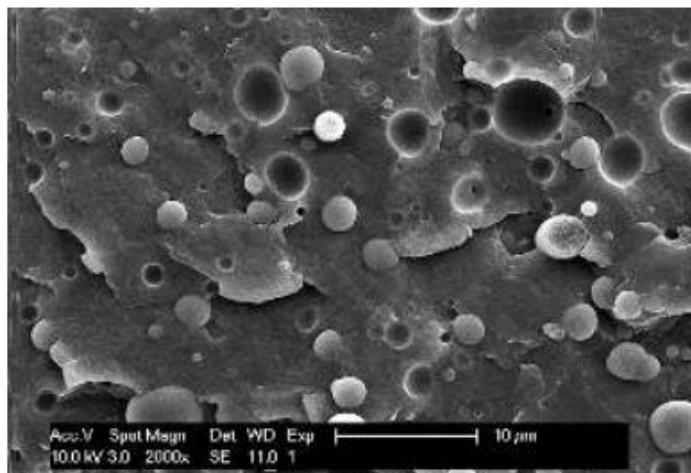


Figure 1.2: SEM image of a PP:PET (85 : 15 wt%) mixture⁹

In order to overcome the limitations of mechanical recycling approaches, innovative approaches for various process steps are being developed and are currently in use. Most of these approaches relate to the sorting process of mixed, solid plastics. Such approaches involve electrostatic separation, which rely on a specific plastic compound's charge deflection in an electric field; flotation and froth flotation separation, which rely on a specific plastic's density; magnetic density separation, which involves the magnetic separation of plastic compounds suspended in a magnetic liquid while under an induced magnetic field; and x-ray detection, which allows for the detection of chlorine rich compounds, such as PVC^{8,10}. Despite these modern-day advances, mechanical processes are still quite limited in their ability to recycle plastics effectively; thus, research has turned its attention to chemical and biological processes as a means for plastic recycling going forward^{8,10–13}.

Innovative chemical processes involved in the recycling of plastics primarily fall into three categories: chemolysis, pyrolysis, and catalytic cracking. Chemolysis is a process that involves the depolymerization, deconstruction of polymers into monomers, of plastic

compounds via chemical reactions, such as glycolysis and hydrolysis. Unlike pyrolysis and catalytic cracking, chemolysis involves the introduction of a new reactant material in addition to the plastic waste. This new reactant material reacts with the plastic compounds to depolymerize the long, complex chains that make up plastics. On the other hand, pyrolysis is not defined by a chemical additive to a plastic mixture, but as the act of breaking down polymer chains to form smaller molecules in a high temperature environment, typically in the absence of oxygen. This decomposition results in depolymerization or random fragmentation of the starting plastic material. Catalytic cracking is defined as the use of a catalyst to breakdown long-chain, organic compounds^{8,11}. Unlike mechanical processes, chemical and biological processes are not focused on the regeneration of plastic molecules, but on their conversion into economically viable petrochemicals. Catalytic cracking and pyrolysis reactions have great potential in the plastic recycling industry due to their relative ease of implementation; however, such processes result in a wide range of product chemicals, which is disastrous from a reaction kinetics and separation standpoint. Additionally, biological advances in enzymatic reaction may potentially prove to be useful as a means of plastic conversion and chain length selective cleaving^{12,13}.

Despite their complexity, a catalytic cracking reaction has the potential to revolutionize the plastic recycling industry due to its cost-effective approach of plastic reformation. The catalysts predominately used in catalytic cracking reaction are silica-alumina based catalysts, zeolites, and mesoporous materials, especially that of Zeolite Socony Mobil-5 or more commonly known as ZSM-5^{9,11,14,15}. Thus, in order to fully optimize a catalytic process, it is important to fully understand the reaction kinetics and the structures

of said catalyst. As this may potentially give insight into plastic reactions that are relatively unstudied.

1.2 Catalytic Cracking via Zeolite Catalysts

Catalytic cracking of hydrocarbons via zeolite catalysis has been around since the 1960s and 1970s^{16,17}. Zeolite catalyst applications primarily occur in fluidized catalytic cracking (FCC) units at elevated temperatures^{9,11,14,15,17–21}. Zeolite employment through FCC units can be found in oil and gas refining applications, biomass conversion, methane conversion, and more recently plastic recycling^{9,11,14,15,17–26}. As such, there is a considerable amount of research in the field of pyrolysis and catalytic cracking of waste plastic via zeolite catalysts^{6,7,9,11,14,15,21–23,27,28}. Much of this research is geared toward thermoplastics with an emphasis on the production of gasoline range hydrocarbons and other valuable petrochemical products^{9,11,14,15,21–23}. Nonetheless, zeolites are playing a major role in research geared toward plastic waste recycling and upcycling^{9,11,14,15,20–23,29,30}.

1.2.1 Zeolite Overview

Zeolites are characterized through their SiO_4 and AlO_4 tetrahedra based structure. The corners of these tetrahedra are linked via an oxygen atom, which result in an organic macromolecule. These joined tetrahedra are made up of SiO_2 and AlO_2^- molecules, which results in the aluminum-based tetrahedra structures to hold a negative charge at their center. The overall zeolite framework is comprised of channels and cages with dimensions from 0.1 to 1 nm, as shown in Figure 1.3³¹. Within these channels, there lies water molecules and cations to balance out the negative charge of the aluminum. Thus, the overall formula for a zeolite can be written as $\text{A}^{m+}_{y/m}[(\text{SiO}_2)_x(\text{AlO}_2)_y \cdot z\text{H}_2\text{O}]$, where m represents the cation charge, A represents the cation, x+y represents the number of tetrahedra per

crystallographic unit cell, and x/y represents the silicon/aluminum ratio³¹. According to the International Union of Pure and Applied Chemistry (IUPAC) classification system, microporous structures are classified as having a $dp \geq 2.0$ nm, mesoporous structures are classified as having a $2.0 \text{ nm} < dp \leq 50$ nm, and macroporous structures are classified as having a $dp > 50$, where dp represents pore diameter^{31,32}. According to this classification, most zeolites would fall under the microporous structure category. Additionally, it is important to note that zeolites contain uniform pores and are classified as crystalline aluminosilicates³¹.

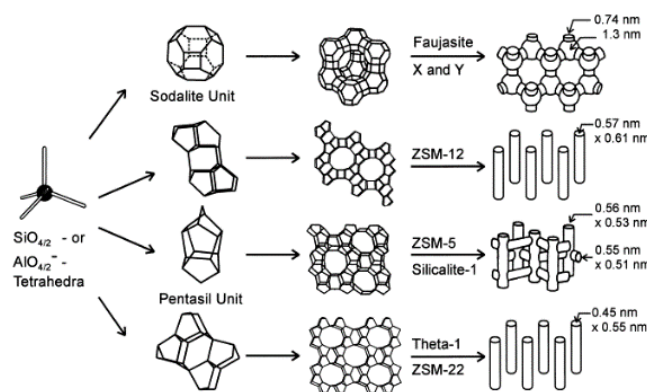


Figure 1.3: Structural representation of various zeolites³¹

1.2.2 Zeolite Surface Chemistry

The most important characteristic for a zeolite are its acidic sites, which give a zeolite its catalytic reactivity. These sites consist of both Brønsted and Lewis acid sites. It is these acidic sites that enable zeolites to breakdown long-chain hydrocarbons^{31,32}. However, it is important to note that severe heat treatment of the zeolite (≥ 500 °C) causes the Brønsted acid sites to degrade; this is due to the splitting off of water within the site, known as dihydroxylation, turning the site into a Lewis acid. Figure 1.4 presents a solid-state infrared (IR) spectroscopy of H-Y zeolite (solid line) and H-Y zeolite having adsorbed pyridine (dotted line). The two bands occurring at 3640 cm^{-1} and 3550 cm^{-1} represent the

bridging that occurs between the O-H group in the sodalite cages. However, when pyridine is absorbed onto the zeolite's surface, the band present at 3640 cm^{-1} disappears. This exemplifies the molecular sieve effect of zeolites; the cage, represented by the 3550 cm^{-1} band, is too small for the pyridine to penetrate unlike the cage present at the 3640 cm^{-1} band. Examining the right side of the spectrum, two bands are present at 1542 cm^{-1} and 1455 cm^{-1} , which represent the Brønsted and Lewis acid sites, respectively³¹. The identification of acid sites is of great interest in zeolite chemistry because it has been found that their catalytic nature stems from the Brønsted acid sites rather than the Lewis acid sites. However, in certain instances, it has been reported that Lewis acid sites may enhance the Brønsted acid sites, which in turn, would increase a zeolite's catalytic activity^{31,33}.

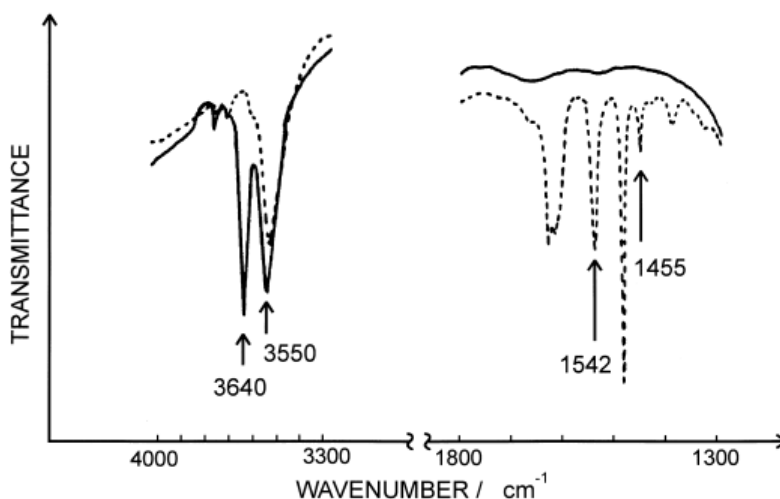


Figure 1.4: Solid-state IR spectrum of H-Y zeolite (solid line) and H-Y zeolite having adsorbed pyridine (dotted line)³¹

1.2.3 Catalytic Cracking Mechanism

The exact mechanism for acid site catalytic cracking, shown in Figure 1.5, has been up for debate since the early days of its discovery^{20,34}. However, the theorized mechanism involves the formation of carbenium ions on Brønsted acid sites via proton donation to an

alkene, which can be the result of previous thermal cracking. Lewis acid sites can also play a role in the formation of carbenium ion formation through hydride abstraction from an alkene. Then, a Brønsted site can donate a proton to an alkene, forming a carbonium ion, which can then split off dihydrogen to form a carbenium ion or undergo protolytic cracking to form an alkane and a carbenium ion. The resulting carbenium ions formed in these processes crack through β -scission, forming alkenes and smaller carbenium ions. Lastly, the recovery of hydrides from a Lewis acid site will result in the formation of alkanes from carbenium ions, and the donation of a proton from the carbenium ions to a Brønsted acid site will result in the formation of an alkene, terminating the reaction^{20,34–39}. Additionally, steam is often used in catalytic cracking to inhibit secondary reactions that result in coking^{40–42}.

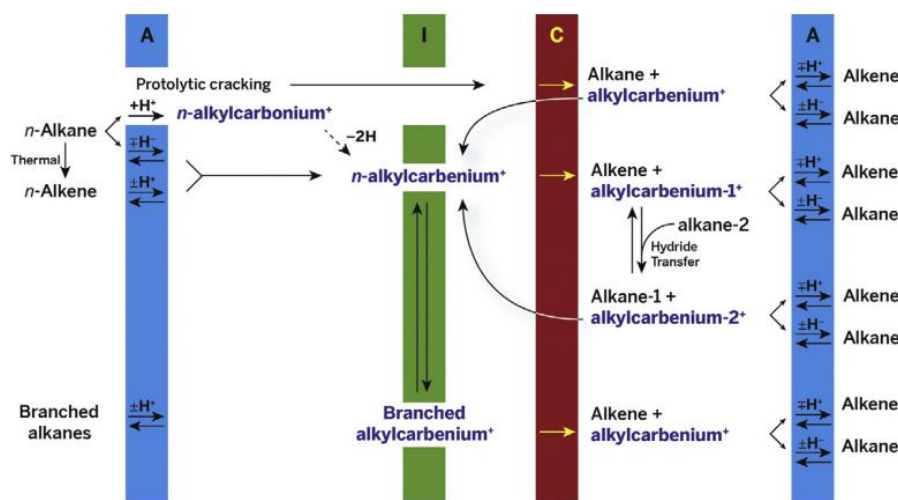


Figure 1.5: Catalytic cracking mechanism of long-chained hydrocarbons¹⁷

1.2.4 Zeolite Crystalline Shape and Pore Size

The pore size of a zeolite can play a large role in the product yield and overall conversion of a reaction. As previously mentioned, the molecular sieve effect can cause a zeolite to react selectively with smaller or larger molecules. By manipulating the pore size

of a zeolite catalyst, it is possible to alter the resultant chain length of a product hydrocarbon^{27,29–31}. However, larger pore size does not always lead to increased selectivity, as found by Y. Li et al. It was discovered, through experimentation with polymer chain lengths and membrane zeolites, that long chain polymers may cause the blockage of a zeolite pore, which would reduce the overall selectivity of the reaction. This phenomenon, which was coined the effect of polymer chain rigidification, seems to occur due to rapid cooling of the zeolite membranes³⁰.

It has also been shown that the shape of the zeolite crystals can play a role in the selectivity of a reaction. Y. S. Bhat et al. found there be a clear correlation between zeolite crystal size and reaction selectivity^{43,44}. Crystallite structures from length 5.7 to 37.9 μm , which resulted in a selectivity from 32% to 81%, respectively, for an isomerization of xylene reaction⁴³. This concept has also been demonstrated by Olson and Haag, who showed a significant selectivity increase by increasing the crystal size of a zeolite by nearly two orders of magnitude⁴⁴. Therefore, it can be concluded that small or large differences in crystalline sizes can vastly improve reaction selectivity; this improvement is due to an increase in selectivity of the primary product while secondary isomerization is reduced^{43,44}.

1.2.5 Zeolite Silicon/Aluminum Ratio

As previously mentioned, zeolites are comprised of SiO_2 and AlO_2^- molecules; thus, the greater the number the AlO_2^- , the greater the acidity of the zeolite itself, as per the charge of AlO_2^- would indicate. The idea of comparing the number of SiO_2 and AlO_2^- is known as the silicon to aluminum ratio ($\text{SiO}_2/\text{Al}_2\text{O}_3$ or Si/Al ratio)^{31,45,46}. The idea of increasing the amount of Al content in a zeolite to increase its acidity can be observed in Figure 1.6⁴⁵. Figure 1.6 displays IR spectra for five samples of H-ZSM-5 with increasing

Si/Al ratios; in other words, sample 1 has the highest number of Al atoms while sample 5 has the fewest number of Al atoms structurally present. The bands present at 3720 cm^{-1} and 3600 cm^{-1} represent Brønsted acid sites. Figure 1.6 shows that as the amount of Al structurally present in the H-ZSM-5 sample increases, the number of Brønsted acid sites also increases⁴⁵. Therefore, as the number of Al atoms structurally present increase, as does overall zeolite acidity. Moreover, it has then been shown that as the zeolite acidity increase, so too does the catalytic activity of the zeolite^{29,45,46}.

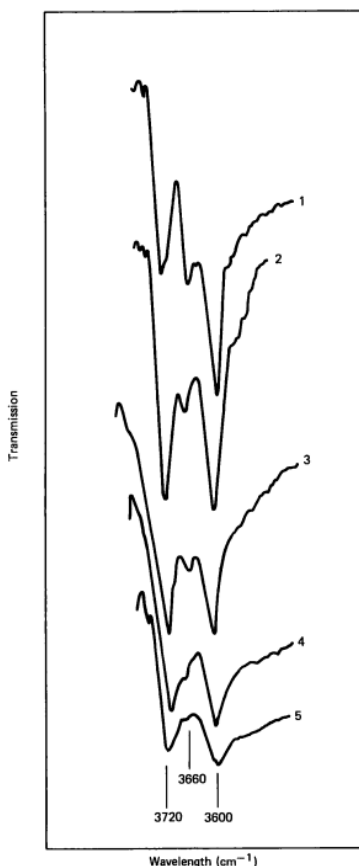


Figure 1.6: IR spectra of H-ZSM-5 samples with varying Si/Al ratios⁴⁵

The idea of “super acid sites” has also been proposed due to a significant increase in the number of Al atoms structurally present in a zeolite^{45,46}. However, an increase in catalytic activity does not always lead to an increase in desired products, as observed by

M. A. Uguina et al. It was observed that by decreasing the Si/Al ratio, the selectivity of the primary product decreased, due to an increase in the selectivity of secondary products⁴⁶.

1.2.6 Implementations of Metals into the Zeolite Framework

The process in which framework aluminum are removed from the “core” zeolite structure is known as dealumination^{31,47}. These are typically replaced by silicon to decrease the number of acid sites on the zeolite surface³¹. However, W. Sriningsih et al. demonstrated that natural zeolites can be used as a support for other metals through the implementation of dealumination. Figure 1.7 displays the X-ray diffraction (XRD) patterns for these associated zeolites, which contain Ni, Ni-Mo, Co, and Co-Mo metals⁴⁷. Based on Figure 1.7, moderate alterations were made to crystallographic structure of the natural zeolite upon the dealumination and introduction of a new metal. The resulting selectivity of these zeolite supported metal catalysts were higher than that of the natural zeolite when used to hydrocrack LDPE plastic waste. It was shown that the zeolite supported metal catalysts have a much higher amount of acid compared to that of the natural zeolite. Therefore, it was concluded that the selectivity of the zeolite supported metal catalysts, compared to that of the natural zeolite, was due to increase in acidity and the strengthening of acidic sites through the replacement of Al with other metals⁴⁷.

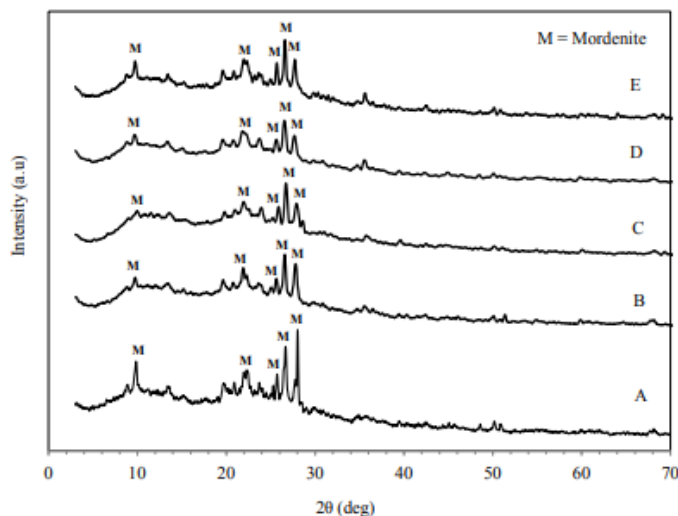


Figure 1.7: XRD patterns of natural zeolite (A) and zeolite supported metals: Ni-zeolite (B), Ni-Mo-zeolite (C), Co-zeolite (D), and Co-Mo-zeolite (E)

1.2.7 Different Types of Zeolites used for Catalytic Cracking

As previously discussed, zeolite pore size can play a large role in the product yield and conversion of a reaction due to the molecular sieve effect^{20,27,29–31}. Thus, synthesis of zeolites with varying pore sizes to test the catalytic cracking of various plastics may yield interesting results, as has been the case for other types of catalytic cracking reactions^{27,29,30,48,49}. Such zeolites may include meso-porous variants of ZSM-5, Zeolite Y, and MCM-41, as these have been tested on several polymers in the literature^{27,29,30,48,49}.

1.2.8 Coke Formation on Zeolite Catalysts

Coking, the buildup of solid carbon particles on the surface of a catalyst, has greatly hindered zeolite catalysts used in catalytic cracking reactions^{50–52}. Coking is an unavoidable phenomenon when used for hydrocarbon cracking due to the presence of longer-chain and aromatic hydrocarbons⁵¹. There is quite a noticeable difference in the surface morphology of the fresh catalyst versus the used catalyst. This difference in appearance can be attributed to coke buildup on the surface of the zeolite. This buildup

blocks the acidic sites on the zeolite catalyst, which causes a decrease in the catalytic reactivity of the zeolite itself^{50,51}. However, a zeolite with coke buildup can be regenerated through high temperatures and in the presence of oxygen to allow the conversion of solid carbon to CO₂. Despite regenerative efforts, some coke may never leave the surface; additionally, the high temperatures required for regeneration may lead to degradation of the zeolite, as shown in Figure 1.8⁵¹. Examining the difference between the dashed and dotted lines of the various catalysts, it is clear to see the change in the crystallinity of ZSM-5 after undergoing five cracking and regeneration cycles. The reason for the large discrepancy between the XRD patterns in the ZSM-5 is a change in crystalline structure from orthorhombic to tetragonal⁵¹.

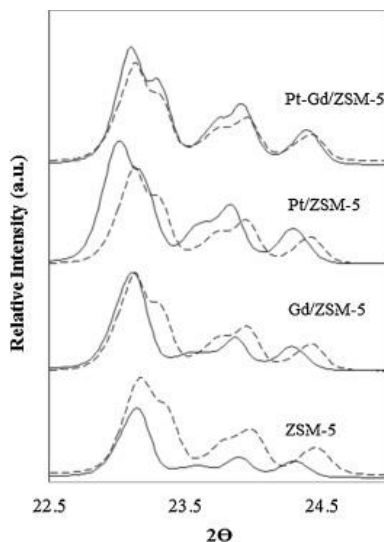


Figure 1.8: XRD patterns for ZSM-5 and ZSM-5 doped with Gd, Pt, and Pt/Gd.

Although five cracking and regeneration cycles resulted in a crystalline structure change for ZSM-5, metal doping of ZSM-5 was shown to significantly reduce said crystalline structure change, as observed by S. Kim et al. Figure 1.8 displays the XRD pattern for three additional ZSM-5 zeolites that were doped with Gd and/or Pt. Based on the Figure, the doped catalyst resulted in significantly less crystalline structure alterations

than regular ZSM-5, especially that of ZSM-5 doped with Pt and Gd. Additionally, it was found that these lack of alterations allowed the selectivity of the cracking reaction to be more consistent through multiple cracking and regeneration cycles, as seen in Figure 1.9 below. Figure 1.9 shows a steep decline in the selectivity of the reaction for ZSM-5 while almost no loss, if any, in the selectivity of the reaction for Pt and Gd doped ZSM-5⁵¹.

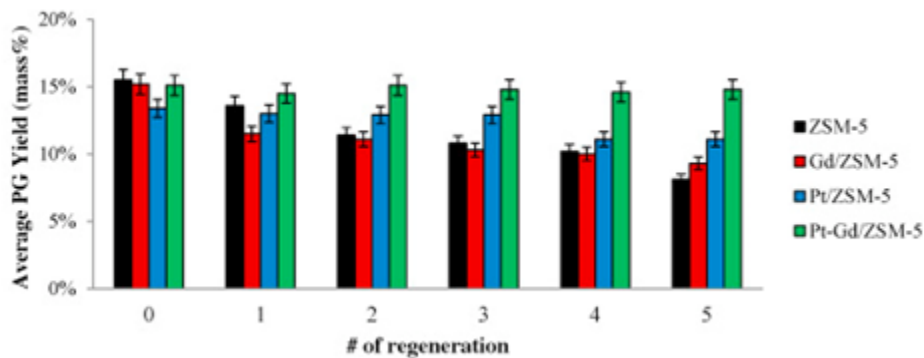


Figure 1.9: Average product gas (PG) versus the number of cracking and regeneration cycles for ZSM-5 and ZSM-5 doped with Gd, Pt, and Pt/Gd⁵¹

1.2.9 Dealumination of Zeolites

Dealumination of zeolites, induced through the usage of steam, in catalytic cracking reactions have long since been an issue in gas-oil fluid catalytic cracking units⁵³. This phenomenon, shown in Figure 1.10, leads to Al extraction from the framework but not the material, resulting only in the alteration of the (Si/Al) framework ratio⁵³.

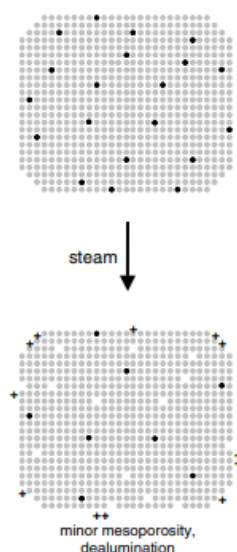


Figure 1.10: The schematic for the dealumination of a zeolite⁵³

Dealumination typically occurs in high temperature environments (above 500 °C) over prolonged steam exposure^{53–55}. Dealumination can result in the reduction of Brønsted acid sites and the creation of Lewis acid sites, as Brønsted acid sites are derived from Al in the framework and Lewis acid sites are derived from Al in extra-framework⁵³. Alterations to Brønsted and Lewis acid sites can significantly impact the catalytic activity of the zeolite^{53–55}. Thus, it is important to identify dealumination of the spent catalyst, which can be done using magic angle spinning nuclear magnetic resonance (MAS NMR)⁵⁶. MAS NMR would allow the identification of changes in Al-O bonds and thus, indicate changes to the aluminum framework^{56–58}. In fact, literature has shown that shifts in 53 and 60 ppm in ²⁷Al MAS NMR demonstrate changes in framework species tetrahedral Al sites associated with zeolites^{57,58}. Additionally, changes in Brønsted and Lewis acid sites can be investigated with in-situ-FTIR, via pyridine adsorption, by examining changes in hydroxyl group bands (3400-3800 cm⁻¹) and pyridine-acid sites interaction bands (1400-1600 cm⁻¹)^{45,51,58–60}.

1.3 Polyols and Polyurethane

As previously mentioned, there are many different types of plastic, but modern day recycling methods and research are primarily focused on PET and polyethene^{3,4,10}. In other words, a large majority of the plastics produced end up in a landfill³. One such example of these overlooked plastics are polyols and polyurethanes. Polyols and polyurethanes can be found in abundance in modern times; they have uses in insulation to coatings to adhesives to foams for mattresses to footwear to car seats. Despite their abundance of useful applications, implementations of polyol recycling are quite rare^{6,7}.

Polyols can be categorized into polyether polyols or polyester polyols. Polyether polyols are produced by reacting epoxides with compounds rich in active hydrogen atoms. Polyester polyols are produced through the polycondensation reaction of multifunctional carboxylic acids and polyhydroxyl compounds. Additionally, these polyols can be further categorized by their molecular weights⁷.

Polyurethane is one of the most important and useful polyols given its applications in furniture and mattresses^{6,7}. However, the vast majority of furniture and mattresses end up in landfills. In fact, a study in Southeast England found that 10% of landfill volume could be attributed to mattresses⁶. Furthermore, polyurethanes are made by reacting polyhydric alcohols with molecular weights of 200-20,000 and functionalities which range between 2 and 8 with isocyanates. With the assistance of a catalyst, the NCO functional groups within the isocyanates help to create urethane/urea linkages, resulting in the formation of polyurethane⁷.

1.3.1 Thermal Cracking of Polyurethane

There are numerous studies that examine polyurethane and its decomposition during pyrolysis^{6,61–65}. The reaction mechanism for a polyurethane pyrolysis reaction is quite complex. However, there are many characteristic changes that occur during said reaction. These changes can be observed in Figure 1.11, which displays two IR spectra of polyurethane during decomposition in an N₂ atmosphere⁶.

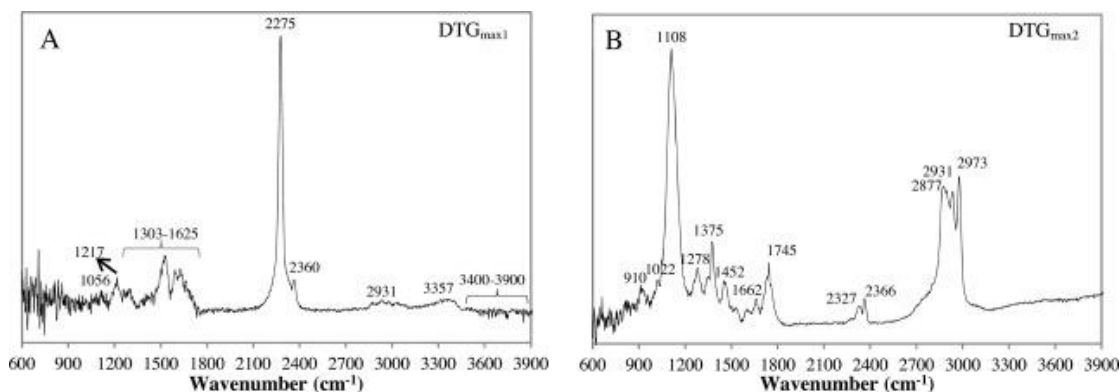


Figure 1.11: IR spectra of decomposing polyurethane at 300 °C (A) and 397 °C (B) in N₂ atmosphere at 30 °C/min⁶

In the A spectrum of Figure 1.11, peak 3357 cm⁻¹ represents the stretching vibration of N-H while the stretching vibration of -CH₂- groups are presents at the 2931 cm⁻¹ peak; additionally, the symmetric and asymmetric bands of C-O-C aryl alkyl ethers can also be observed at peaks 1056 cm⁻¹ and 1217 cm⁻¹. The mass of peaks observed from 1303-1625 cm⁻¹ and 3400-3900 cm⁻¹ are indicative of the presence of water vapor. Similarly, the presence of CO₂ can be observed at the 2360 cm⁻¹ peak. From these peaks, it can be concluded that the thermal degradation of polyurethane begins with the breakage of urethane bonds in an inert atmosphere. The rupturing of hard segments aligns with the formation of isocyanates (-NCO) which is observed to have an intense peak at 2275 cm⁻¹

⁶.

In the B spectrum of Figure 1.11, the peaks present at 2973 cm^{-1} , 2931 cm^{-1} , and 2877 cm^{-1} represent the vibration stretching of $-\text{CH}_3$, CH_2 , and $-\text{CH}$ groups, respectively; it should also be noted that these peaks have a strong, positive correlation with increasing temperature. The peaks present at 1022 cm^{-1} and 1278 cm^{-1} represent the symmetric and asymmetric absorption band of C-O-C in alkyl aryl ethers. The peaks at 910 cm^{-1} , 1375 cm^{-1} , and 1452 cm^{-1} are indicative of the formation of tert-butyl groups ($-\text{C}(\text{CH}_3)_3$). CO_2 bands are once again present at the 2366 cm^{-1} and 2327 cm^{-1} peaks. Additionally, the peak at 1662 cm^{-1} represents the presence of various types of ethers. The strongest peak can be observed at 1108 cm^{-1} , which represents the stretching vibration of C-O-C bonds from ethers of high polarity. In conclusion, the second stage of the decomposition of polyurethane is primarily comprised of the decomposition of the ether polyols produced during the first stage into products with methyl, methylene, methine, C-O-C/carbonyl groups, and CO_2 ⁶.

1.3.2 Catalytic Cracking of Polyols

One of the first promising recycling paths for polyols was demonstrated in a patent produced by A. Gaffney et al., which displays some promising results regarding the catalytic treatment for polyether polyol waste to produce valuable, petrochemical products, as displayed in Figure 1.12²⁸. In the patent, a fluidized bed reactor is used to produce the results displayed in Figure 1.12. Catalyst A, listed in Figure 1.12, is a ZSM-5 based catalyst. Nitrogen and steam were bubbled through a catalyst and plastic mixture within the reactor. Unfortunately, the patent does not directly state the polyol used, but describes the polyol as having an average molecular weight (MW) of 440; although based on the reaction products, it is likely that the polyol primarily consisted of polypropylene glycol²⁸.

Regardless, Figure 1.12 indicates a significant potential for the deconstruction of waste polyols into propionaldehyde, given its 81.6 wt% in the product gas²⁸.

Figure 1.12: The products of the catalytic cracking of polypropylene glycol in an FCC unit²⁸

TABLE I

Product ¹	Wt % Yield Example #			
	1	2	3	4
Methane	0.3	0.1	0.2	0.1
Ethane	0.1	0.2	Trace	0.2
Ethylene	0.04	0.4	0.4	0.7
Propane	0.2	0.1	0.1	0.2
Propylene	1.4	1.3	1.8	1.8
Acetaldehyde	4.3	1.0	0.9	0.7
Propionaldehyde	2.7	61.3	81.6	39.8
Acetone	1.9	1.6	2.1	1.0
1,4-Dioxane	Trace	0.6	4.2	1.7
Propylene Oxide	0.01	0.02	0	0.3
n-propanol	0.2	0.84	2.7	0.9
i-propanol	0.4	0.01	0.03	0.01
Propylene Glycol	0.9	1.5	2.5	1.7
Dipropylene Glycol	1.7	3.1	0.8	0.5
Dioxalane	0.1	2.1	2.3	2.1
Lower MW Polyols ²	79.5	20.2	0	37.6
G.C. lights ³	6.1	5.0	2.1	10.1
CO ₂	0.1	0.3	0.4	0.3
Coke	0.1	0.3	1.3	0.3
Catalyst	None	A	A	A
Temp, °C	450	450	450	450
Vol % Steam	10	10	10	33
in N ₂ Stream				
Method ⁴	Drop-in	Drop-in	Premix	Drop-in

1.3.3 Thermal Cracking of Polyols

Despite the lack of literature involving catalytic cracking of polyols, there exists several studies which investigate the thermal decomposition of polyurethane^{6,61–65}. However, given the polyol most likely used in the patent, polypropylene glycol, the reaction mechanism for the thermal decomposition of propylene glycol is far more insightful. Shown in Figure 1.13, the proposed decomposition schematic illustrates the dehydration of propylene glycol (1) to 2-propen-1-ol (5) or dehydration to form propylene oxide (2). Propylene oxide acts as the intermediate for the further decomposition of itself to acetone (3) and propionaldehyde (5). It was also concluded from this study that only 0.1% of propylene glycol decomposed due to kinetic limitations; however, it was found that most of the resulting decomposition products primary consisted of propionaldehyde⁶⁶.

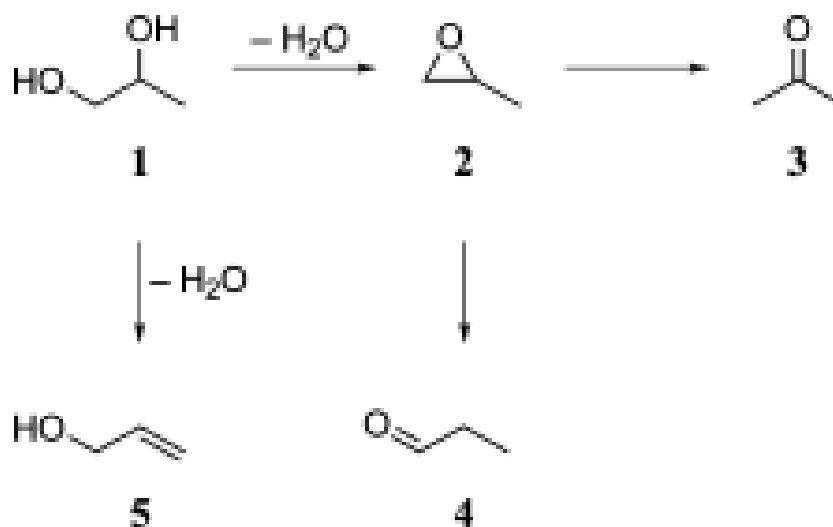


Figure 1.13: Pyrolysis of propylene glycol reaction schematic⁶⁶

1.4 2-D Mordenite Framework Inverted (MFI) Zeolite Nanosheets

2-D mordenite framework inverted (MFI) Zeolite nanosheets were synthesized and fully characterized by E. Naranov et al. in accordance with the surfactant synthesis outlined by M. Choi et al. Additional papers also outline similar procedures for the synthesis these nanosheets^{67,68}. Regarding the procedure followed by E. Naranov et al., the synthesized zeolite nanosheets then underwent a calcination of 6 hours in air, H-form through ammonium nitrate exchange for 4 hours, and then a drying and calcination for 3 hours⁶⁷. The number of these 12-hour cycles directly defines the name of the zeolite nanosheets discussed below. Figure 1.14 displays A) the small-angle PXRD patterns and B) the wide-angle PXRD patterns for the 2-D MFI zeolites during synthesis, which have similar patterns to that of MCM-41 and ZSM-5 due to their MFI structure⁶⁹. It is also worth noting that MCM-41 has been shown to have excellent reaction selectivity and selectivity enhancement when paired with a ZSM-5 catalyst⁴⁸. Part C of Figure 1.14 represents N_2 adsorption isotherms, which indicate that at low pressures ($P/P_0 < 0.4$) the observed

isotherms correspond to microporous materials while the high changes in adsorption, in the high-pressure regions, indicate a pore irregularity. It has been observed that ZNS-HT-48 contains both micropores as well as mesopores, which are indicative of a structural transformation; this claim is also supported by part D of Figure 1.14 which represents the overall spread of the pore diameters found within the structure. Part A of Figure 1.14 is also indicative of low levels of crystallinity within the mesostructured ZNS-HT-12, due to the lack of peaks; however, the peak returns at 24 hours, indicating the presence of the MFI crystallite. At 36 hours, the peak once again disappears, but returns at 48 hours, where the fully crystalline structure with ultrathin nanosheets is detected.

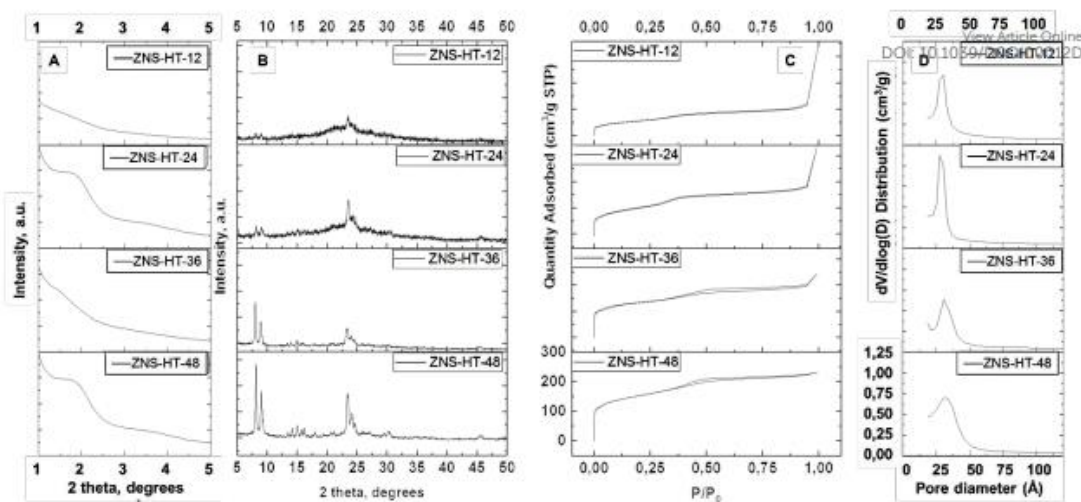


Figure 1.14: Characterization of 2-D MFI zeolite nanosheets A) small-angle PXRD patterns B) wide-angled PXRD patterns C) N_2 adsorption isotherms (C) pore size distributions of MFI zeolite nanosheets⁶⁷

Figure 1.15 provides a schematic of the structural changes that take place during the 48-hour period to produce the MFI nanosheets. Initially a structure like that of MCM-41 is visible, which is then disordered, unfolded, flattened, and reordered to form MFI nanosheets⁶⁷.

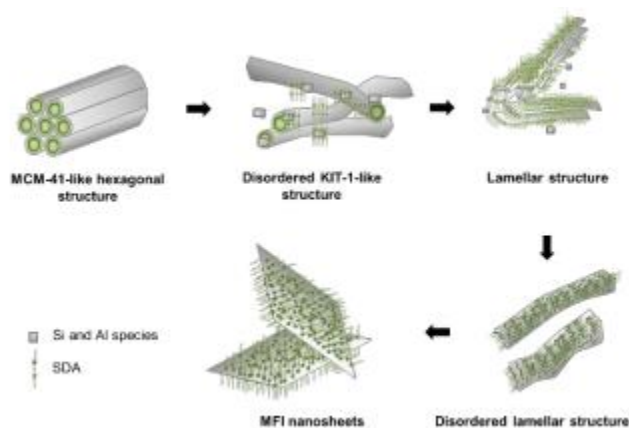


Figure 1.15: MFI nanosheet crystalline structure changes throughout the four 12-hour cycles⁶⁷

As Figure 1.15 implies, there is a large increase in the number of acid sites on the zeolite as time moves forward. The unfolding effect observed in Figure 1.15, allows the surface of the zeolite to facilitate acidic sites, which may significantly reduce internal mass transfer limitations presented in porous zeolites. Through the examination of Figure 1.16, it is concluded that this is indeed the case. The absorption band at 1545 cm^{-1} is due to interaction of pyridine on Brønsted acid sites while the absorption bands around 1455 cm^{-1} indicate the interaction of pyridine with Lewis acid sites⁶⁷.

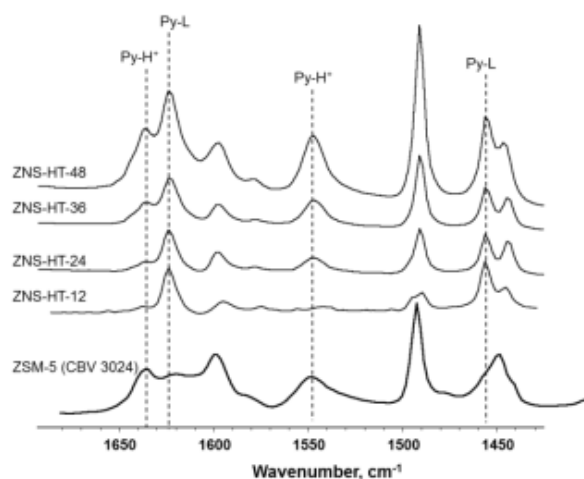


Figure 1.16: FTIR spectra of ZSM-5 and MFI nanosheets at various synthesis times⁶⁷

As shown in Figure 1.17, ZNS-HT-48 has highest number of Brønsted and Lewis acid sites, which would indicate a higher reaction selectivity, as discussed previously^{45,46,67}. As it turns out, this is indeed the case for the MFI nanosheets as well; as the number of Brønsted acid sites increases, so too does the reaction selectivity, as shown in Figure 1.17.

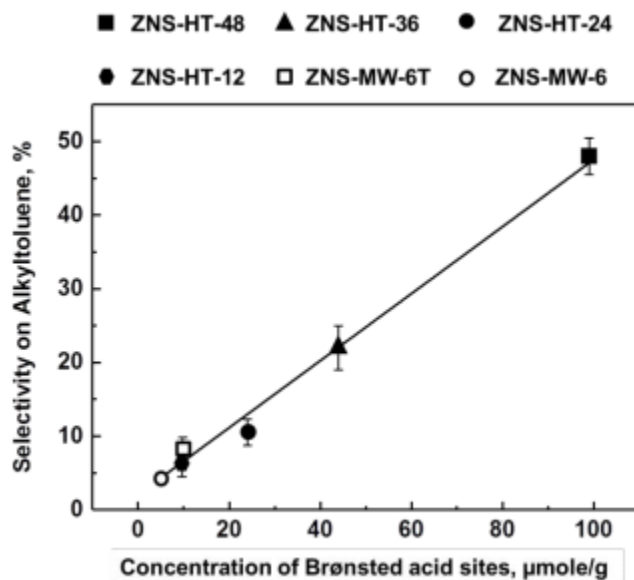


Figure 1.17: Selectivity of Alkyltoluene versus the concentration of Brønsted acid sites on the MFI nanosheets throughout the four 12-hour cycles; note that ZNS-MW-6T and ZNS-MW-6 zeolite nanosheets were nanosheets synthesized through microwave irradiation⁶⁷

2-D MFI nanosheets are also easily identifiable through scanning electron microscopy (SEM) imaging, as displayed in Figure 1.18. Clear ball-like clusters can be seen in Figure 1.18 in further distance images. However, closer imaging reveals the floral like structures of these ball-like clusters. The “petals” of these structures represent the 2-D MFI zeolite sheets⁷⁰.

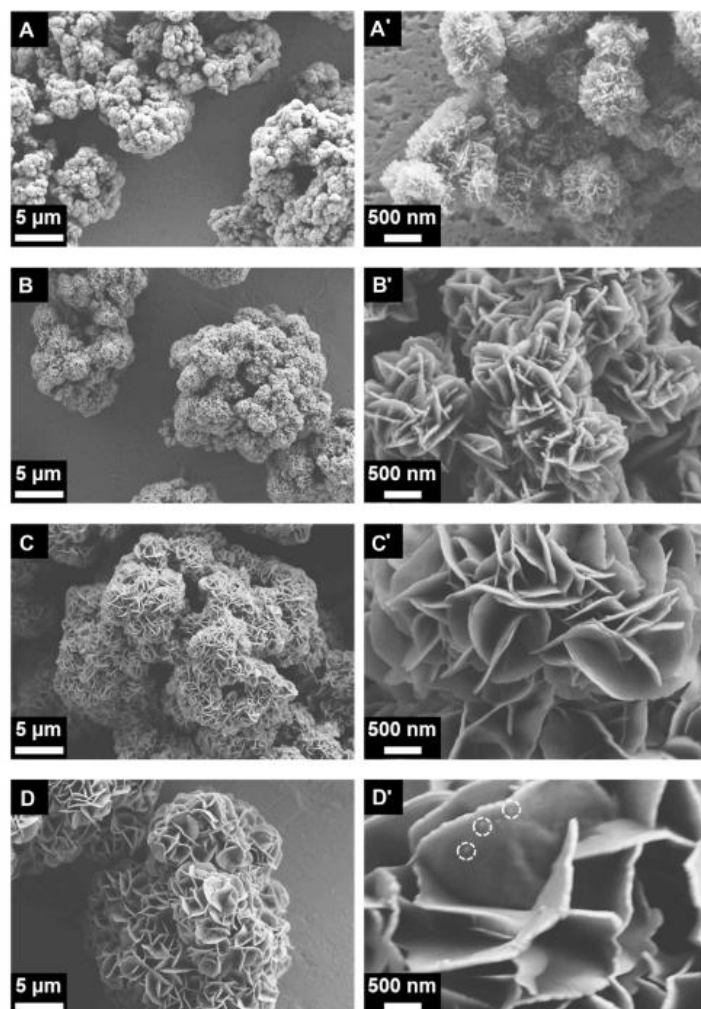


Figure 1.18: SEM images of 2-D MFI zeolites⁷⁰

CHAPTER 2

EXPERIMENTAL METHODOLOGY

2.1 Reactor System Setup

A reactor system was designed and built to test the catalytic cracking of waste polyol plastics. The reactor system was primarily built from a combination of 316 stainless steel tubing and fittings of various sizes. In total, the reactor system was redesigned three times: version 1.0, version 2.0, and version 3.0. The following subsections discuss these three versions and their respective intricacies as well as the general design of the reactor itself. Overall, the reactor system can be categorized as a semi-batch, plug-flow reactor system.

2.1.1 Reactor Tube

The general design of the reactor tube, as seen in Figure 2.1, did not change from version-to-version. However, the size of the tube and loading amounts were varied and are to be discussed in the following subsections as well. The reactor tube is a 30 cm 316 stainless steel tube that is positioned vertically and encapsulated within a tube furnace. Originally, a vertically positioned reactor tube stemmed from the idea of an FCC unit, as discussed within the introduction. However, given the flow rate limitations imposed upon the system, fluidization of the bed was unsuccessful. This was verified using a quartz tube, as seen in Figure 2.1, which was produced in Chemix. Figure 2.1 displays the polyol, the slightly green viscous liquid, on top of the zeolite catalyst and sandwiched in between two pieces of quartz wool. The polyol used is typically clear; however, it was mixed with an

inert salt, nickel (II) chloride, for visual representation. Although a quartz tube provides a visual outlook on the reaction, a stainless steel tube was chosen due to the stability it provided, as many quartz tubes were broken during the initial experimentation. The tube is first loaded with a support rod, which enables precise catalyst bed placement regarding the thermal couple. The thermal couple is introduced into from the top of the reactor tube and sits approximately in the middle of the tube; this thermal couple allows accurate bed temperature readings, as the furnace thermal couple can result in drastically different values from the setpoint depending on the set temperature. A piece of quartz wool is then inserted and flatted with another piece of tubing on top of the support rod; this flattened piece of quartz wool is to act as the bottom of the catalyst bed and prevent any catalyst/reactant from escaping the bed. A set amount of mixed catalyst and polyol is then added to the reactor tube, which is followed by another piece of quartz wool to keep the bed in place. The loaded reactor tube is then situated between two fittings and tightened on the top and bottom to prevent any possible leaks.

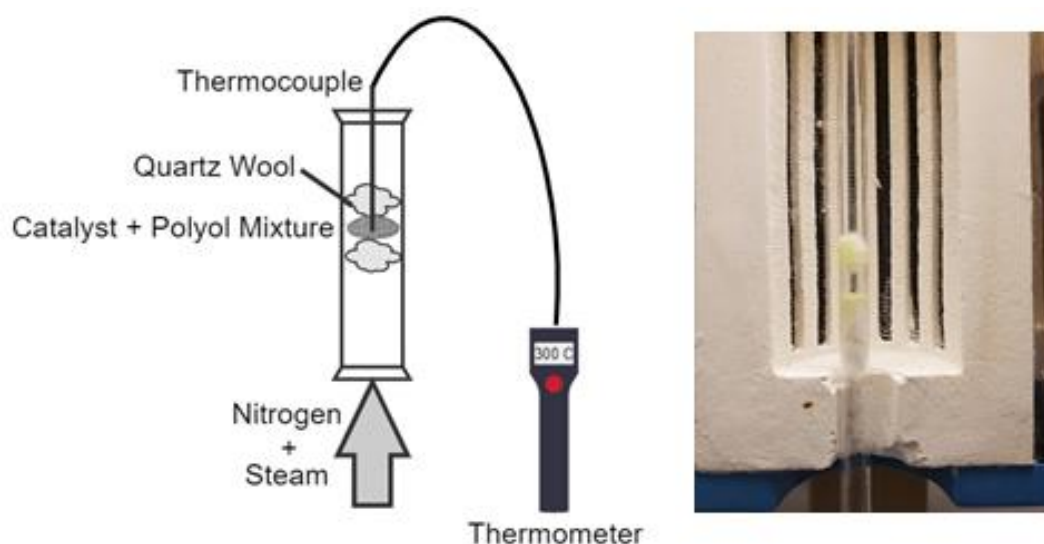


Figure 2.1: Side view of the reactor tube

2.1.2 Reactor Setup Version 1.0

The initial version of the reactor system was closely based on the previously discussed patented process for polyol decomposition, as seen in Figure 2.2²⁸. The primary goal of this setup was to validate the results presented in the patent. Thus, version 1.0 employed the use of an evaporator, reactor, condenser, and a gas chromatograph (GC) for analysis Figure 2.1, which was produced in Chemix. An HPLC (high-performance liquid chromatography) pump was used to pump water from a reservoir, a 1 L Erlenmeyer flask, into a large stainless steel tubing of ½” outer diameter (OD); additionally, inert gas, nitrogen, was introduced at the top of said tube. The HPLC pump was first calibrated for several different lower end flow rates over a large range of time, over 30 hours, to create an adjustment for the setpoint vs. the actual flow rate. This calibration was achieved through a mass-based calibration using water. The nitrogen gas flow rate was regulated using a mass flow controller (MFC) of 200 mL maximum flowrate using an MFC controller box. The MFC was also calibrated using a giliblator to adjust the setpoint for the actual flow rate. 1/16” 316 stainless steel tubing was plumbed from the HPLC pump into a series of bored fittings and expanding fittings into the evaporator. The water was introduced about halfway inside of the tube to prevent potential backflow and better mixing. The tube was also slightly angled downward to also help mitigate potential backflow and pooling of water within the tube. The stainless steel tube was filled with stainless steel beads, which acted to provide additional mixing properties for the nitrogen and steam mixture. The stainless steel beads were also hypothesized to increase the overall heating effectiveness of the evaporator, given their thermal conductivity properties. The stainless-steel beads were placed through the top of the condenser before tightening the fittings and were held in place

with a piece of quartz wool at the end of the tube. The tube was wrapped with rubber heating tape and then wrapped with aluminum foil, which allowed for a more uniform heating distribution. The resulting creation acted as the evaporator for all versions of the reactor system. The evaporator operated at temperatures over 120 °C and resulted in what is assumed to be a well-mixed carrier gas feed comprised of steam and nitrogen. The carrier then flowed through ¼” stainless steel tubing, which was heated in a similar manner to the evaporator, directly to the reactor tube itself. Along the way to the reactor, a pressure gauge was introduced to allow for pressure monitoring of the system. This became extremely important in later versions of the reactor system for identifying system plugging. In version 1.0, the reactor tube was a ½” 316 stainless steel tube, which is held in place with two Swagelok® ultra-torr vacuum fittings, which are both sealed with a Viton® O-ring. Typically, these fittings are used with a quartz tube; however, they also provided a leak-tight seal with a stainless steel tube, which allowed for easy removal and replacement of the reactor tube. Eventually, the Viton® O-rings were replaced with polytetrafluoroethylene (PTFE) O-rings due to concerns of potential product reactivity and temperature limits. At this point, the reactor operated with 1.0 g of catalyst and 0.5 g polyol. The zeolite poured into the reactor tube on top of the quartz wool bed with a funnel, and then polyol was injected via a syringe down the tube onto the zeolite, resulting in the zeolite and polyol mix. Following the reactor, the Swagelok® ultra-torr vacuum fittings were connected to ¼” stainless steel tubing that flowed to the condenser. The condenser was comprised of two pieces of ¼” 316 stainless steel tubing that were curved to try and increase surface area exposure. These two pieces of tubing were connected to a cross fitting, which allowed for the connection of a ½” 316 stainless steel tube and a

thermocouple, which was situated at the center of the cross fitting. The ½” stainless steel tube, which was about 15 cm in length and closed at the bottom with a ½” stainless steel nut, allowed for the collection of any potential condensate. The entire condenser and the lines leading up to said condenser from the reactor were wrapped in a similar fashion as the evaporator. The thermocouple placed inside the condenser allowed for an accurate reading on the temperature within the condenser. The condenser was heated to about 60 °C to condense all the water out of the system while leaving any volatile products. This was then followed by ¼” 316 stainless steel tubing, which also was connected to two particulate filters to protect the GC instrument from possible plugging from escaped quartz wool or catalyst particles from the reactor. The first particulate filter contains a 2 micron pore size filter while the second particulate filter contains a 0.5 micron filter. All the ¼” tubing leading up to the GC, including the two particulate filters, were heated in a similar manner to the evaporator. Additionally, the outlet of the GC was also wrapped and heated to prevent any plugging of condensing products after leaving the GC. This outlet line was introduced into a beaker of water, which allowed for proof of flow through the system from the resulting bubbles.

There were many issues with this version of the reactor setup. The primary issue faced was a closed mass balance. Almost no condensate was collected from the condenser, which means the condenser needed to be reworked to remove the water from the system. Only after about 5 runs could any quantifiable condensate be collected from the condenser outlet. Additionally, water droplets were observed being expelled through the GC outlet. Although water is not necessarily quantifiable in the GC, as will be discussed later, it can

potentially cause damage to the GC column⁷¹. Regardless, the system needed to be reworked, which led to reactor setup version 2.0.

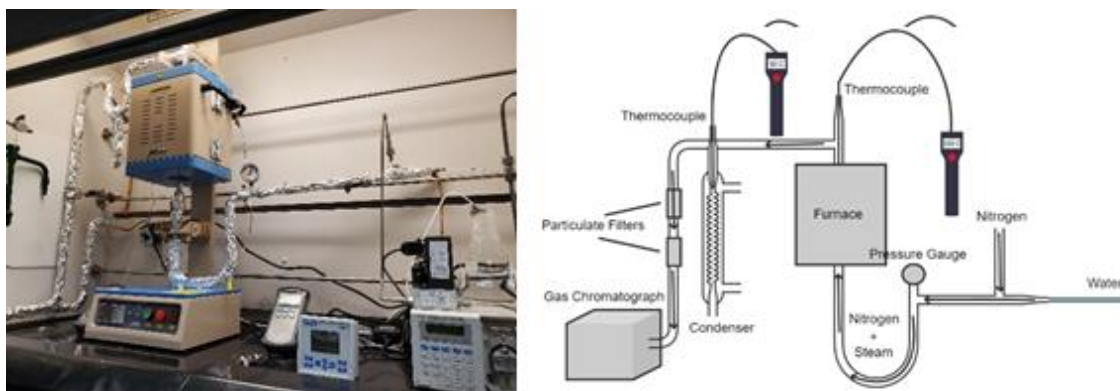


Figure 2.2: Reactor setup version 1.0

2.1.3 Reactor Setup Version 2.0

Version 2.0 of the reactor system can be seen in Figure 2.3. The overall design of version 2.0 was very similar to that of 1.0. The general design of the reactor system before the reactor was same as in version 1.0, apart from minor modifications. The first minor modification that was implemented was the replacement of the stainless steel beads in the evaporator with glass beads. After numerous runs, the flow out of the evaporator become almost non-existent. As it turned out, the stainless steel beads had been corroding, which resulted in small, oxidized metal flakes to build up within the quartz wool outlet and plug the evaporator. As such, the stainless steel beads were removed and replaced with inert, glass beads. Additionally, the quartz wool was removed and replaced with a steel frit in order to mitigate the potential migration of contaminants from inside of the evaporator to the reactor. The steel frit was hammered into a ¼” stainless steel tube that was connected to the end of the evaporator, which primarily served to contain the glass beads within the evaporator. The last minor modification was the replacement of the rubber heating tape

with high-temperature heating tape made from quartz fabric. Due to overwrapping and overheating of the rubber heating tape, the rubber became very brittle and cracked along with the heating wire it contained; thus, rendering the heating tape useless and unable to heat. This issue was especially pertinent within the evaporator which required higher temperatures to ensure the evaporation of the water. As such, several variable transformers were required to facilitate use of the high-temperature heating tape, as seen in Figure 2.3, which was produced in Chemix. The high-temperature heating tape was wrapped with aluminum foil, allowing for more uniform heat distributions of the wrapped tubing. Additionally, the line leading to the condenser was also replaced with high-temperature heating tape as opposed to rubber heating tape.

The most important modification made to version 1.0 was the complete redesign of the condenser. The old condenser was completely scrapped and a new one that sought to condense all products and reactants was designed. Surface area exposure was key to overcoming this challenge; thus, the condenser was comprised of two pieces of 1/8" 316 stainless steel tubing that were about 180 cm in length. These two pieces of tubing were coiled and connected to the right and left side of a cross fitting. Much like the first condenser, a thermocouple was fed into the top of the cross fitting and situated in the center of said fitting. The bottom of the cross was once again connected to a 1/2" stainless steel piece of tubing of about 15 cm in length, which was now closed using a 1/2" switching valve. Prior to the connection of the switching valve, the entire condenser was lowered into a plastic bucket. A hole was drilled into the bottom of the bucket of about 1/2" OD, where the 1/2" stainless steel tube was slipped through. The switching valve was then secured at the bottom, locking the condenser into place with the bucket. The slight cracks between

the tubing and the bucket were sealed using adhesive. Once the adhesive dried, the bucket was filled with a solution of antifreeze, which consisted of a 40% water and 60% ethylene glycol mixture by volume. The bucket and condenser was situated next to the reactor and supported with steel scaffolding. A chiller is used to circulate the antifreeze solution to reduce the temperature. The chiller is set to its lowest setpoint, 35 °F, which allowed the condenser to reach temperatures of about 2 °C. The cold inlet for the chiller is situated at the bottom of the bucket while outlet is situated at the top in an attempt to make use of natural convection. By immersing the condenser in the antifreeze solution, it allowed for the maximum amount of heat transfer to occur as opposed to wrapping the condenser with tubing that circulated cooling fluid. The 1/8" stainless steel coils were attached connected to the rest of the system at the bucket.

After the condenser, the same 1/4" stainless tubing wrapped in rubber heating tape transported the remaining gases to a switch valve that was connected to a gas bag. The gas bag was used to collect any uncondensed product. The gas bag and the condensate that resulted from reaction were analyzed using a gas chromatography mass spectrometer (GC-MS).

The mass balance had significantly improved from version 1.0; however, it still did not come close the desired >95% closure with repeated experiments. Thus, three modifications were made in an attempt to improve the overall condensation and precision of the reaction. The first modification involved pre-mixing the catalyst and polyol prior to addition to the reactor tube. There were a number of inconsistencies with the condensate being capture, so it would stand to reason that these may stem from inconsistencies with external mass transfer limitations within the reactor⁷²⁻⁷⁴. Upon introducing the pre-mixed

methodology, the results became more consistent by adding 1.5 of pre-mixed catalyst and polyol (2 to 1 catalyst to polyol ratio). However, there were still very broad ranges of condensation collection. Thus, it was decided to increase the amount of pre-mixed polyol that would be added to the reaction to minimize the experimental error and remaining residual products within the reactor system. However, the current tube could not facilitate additional catalyst and polyol mixture; thus, a 1" OD reactor tube of the same length was prepared and employed. Unfortunately, Swagelok® ultra-torr vacuum fittings had to be replaced with regular fittings that had to be tightened and loosened with large wrenches. Regardless, with the implementation of a larger reactor tube, experimental runs consisting of 5 g of pre-mixed catalyst and polyol were used thereafter. These larger pre-mixed runs were able to drastically reduce the inconsistencies from run to run; however, the mass balance still did not exceed the desired 95%. Therefore, it was decided to lengthen the coils within the condenser itself. Instead of 180 cm coils, 360 cm 1/8" stainless steel coils were used. Despite this modification, no additional improvements in the mass balance were seen. In fact, since the inner diameter (ID) of longer coils was smaller than that of the 180 cm coils, problems with flowrates become a noticeable concern. It was observed that the smaller ID coils could not ensure an unhindered flow of gas, resulting in a slight pressure buildup within the system. Thus, it was decided that the 180 cm coils would be better choice for the system overall. However, this still resulted in difficulties with the mass balance closure; thus, version 3.0 of the reactor system was designed to achieve the desirable mass balance closure of over 95%.

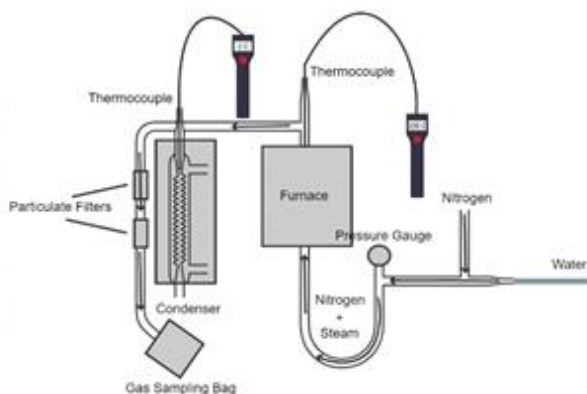
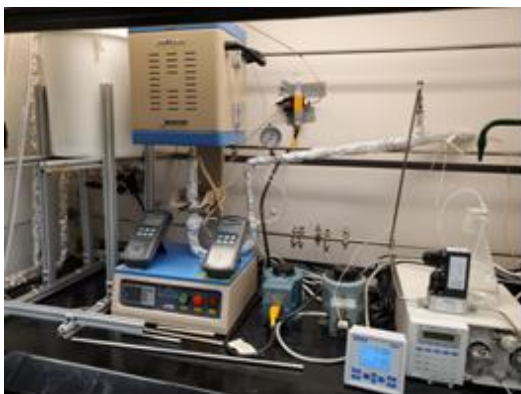


Figure 2.3: Reactor setup version 2.0

2.1.4 Reactor Setup Version 3.0

Reactor setup version 3.0 can be seen in Figure 2.4. The only objective of this design of the reactor system was to obtain a desirable mass balance closure of over 95%. Given the modifications to version 2.0, it seemed as though the improvement of the current condenser was not a viable option for closing the mass balance. Since the temperature of the first condenser could not fall below 0 °C, as the water within it would freeze, lowering the temperature of the condenser was not a viable option. The only two foreseeable options were to either design the condenser once again or add another condenser. If another condenser was added to the setup, then it could operate at significantly lower temperatures than the first condenser, assuming the first condenser is successfully able to condense out water and other higher boiling point products from the product stream. Thus, it was decided to try adding a secondary condenser that would operate in series with the other one to improve the mass balance closure.

Much like the first condenser, the idea was a coiled condenser submerged in a cooling liquid. This time a small tee cross was used with two 1/8" coils of about 20 cm in length. The bottom part of the condenser, where the liquid would be held, was 1/4" tubing with a 1/4" switching valve. The body of the condenser was a stainless steel tissue holder

from Walmart, which was welded to a stainless steel plate to close off the bottom of the condenser. A hole about 1/4" was drilled into the bottom of the stainless steel plate, and once again, the 1/4" stainless steel tubing was inserted and secured into the plate with the 1/4" switching valve. Despite an attempt to seal the bottom of the new condenser with adhesive, it began to leak quite quickly due to the operable temperature limit of the adhesive; therefore, the 1/4" tubing had to be welded to the steel plate. This allowed the condenser to be leak proof and it was filled with acetone, which has a very low freezing point of -95.35 °C⁷⁵. Thus, the condenser could theoretically cool the product gas to said temperature with ease. The condenser was also wrapped with absorbent pads in an attempt at insulating the condenser. The acetone within the condenser is then cooled to about -60 °C with liquid nitrogen or dry ice. The condenser typically heats up to be about -40 °C at the conclusion of an experimental run. The temperature is monitored via a thermal couple that is submerged in the acetone bath itself, as there was a limited amount of space within the condenser itself.

No additional modifications were made to the remaining part of the reactor system. The gas bag was then sampled at the end of the second condenser instead of the first. However, with this new modification of a secondary condenser, a mass balance closure of over 95% was achieved. Thus, the final version of the working reactor system, displayed in Figure 2.4 which was produced in Chemix, includes the usage of an evaporator that produced a carrier gas stream of steam and nitrogen, which flows through a semi-batch plug flow reactor. The resulting catalytic cracking products from 5 g of mixed polyol and zeolite is condensed through a series of two condensers. Through this system, a mass

balance closure of over 95% is achievable with only liquid condensate as the concern for the quantification.

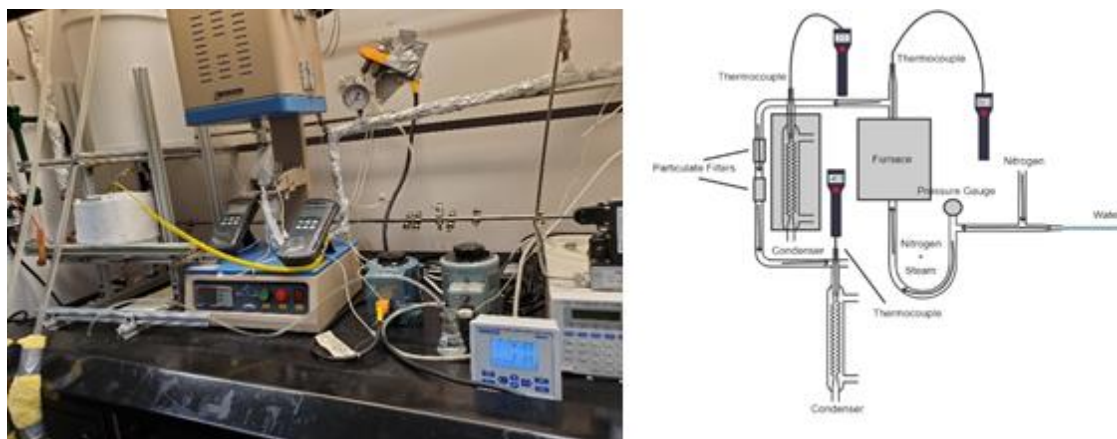


Figure 2.4: Reactor setup version 3.0

2.2 Reaction Materials

Although numerous catalysts and polyols were tested in the setup, the following sub-section will primarily focus on the usage of $\text{NH}_4\text{-ZSM-5}$ as the catalyst and polypropylene glycol Mn ~425 as the reactant polyether polyol. Zeolyst provided the $\text{NH}_4\text{-ZSM-5}$ catalyst, which is their CBV 5524G product that has a $\text{SiO}_2/\text{Al}_2\text{O}_3$ molar ratio of 50:1 and a surface area of $425 \text{ m}^2/\text{g}$ ⁷⁶. The catalyst was primarily used out of the container as $\text{NH}_4\text{-ZSM-5}$ unless otherwise specified. The polypropylene glycol was purchased from Sigma Aldrich. Several different zeolite catalysts were also used as well as other polyols such as polyethylene glycol and polyurethane. Polyethylene glycol Mn ~8000 was also purchased from Sigma Alrich while the polyurethane samples (Texin® 950 D) were provided by Covestro. The usage and results of these different zeolites and polyols will be further discussed in the Experimental Results section.

2.3 Product Gas Analysis

2.3.1 Reactor Setup Version 1.0 Product Analysis

The diagram illustrates a gas chromatography system with the following components and flow paths:

- Carrier Gas Source:** A 500 µL Carrier 1 reservoir connected to an AFC (Automatic Flow Control) valve.
- Flow Path:** The carrier gas flows through a series of components: a TCD REF Gas detector, a Carboxen column, a Q Plot detector, and an I.C.D. (Internal Combustion Detector).
- Detectors:** The system includes a TCD REF Gas detector, a TCD MUP (Molecular Understanding Probe), and two FID (Flame Ionization Detector) units (Left FID and Right FID).
- Control and Inlets:** The system is controlled by a Pres Reg/Rstrctr (Pressure Regulator/Restrictor). Air H₂ inlets are provided for the FID detectors.
- External Transfer Line:** An External heated transfer line is connected to the system, likely for sample introduction.

38

The TCD and FID chromatograms of one of the first experimental runs are displayed in Figure 2.6. As seen in Figure 2.6, the FID primarily consists of two large peaks with many smaller trailing peaks around the 2 and 3 retention time while the TCD also consists primarily of two large peaks. The column oven was heated to 150 °C and kept constant throughout the run, which totaled 15 minutes. This experimental run utilized a reaction temperature of 440 °C, a catalyst to polyol ratio of 2:1 with a total mixture mass of 1.5 g, and a steam percentage of about 20% with a total flow rate of about 25 mL/min.

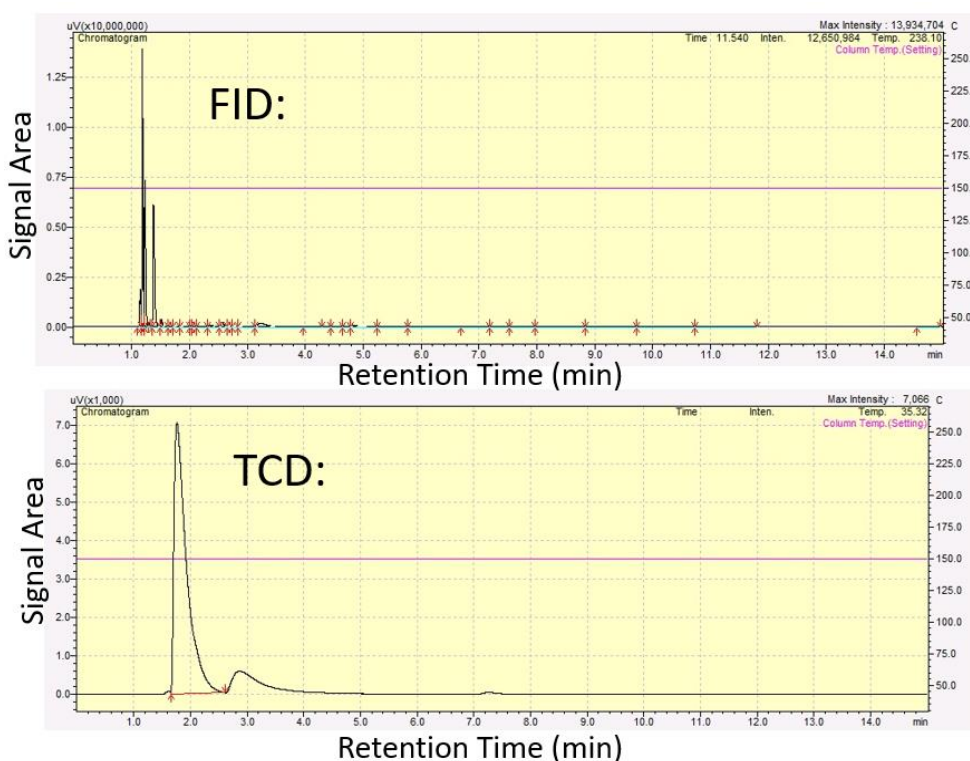


Figure 2.6: TCD and FID chromatogram of preliminary data from the GC analytical setup used in version 1.0 of the reactor

Although the patents provided some guidance as to the possible products being produced, it was necessary to verify these potential products through the use of a GC-MS system. A sampling gas bag was connected to the outlet of system to be collected for the GC-MS. This sampling gas bag was sampled with a gas-tight syringe and injected into a

2010 Shimadzu GC-MS via an injection port at the top of the GC-MS. The chromatogram for the vapor product is displayed in Figure 2.7. The GC-MS utilized a RTX-1701 capillary column with a constant oven setpoint temperature of 150 °C with a total time of 8 minutes. The detector used in the GC-MS system is the mass spectrometer portion of the GC, which was connected to the Nuclear Science and Technologies (NST) database for easy compound identification. Additionally, the carrier gas used for the GC-MS system is helium. Majority of the peaks appeared within the first 3 minutes of the run, as seen in Figure 2.7. As seen in Figure 2.7, there exists one large peak, belonging to that of propionaldehyde. The other small peaks within the run were identified as propanoic acid; 1,3-dioxolane, 2-ethy-4-methyl; and 1,4-dioxane, 2,-dimethyl. However, the quantities of these other products were negligent.

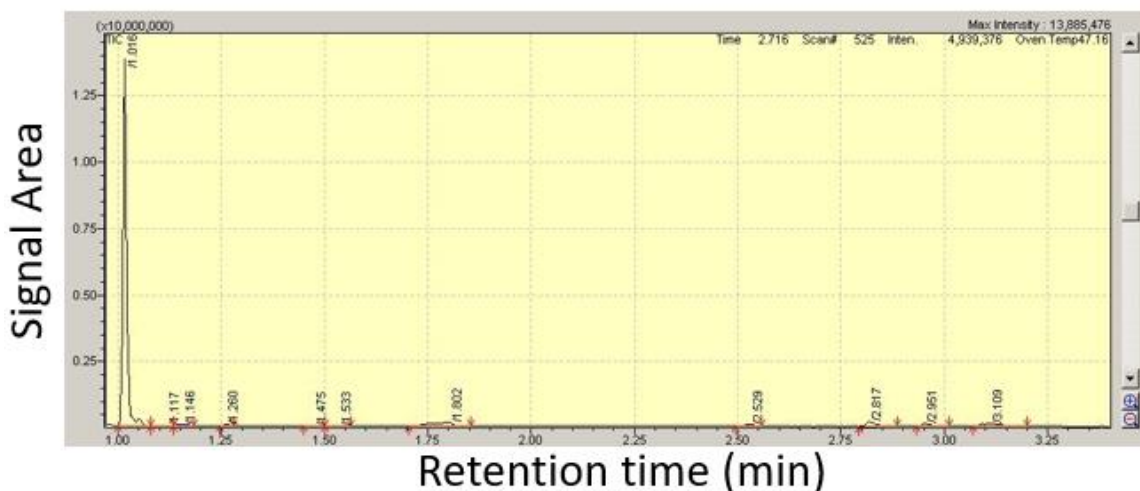


Figure 2.7: The GC-MS chromatogram for the product gas of version 1.0 of the reactor system

After several preliminary runs had been conducted using the reactor system, a slight amount of condensate was able to be collected from the condenser. This condensate was also injected into the GC-MS, as seen in Figure 2.8. The column oven was heated and held once again at a constant 150 °C, but for a total time of 17 minutes for the condensate. The

initial peak resembles a mass spectrometer saturation due to the high amount of water within the same, but the other peaks resemble acetone, propylene glycol, 1-propanol, and 2-propanol methyl-.

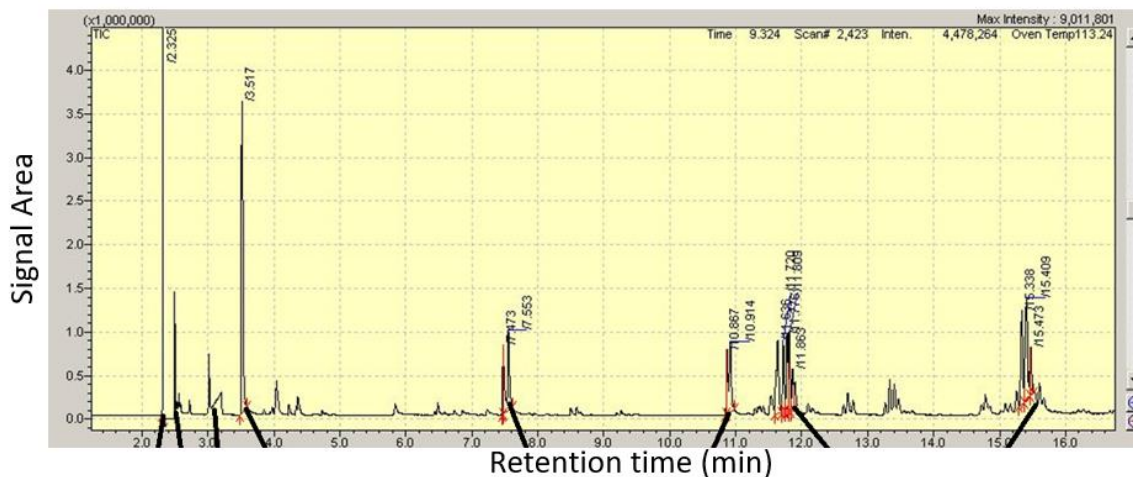


Figure 2.8: GC-MS chromatogram for the condensate of version 1.0 of the reactor system

With the identification of the condensate and vapor products complete, the focus was returned to the original GC system with the dual detector setup. The next step for this process was to quantify the primary products from the reaction. This was accomplished by external calibration for propionaldehyde in the FID as well as nitrogen in the TCD. At first, a solution of known concentration of propionaldehyde was injected into the injection port of the GC; however, after many iterations, it was clear that something was not working correctly, as the results were not even close to reproducible. Instead, it was decided to inject propionaldehyde directly into the evaporator via syringe pump at a known flow rate along with nitrogen; however, this once again did not yield reproducible results. The outcome was the same even after the evaporator had straight-piped to the GC, which involved directly linking the evaporator to the GC. This was done in an attempt to mitigate potential experimental error due to cold spots within the system. Additionally, the small 1/16" lines

connected to the switching valve of the GC system were wrapped with heating tape in case propionaldehyde was condensing there. However, this still did not alleviate the inconsistencies within the results. By accident, it was discovered that one of the syringes that was being used in the syringe pump to deliver propionaldehyde to the system seemed distorted and discolored. As it turns out, propionaldehyde was reacting with the rubber seal of the syringe being used. Therefore, a PTFE syringe was ordered specifically for pumping propionaldehyde into the system. With this change, the results finally became reproducible and a calibration curve for nitrogen with the TCD and a calibration curve for propionaldehyde with the FID were constructed as seen in Figure 2.9.

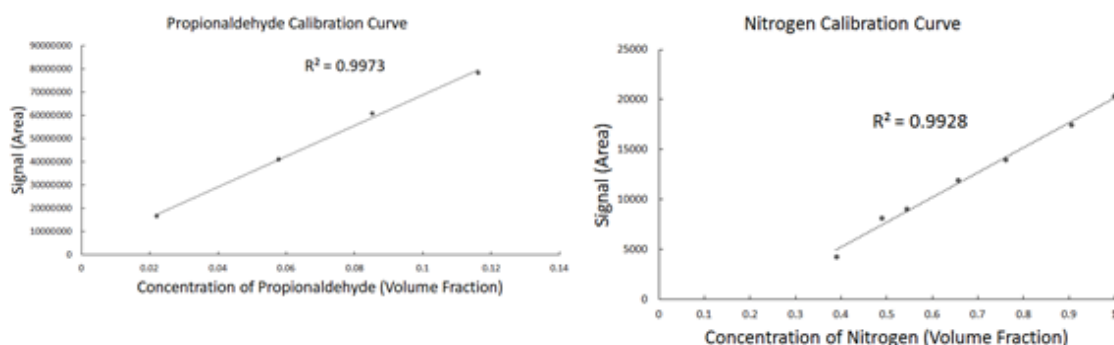


Figure 2.9: GC calibration curves for propionaldehyde and nitrogen used in version 1.0 of the reactor setup

Using these calibration curves, a volume fraction for nitrogen, propionaldehyde, and other products was able to be developed. The idea was that the volume fraction for propionaldehyde plus the volume fraction for nitrogen plus the volume fraction of the other products should equal one. Using this equation, one was able to calculate the volume fraction selectivity of propionaldehyde for the product gases. Preliminary results suggested propionaldehyde selectivity's above 60%, which were later further optimized through the usage of a design of experiments (DOE), as discussed in the experimental results section.

Additionally, it is important to understand that selectivity here refers to the adjusted quantification of products seen in the GC system. Using the calibration curves in Figure 2.9, a percentage of product gas was defined as propionaldehyde, and the remaining percentage defined as other products. Therefore, the selectivity of propionaldehyde refers to the amount of propionaldehyde with respect to the other observed product peaks.

Although the selectivity is important for this reaction, the yield of the reaction products is far more important. However, without a sufficient mass balance closure on the condenser and the vapor phase, there could be no quantification of yield for this process. Additionally, water droplets had been observed in the gas sampling bag, signaling a lack of condensation within the condenser itself. Thus, the reactor system had to be reworked, as previously mentioned, in addition to the analytical method for product quantification.

2.3.2 Reactor Setup Version 2.0 Product Analysis

Version 2.0 of the reactor sought to close the mass balance, as previously discussed. The first means of mass balance closure was a physical quantification of the liquid product mass as well as the amount of polyol and water put into the reactor system. A single run was repeated three times to get an idea of the general mass closure percentage as shown in Table 2.1. The run consisted of 50 mL/min of total flow, 20% steam in the carrier gas, a total mixed polyol and zeolite mass of 5 g, a catalyst to polyol ratio of 1:2, and reaction temperature of 310 °C. 10 mL/min of steam constituted around 0.324 g of water pumped into the system, from the earlier discussed calibration. Given the mixed polyol and zeolite mass and the ratio between the two, the total amount of polyol introduced into the system was 1.67 g. Once the reaction had run its course, over an hour period, condensate was collected from condenser and massed. Thus, the mass in is equal to the water pumped into

the system and the polyol introduced while the mass out is equal to the condenser mass, displayed in Table 2.1. The mass balance closure was then calculated by dividing the mass in by the mass out of the system. This resulted in all three runs having nearly 100% mass balance closure.

Table 2.1: Physical Mass Balance Closure of Version 2.0

Run	Total Water Pumped	Polyol Loaded	Mass In	Mass Out	Mass Balance Closure
1	0.324 g	1.67 g	1.994 g	1.981 g	100.66%
2	0.324 g	1.67 g	1.994 g	2.053 g	97.13%
3	0.324 g	1.67 g	1.994 g	1.969 g	101.27%

However, upon further calibration testing using the HPLC pump, it seemed as though there might be a large amount of experimental error introduced within these results. Thus, it was decided that a more in-depth quantification of the mass balance was necessary. The primary products of reaction would have to be identified and calibrated for within the setup. The quantification of the products was done solely using the GC-MS, as it provided better separation with the same column due to the use of a vacuum. Much like the product analysis for version 1.0, an RTX-1701 capillary column was used; however, the ramping temperature and mass spectrometer detection ranges were varied. Several runs were repeated, and the liquid effluent tested along with vapor phase that was captured in a sampling gas bag after the condenser. At this point in the system, there was solvent being used to dissolve the products in one phase; thus, the condenser had both an aqueous phase and an organic phase that was tested.

For the vapor phase, a ramp temperature of 30 °C was used to increase the column temperature from 40 °C to 200 °C after an initial hold at 40 °C for 2 minutes. The total time for this run was just over 7 minutes. The mass spectrometer scan range was set to 33-380 m/z for the first minute and 14-380 m/z for the remaining time. This was done to avoid seeing oxygen and nitrogen within the detector, as the vast majority of the gas sampling bag was comprised of nitrogen. The vapor phase yielded a number of products: carbon dioxide, propene, acetaldehyde, 2-pentene (E), 2-pentene (Z), ethanol, and propionaldehyde. The primary products in the vapor phase are displayed in Table 2.2, as well as their respective area percentages.

For the aqueous and organic phases of the condensate, an initial temperature hold at 40 °C was done for 3 minutes, followed by a temperature ramp to 80 °C at 20 °C/min. The 80 °C temperature was held for 2.5 minutes, which was followed by the final ramp to 150 °C to then be held there for additional 5 minutes. The total time of the run was about 16 minutes. A solvent cut time, to avoid saturating the detector with water, was implemented, and the mass spectrometer began scanning at 1.35 minutes for 14-380 m/z for the remainder of the run. The visible products present in these runs were as follows: propionaldehyde; acetone; 1-propanol; 2-propen-1-ol; 2-pentanone; acetol; 1,3-dioxolane, 2-ethyl-4-methyl-; pentanal, 2-methyl-; 1,3-dioxolane, 2-ethyl-4-methyl-; 1,4-dioxane, 2,6-dimethyl-; 1,4-dioxane, 2,5-dimethyl-; propanoic acid, 2-propenyl ester; propanoic acid; propanoic acid, propyl ester; 2,3-pentanedione, 4-methyl-; 1,4-dioxane, 2,5-dimethyl-; 1,4-dioxane, 2,5-dimethyl-; 2-ethyl-trans-butenal; propylene glycol; 2-propanol, 1-(2-propenyloxy)-; 1,3-dioxolane, 2-ethyl-4-methyl-; 1-propanol, 2'-oxybis-; and 1-

propanol, 2-(2-hydroxypropoxy)-. The primary products visible in the aqueous phase and the water phase, along with their respective area percentages are displayed in Table 2.2.

Table 2.2: The area percentages of the GC-MS chromatogram of the vapor, aqueous, and organic phases of the condenser in version 2.0

Organic Phase		Water Phase		Vapor Phase	
Product	Peak Area Percentage (%)	Product	Peak Area Percentage (%)	Product	Peak Area Percentage (%)
Propionaldehyde	14.64%	Propionaldehyde	16.43%	Carbon dioxide	4.45%
Acetone	2.72%	Acetone	2.99%	Propene	6.39%
Propanol	2.84%	Propanol	2.41%	Propionaldehyde	64.76%
Dioxolane-ethyl-methyl	35.19%	Acetol	3.74%	Acetone	3.27%
Dioxane-dimethyl	28.53%	Dioxolane-ethyl-methyl	13.03%	Dioxolane-ethyl-methyl	3.95%
Pentanedione-methyl	2.35%	Dioxane-dimethyl	22.04%	Dioxane-dimethyl	6.25%
Other Products	13.73%	Propylene glycol	3.97%	Other Products	10.93%
		Dipropylene glycol	27.81%		
		Other Products	7.58%		

The next step was quantifying the primary products using external calibration standards. However, given the area percentage of propionaldehyde within the vapor phase, it was decided to only calibrate for propionaldehyde for the time being. The calibration for propionaldehyde as well as the adjusted calibration curves are displayed in Figure 2.10.

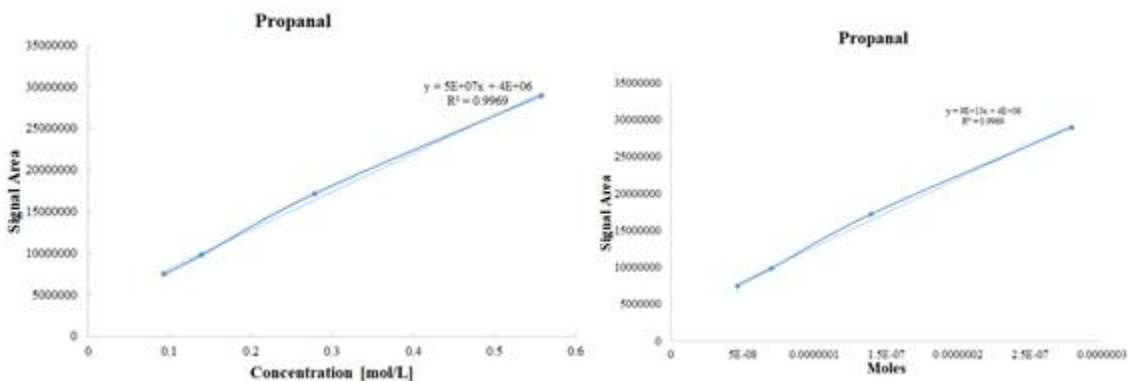


Figure 2.10: Propionaldehyde (propanal) calibration curve (left) and adjusted propanal calibration curve (right)

The propionaldehyde calibration curve displayed on the left was produced with the GC-MS using liquid, external calibration standards. These standards were made by

dissolving a known concentration of propionaldehyde in water to correlate said concentration to an area signal on the GC-MS. Using the external calibration curve on the left in Figure 2.10, one can the calibration curve on the right in Figure 2.10 by multiplying the concentration by the amount of volume injected into the GC-MS, which is about 500 nL. By doing this, one can create a calibration curve of moles vs. signal area, as shown in Figure 2.10. Then by taking the signal area of the vapor phase for propionaldehyde, one can plug it into the linear formula for the adjusted calibration to get moles of injected propionaldehyde from the gas. By taking this value and dividing it by the amount of injected volume from the syringe, 500 μ L, one will be left with a concentration. This concentration can then be multiplied by the total gas captured within the sampling bag. This is estimated to be around 2.4 L, as a nitrogen flow rate of 40 mL/min over the course of 60 minutes would produce 2.4L of gas. Thus, the total amount of moles of propionaldehyde within the vapor phase can be estimated through this methodology. This methodology was then used to calculate the number of grams of propionaldehyde within the vapor phase. A similar methodology was used for calculating the amount of propionaldehyde within the aqueous and organic phases as well. Additionally, it was assumed that the remaining gas and liquid products followed similar signals to that of propionaldehyde; thus, the calculated masses of the propionaldehyde in the condensate and vapor phase were divided by their respective area percentages. Essentially, the liquid and vapor phases were assumed to be 100% propionaldehyde and the difference between the vapor and liquid phase splits were examined. As it turned out from these calculations and assumptions, 17% of the total cracking products produced remained in the gas phase while 83% of the products remained in the organic and aqueous phase.

As previously discussed, the desired mass closure was about 95%. Although the mass balance closure of these combined phases was within in experimental error of 95%, it was desired to achieve a mass balance closure of over 95% in a single phase. That is, to completely close the mass balance without having to account for the vapor phase anymore. As such, version 3.0 of the reactor system was developed.

2.3.3 Reactor Setup Version 3.0 Product Analysis

As previously mentioned, the only goal that version 3.0 from version 2.0 was the closure of the mass balance of above 95% in the liquid phase. After the addition of the second condenser, a similar methodology, as described in version 2.0 product analysis was utilized for three samples of the same run parameters. These three repeated samples had mass balance closures of 96-98%, which was above the desired 95%. Additionally, propionaldehyde was pumped into the system and condensed at condenser. The total amount of propionaldehyde that was recovered was approximately 97% of what was pumped into the system. This result along with the calibration curve result, allowed for the dismissal of the vapor phase entirely. From now, the only quantification results would be from the liquid condensate. Additionally, it is worth noting propionaldehyde and propene were the primary remaining products that were left unaccounted for in the vapor phase.

With a mass balance closure of 96% liquid and 4% vapor, the condensate was reexamined. Several different solvents were tested in order to combine the aqueous and organic phases; however, many of these solvents had similar retention times as main products and/or were reactive with the products. Despite these setbacks, water was eventually used as the primary solvent for the products. The GC-MS method file for the liquid phase was the exact same setup described for the other liquid phases in version 2.0:

is usually the case with 1,4-dioxane, 2,5-dimethyl and 1,3-dioxolane, 2-ethyl-4-methyl. These different peaks are believed to be isomers of the same product; therefore, the signal areas of the peaks identified as the products are simply summed.

Given the good separation and peak shape shown in the chromatogram, the areas of the products can readily be calibrated for. The calibration curves for these seven products are displayed in Figure 2.12. However, 1,4-dioxane, 2,5-dimethyl; 1,3-dioxolane, 2-ethyl-4-methyl; and 2-ethyl-trans-2-butenal could not be directly purchased with ease; therefore, chemicals of similar structures were used in place of said products. For 1,4-dioxane, 2,5-dimethyl, 1,4-dioxane was calibrated for in its place. For 1,3-dioxolane, 2-ethyl-4-methyl, 1,3-dioxolane was calibrated for in its place. For 2-ethyl-trans-2-butenal, trans-2-methyl-2-butenal was calibrated for in its place. Using the discussed substitutes, it was assumed that the signal response for the product chemical and the substitute chemical were the same. Additionally, the calibration substitutes are displayed in Figure 2.12. The curves also display their respective linear trend equation, which is the basis of the quantification. The curves also display their respective R^2 values, which are all above 0.99. The number of points varies from curve to curve, but all the curves have at least four points, which are used to define the linear regression equation. It is also worth noting that all these curves display a linear fit, because all non-linear points were removed, which resulted from large concentrations.

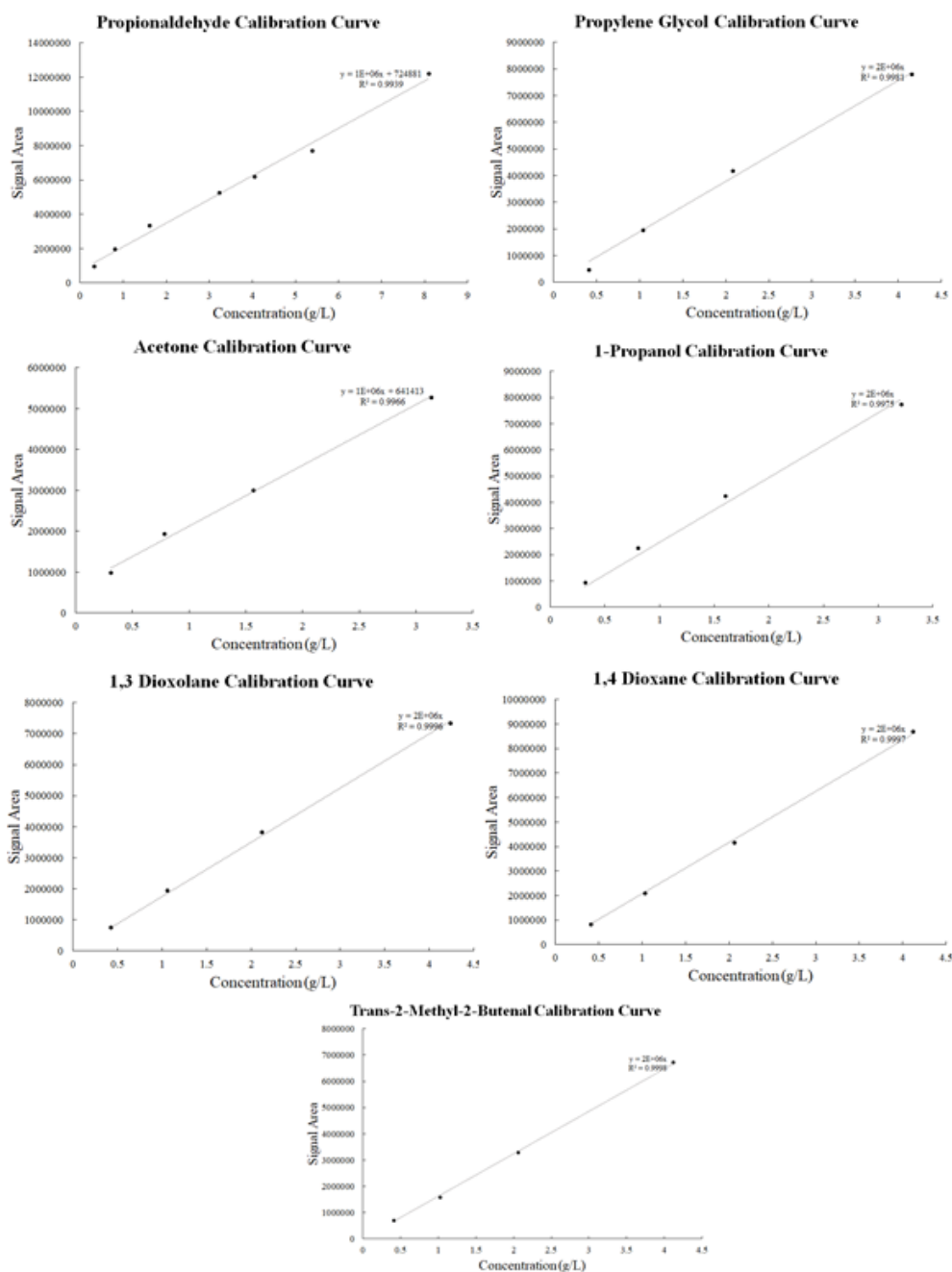


Figure 2.12: Calibration curves for the primary seven products

These calibration curves were then used to redefine selectivity of the products. Instead of using the area of percentages of the product compounds, one can adjust the areas percentages according to the calibration curves in Figure 2.12. This allows for an accurate representation of the selectivity of the seven products by adjusting their respective signals.

For example, propionaldehyde may give a much stronger signal reaction for a given concentration than acetone at the same given concentrations; thus, their signal areas are adjusted for and divided by the sum of the total product area to calculate selectivity. Thus, the resulting adjusted selectivity for the standard cracking run presented in Figure 2.11 are displayed in Table 2.3 for the primary seven products.

Table 2.3: The adjusted selectivity of the primary seven products in the standard reaction run

Product	NH ₄ -ZSM-5 (50:1) Selectivity
Propionaldehyde	26.91%
Acetone	2.47%
1-Propanol	4.36%
1,3-Dioxolane, 2-ethyl-4-methyl-	6.69%
1,4-Dioxane, 2,5-dimethyl-	34.01%
2-Ethyl-trans-2-butenal	6.27%
Propylene Glycol	5.22%
Other Products	14.07%

Additionally, these calibration curves can also be used to quantify the yield of the products. However, given the lack of injection volume precision, it is necessary to use an external standard to adjust for variations in injection volume. Several different external standards were tested, but most of them reacted with the products; however, butylene glycol was purchased and tested. It seemed to be stable with the reaction products and have a retention time of about 10 minutes, which is far away from the other product peaks. Therefore, it was decided that butylene glycol would act as the external standard for the product analysis. Thus, butylene glycol was calibrated for, and its calibration curve is

shown in Figure 2.13. Once again, the calibration curve yielded an R^2 of over 0.99, which is the result of a good linear fit. The linear regression equation is also displayed on the calibration in Figure 2.13. The calibration curve displays five points of varying concentrations. Although these points do not follow closely from one to the next, the linear regression is quite good, and this factor is overlooked.

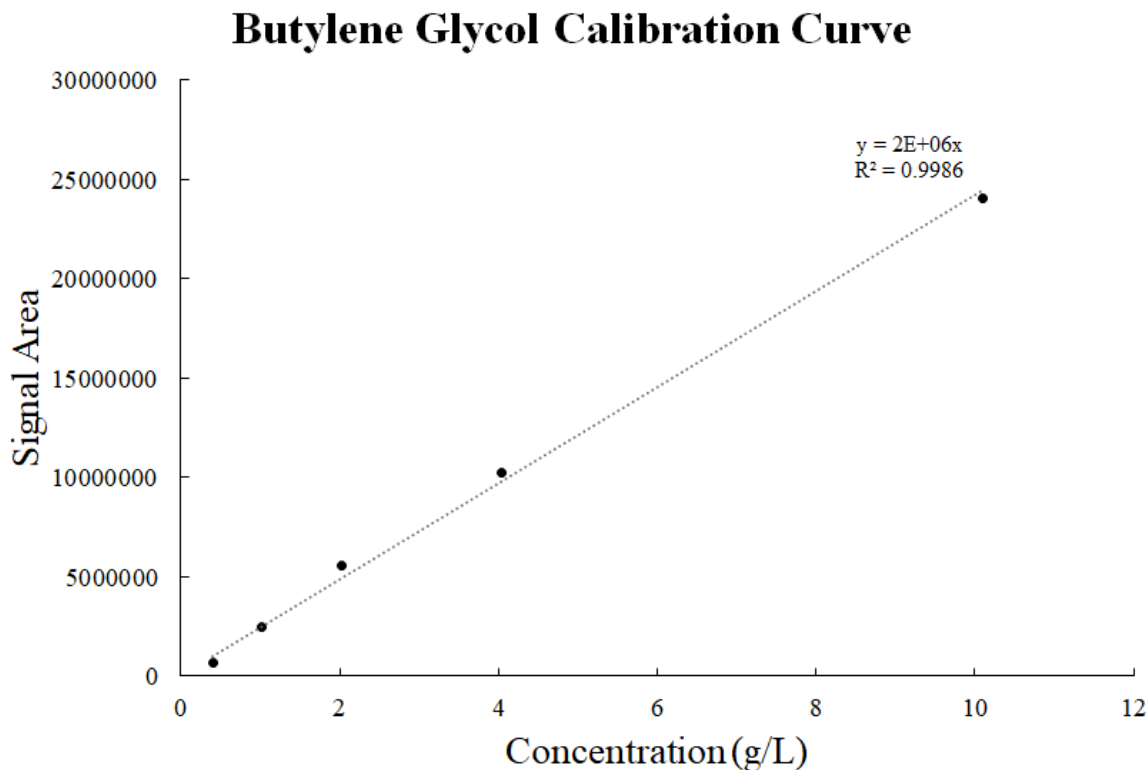


Figure 2.13: Calibration curve for the external standard

2.4 Catalyst Characterization Methods

There are several the useful techniques for characterizing coke buildup on/in catalysts. The primary characterization techniques to be discussed are thermogravimetric analysis (TGA), powder X-ray diffraction (PXRD), diffuse reflectance for infrared Fourier transform spectroscopy (DRIFTS), nitrogen physisorption positron, annihilation lifetime spectroscopy (PALS), and scanning electron microscopy (SEM). As previously mentioned,

coking is one of the primary concerns for catalytic cracking reaction⁷⁷. Coking, which is the buildup of carbonaceous materials on a catalyst surface, can greatly hinder the catalytic performance of a catalyst^{50,51,77,78}. As such, these characterization methods primarily focus on the characterization of potential coke buildup on/in the zeolite structure.

2.4.1 Thermogravimetric Analysis (TGA)

TGA was performed at the University of South Carolina (UofSC) on a Shimadzu 2010 Shimadzu TGA-50H with a TA-60WS thermal analysis, and GC-60A flow control unit, and BLW-50 cooling blower. The TGA was operated from room temperature to 600 °C for all the runs performed. The ramp rate was set to 10 °C/min for each run with typically a hold of 10 minutes at 600 °C. The gas flow, either air or argon, was flown from top to bottom at 200 mL/min. The platinum basket was supported by a quartz rod while being held with a platinum basket holder. Several runs of zeolites and polyols were conducted and will be further discussed in the experimental results section. Additionally, a baseline of sorts for the polyol of interest, polypropylene glycol, was performed using the TGA. Polypropylene glycol was added to the aluminum basket without any catalyst. The run then proceeded as normal while flowing air over the basket, as displayed in Figure 2.14.

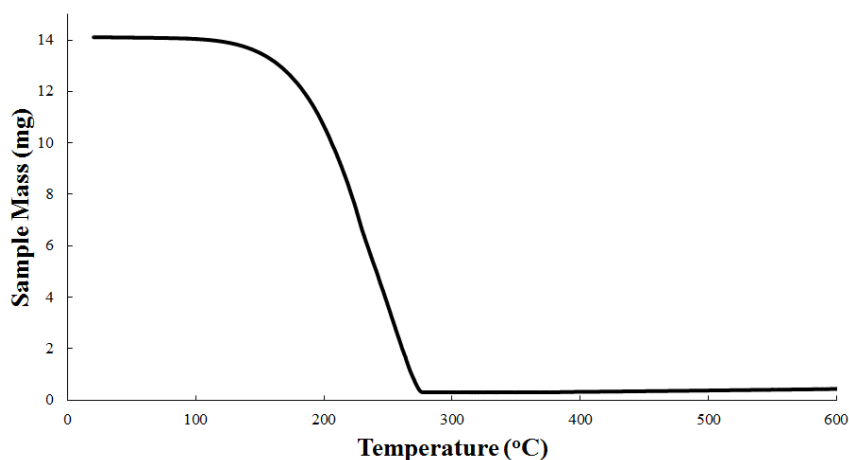


Figure 2.14: TGA of PPG

Based on Figure 2.14, the polyol began to decompose quite rapidly beginning at about 150 °C and ending at around 280 °C. Using this information, it can be estimated that mass loss between these temperature ranges may be attributed to excess polyol on the catalyst while any mass loss beyond 280 °C will likely only be from coke on/in the catalyst.

2.4.2 Power X-ray Diffraction (PXRD)

PXRD was performed at UofSC on a Rigaku MiniFlex II with Cu K α source radiation ($\alpha = 1.5406$) from a 2-Theta region of 3-80° at a scan rate of 2°/min. Samples were taken using a zero-background holder, and the results will be discussed in the experimental results section.

2.4.3 Diffuse Reflectance for Infrared Fourier Transform Spectroscopy (DRIFTS)

DRIFTS was performed at UofSC using a mercury cadmium telluride (MCT) detector. The instrument scanned from 1000-4000 wavenumber (cm⁻¹), which resulted in a total of 256 scans performed. The scans were taken at atmospheric temperature and pressure in the presence of atmospheric air, and the results will be discussed in the experimental results section.

2.4.4 Physisorption

Physisorption was conducted at UC Berkeley by Dr. Alex Katz's group. Brunauer–Emmett–Teller (BET) method, using nitrogen isotherms, was implemented to calculate sample surface areas and porous volumes.

2.4.5 Scanning Electron Microscopy (SEM)

SEM was conducted at UofSC in the Department of Chemistry on a Zeiss Gemini500 Thermal Field Emission Scanning Electron Microscope (FESEM). This microscope operates at high vacuum allowing for high resolution imaging as well as

Energy Dispersive Spectroscopy (EDS) capabilities. The instrument has many available detectors, but an In-lens detector was used for all samples by analyzing type II secondary electrons (SE2).

2.4.6 Positron Annihilation Lifetime Spectroscopy (PALS)

PALS was conducted at Idaho National Lab (INL) by Dr. Urban-Klaehn. The PALS system is shown in Figure 2.15. Positron Annihilation Spectroscopy (PAS) offers a non-destructive analysis (NDA) of materials in the micro-scale. PALS utilizes positrons (anti-electrons) from a radioactive “beta plus” source to penetrate the studied material, which are annihilated using electrons to create a positron-electron annihilation signal. The resulting signal gives insight into the overall structure of the material. The comprehensive overview of the PAS principle, technologies, and its applications are found in the *Principles and Applications of Positron and Postronium*⁷⁹. INL offers three different PAS technologies that are operated by a Techno-AP state of the art fast-frequency digital spectrometer⁸⁰:

1. Positron Annihilation Lifetime (PAL)
2. Coincidence Doppler Broadening (CDB)
3. Age Momentum Coincidence Spectroscopy (AMOC)



Figure 2.15: TechnoAP Digital Instrumentation for PALS along with the fast scintillator detectors and the sample source

PALS relies on two “fast timing” detectors to correlate the lifetime of a positron in the material with its structure. The lifetime signal, in range of 10^{-12} to 10^{-9} s, provides information about the nanostructure and morphology of examined materials, such as voids, vacancies, defects, and microporous structures and their respective concentrations. This technique is commonly used in a variety of surface, metal, metal-oxide studies⁷⁹. PALS is used for non-conductive materials with high nano- and micro-porosities and free volumes, such as polymers, silica-gels, and zeolites. In these materials, which are typically used in catalysis, positrons can localize in form of a positron-electron hydrogen-like atom, called a positronium (Ps). These positroniums live much longer than “free” or “trapped” positrons since their total electric charge is neutral; this allows for far more in-depth analysis at the size and fraction of these microporous structures.

The Na-22 positron source, with a 2.6-year half-life, is sealed within a thin Ti cover that is used as the positron emitter⁸¹. During the measurement process, the source is surrounded by two samples in “sandwich” arrangement. The Techno-AP system was upgraded in 2020 to add long range timing systems to the existing standard one. This is especially useful in polymers and other materials with high “free-volume”, where positrons can be created and survive for longer periods of time. The time range sensitivity, which is related to the trapping of positrons, is usually limited to about 10 ns in metals, as positrons within metals annihilate faster due to their electronic conductivity. While for high “free-volume” and low conductivity materials, the lifetime range is extended to a maximum of 140 ns.

A total of four samples were characterized using PALS. The first sample was fresh ZSM-5, which was to act as the reference point. The second sample was ZSM-5 that had

undergone a catalytic cracking reaction with polyurethane. The third sample was ZSM-5 that had undergone a catalytic cracking reaction with PPG. The Fourth and final sample was a 5x reacted ZSM-5 sample with PPG. Additionally, these catalysts had been reacted with 20% steam, a 2:1 catalyst to polyol ratio, and a reaction temperature of 260 °C. These experimentations were conducted on version 1.0 of the reactor system with a total flow rate of 25 mL/min and a total mixed catalyst and polyol mass of 1.5 g.

The analysis on pelletized ZSM-5 samples was carried out by use of LT software program in two different timing ranges. Figure 2.16 presents a picture of the pelletized ZSM-5 reacted with polyurethane sample (left) and the pelletized ZSM-5 reacted with polypropylene (right). The source/sample is oriented in a sandwich arrangement with two BaF (barium fluoride) fast timing detectors. These detectors, shown at the top right and left in Figure 2.16, are used for registering the beginning and the end of the gamma signals, which are converted to positron lifetimes and intensities in the examined material. The fresh ZSM-5 and ZSM -5 reacted with polyurethane pellets were robust and sufficiently thick to absorb all remaining positrons after one run. The ZSM -5 reacted with PPG pellets were very fragile and broke apart; thus, the pieces of the broken pellets were stack together to make sure that all positrons were absorbed in the sample material, as seen in Figure 2.16.

The analysis was carried out by use of the LT v9.2 Kansy software program⁸¹.

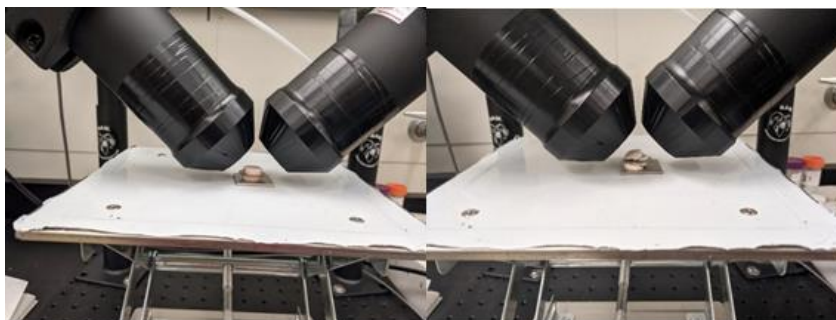


Figure 2.16: PAL measurements of ZSM-5 reacted with polyurethane pellets (left) and ZSM -5 with polypropylene glycol pellets (right)

2.5 Catalyst Synthesis Methodology

Several different zeolite catalysts were synthesized for the catalytic cracking reaction of PPG beyond the out of the box NH_4 -ZSM-5 catalyst. These catalysts include H-ZSM-5, mesoporous zeolite Y, Pt-H-ZSM-5, and 2D zeolite MFI nanosheets.

2.5.1 H-ZSM-5 Synthesis Methodology

Although all the ZSM-5 was purchased through outside vendors, it comes in the NH_4 form upon arrival. Thus, in order to convert the NH_4 -ZSM-5 to H-ZSM-5, the NH_4 -ZSM-5 zeolite had to be calcined. The idea is to thermally remove NH_3 from the zeolite, which would leave a single hydrogen atom to balance out the negative charge on an acidic site. There are several different procedures for calcining ZSM-5, but a variation of the procedure used by the Kronawitter group at UC Davis was utilized. The exact procedure involved the use of a shallow, horizontal bed under flow of zero-purity air with an isothermal hold at 120 °C for 1 hour, followed by an isothermal hold at 550-600 °C for 6 hours. This procedure also employed 2 °C/min ramp rates. However, due to a lack of viability, about 50 g of NH_4 -ZSM-5 was placed in a large crucible. This was placed in an oven and heated in the presence of atmospheric air. An isothermal hold at 120 °C for 1 hour, followed by an isothermal hold at 550-600 °C for 6 hours, and the implementation of 2 °C/min ramp rates were utilized as well. After the zeolite had cooled down, it was mixed with polyol and reacted following the previously described procedures.

2.5.2 Mesoporous Zeolite Synthesis Methodology

Mesoporous zeolite Y samples were synthesized by Dr. Katz's group at UC Berkeley. These samples were synthesized with 15 to 1 and 30 to 1 silica to alumina ratios. These mesoporous samples were synthesized closely following the procedure outlined by

L. Meng et al with slight alterations⁸². The nitrogen physisorption results for said mesoporous samples and their microporous counterparts are displayed in Figure 2.17.

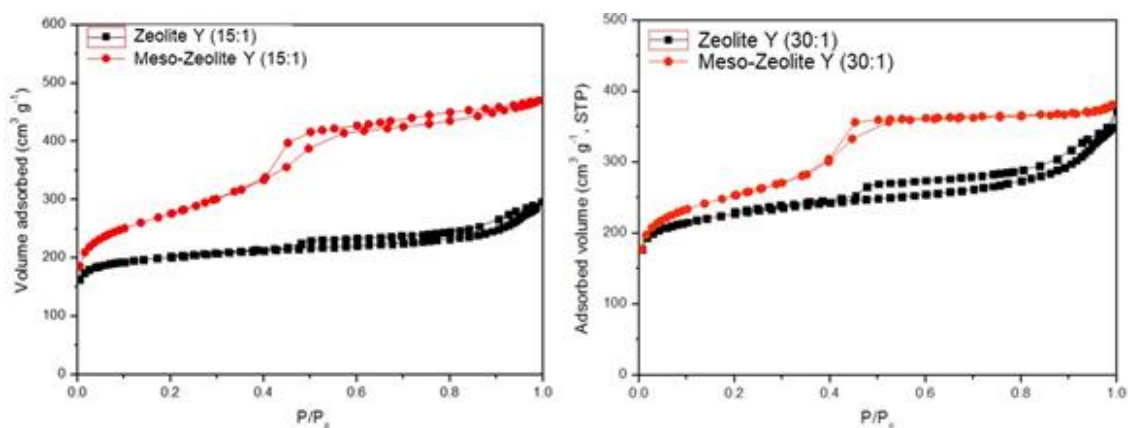


Figure 2.17: Nitrogen physisorption data for microporous and mesoporous zeolite Y samples

Based on Figure 2.17, there is a clear increase in the adsorbed volume of the mesoporous samples vs. the microporous samples. This is expected, as the overall volume capacity increases by increasing the average pore size of the zeolite. The trends shown in Figure 2.17 can more clearly be seen in Table 2.4.

Table 2.4: Nitrogen physisorption data for microporous and mesoporous zeolite Y samples

Sample	BET SA (m ² /g)	Micro SA (m ² /g)	Meso SA (m ² /g)	Micro PV (cm ³ /g)	Meso PV (cm ³ /g)
Y zeolite (15:1)	760	580	180	0.23	0.22
Meso-Y zeolite (15:1)	1001	413	588	0.17	0.56
Y zeolite (30:1)	847	579	268	0.23	0.33
Meso-Y zeolite (30:1)	930	472	458	0.19	0.59

2.5.3 Pt-H-ZSM-5 Synthesis Methodology

Pt-H-ZSM-5 was synthesized by Noah Felvey from the Kronawitter group at UC Davis. These samples involved the incorporation of Pt in the H-ZSM-5 framework via ion exchange. Overall, 8.0 g of Pt-H-ZSM-5 were synthesized at UC Davis and delivered prior to calcination. These samples contained a Pt weight loading of 0.4%, verified by inductively coupled plasma mass spectrometry (ICP-MS). Similar to H-ZSM-5, the zeolite is the Zeolyst CBV 5524G sample with a silica to alumina ratio of 50. The samples are first prepared by mixing H-ZSM-5 with $\text{Pt}(\text{NH}_3)_4(\text{NO}_3)_2$ precursor, which is followed by several cycles of centrifugation and washing. The sample is then dried at 80 °C in atmospheric air. The last remaining step involves the samples calcination.

The UC Davis calcination procedure for the Pt-H-ZSM-5 involves an in-situ calcination procedure. A flow of 20% O_2 is flown over the sample while it is heated from 25 °C to 120 °C at a temperature ramp of 5 °C/min. The sample is left to dwell at 120 °C for 1 hour, before then ramping to 700 °C at 2 °C/min, where it is left to dwell for an additional 2 hours. The sample is then cooled to 500 °C and the flow switched to N_2 , due to possible moisture within the zero-purity air cylinders. Once the sample is cooled, it is ready for experimental use. Because zeolite samples are inadvertently exposed to air prior to the catalytic cracking reaction, the procedure was slightly modified. The procedure for the Pt-H-ZSM-5 samples involved placing the uncalcined sample in a crucible and into an oven. The oven was then heated from 25 °C to 120 °C at a temperature ramp of 5 °C/min. The sample was left to dwell at 120 °C for 1 hour, before then ramping to 700 °C at 2 °C/min. The sample was then cooled and mixed with the polyol and introduced into the reactor system.

2.5.4 2-D MFI Zeolite Nanosheets Synthesis Methodology

2-D MFI Zeolites nanosheets were synthesized by Kanan Shikhaliyev at UofSC. The synthesis procedure utilized is based on the synthesis procedure described by R. Wei et al⁷⁰. Initially, the bi-functional surfactant, $C_{22}H_{45}-N^+(CH_3)_2-C_6H_{12}-N^+(CH_3)_2-C_6H_{13}(Br^-)_2(C_{22-6-6}Br_2)$, was synthesized by dissolving 0.2 mol of 1-bromodocosane and 2 mol of N,N,N',N'-teramethyl-1,6-diaminohexan in a 2000 mL, 1:1 mixture of acetonitrile and toluene. This mixture was then heated to and held at 343 K for 24 hours. After cooling to room temperature, the solid particulate was filtered out of the solution and washed with diethyl ether, and then dried in air at 333 K for 12 hours.

Once the substrate was synthesized, the 2-D MFI zeolites were synthesized via hydrothermal methodology. 0.005 mol of surfactant was dissolved in deionized water to form a 10 wt% template solution. 0.06 mol of NaOH along with 0.1 of TEOS was added to the template solution. The resulting solution was stirred at 333 K for 0.5 hours. An additional solution was prepared by dissolving Al_2O_3 and 0.015 mol of HCl acid in deionized water. This solution was then added drop-wise to the previous solution to form a colloidal solution. This colloidal solution was then stirred at 333 K for 6 hours before being transferred in a Teflon-coated stainless steel autoclave, which it was heated to 423 K and set to maintain said temperature for 120 hours; additionally, this reaction was carried out twice without stirring and once with. The solid product was then recovered and set to dry at 343 K for 14 hours. Once the product was fully dry, it was calcined in air at 823 K for 5 hours.

Three batches of 2-D MFI zeolites were synthesized. One synthesis procedure utilized stirring during the reaction while the other two were without stirring. Additionally, the silicon to aluminum ratio of the first non-stirred batch was 1 to 10 and the two additional

batches, consisting of stirred and non-stirred, are both 1 to 50. All three of these surfactants were characterized by PXRD in Figure 2.18.

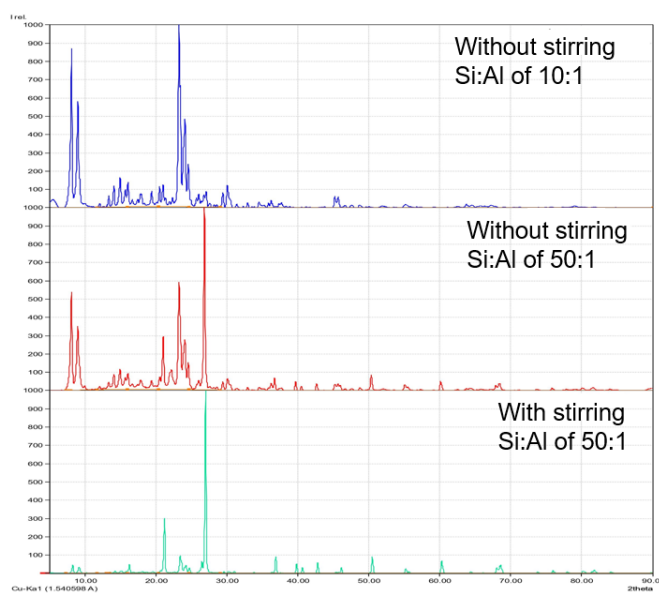


Figure 2.18: PXRD pattern of the synthesized MFI zeolite nanosheets

Based on Figure 2.18, the PXRD pattern for the 2-D MFI zeolites synthesized are all crystalline with a crystal structure very similar to that of ZSM-5 and the previously reported 2-D MFI zeolites, especially for the silicon to aluminum ratio of 1:10^{67,69}. However, slight differences can be seen in the higher silicon to aluminum ratio zeolites. The large increase in the peak at a 2-theta of around 27° is likely due to silica according to Match!. SEM images were also taken of the synthesized 2-D MFI zeolites, as shown in Figure 2.19.

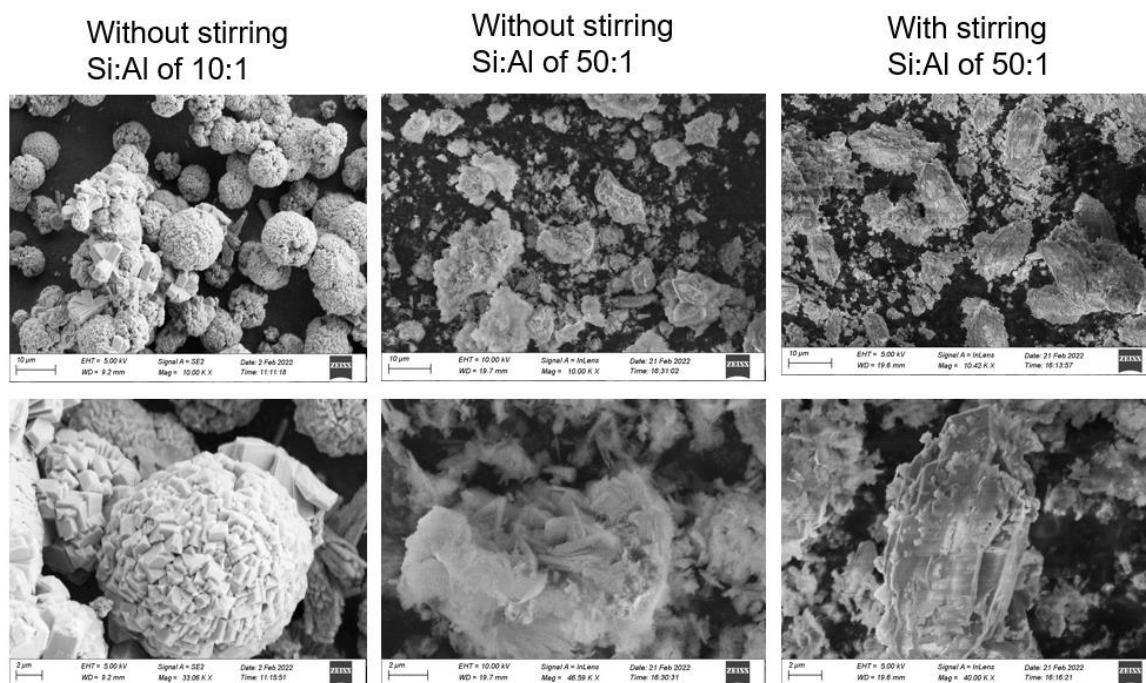


Figure 2.19: SEM images of synthesized 2-D MFI zeolites

The 2-D MFI zeolites with a silicon to aluminum ratio of 10:1, shown in Figure 2.19, seem fairly similar to the MFI zeolites discussed in Figure 1.18. From a distance, both zeolites display ball-like structures. However, upon closer examination of the synthesized zeolite in Figure 2.19, the ball-like structures are not floral like the structures in Figure 1.18. In fact, there are no visible sheets, and there appears to be large crystal-like structures also intermingled within the ball-like structures. These crystal-like structures bare a similar resemblance to ZSM-5³². It may be possible that an intermediate zeolite structure, between nanosheets and ZSM-5, was formed, as presented in Figure 1.15. Additionally, both 50:1 synthesized MFI sheets seem to resemble large crystals that have thin sheets peeling from their structure; although these sheets may resemble MFI sheets, their uniformity from structure to structure is lacking.

2.6 Reaction Conversion and Selectivity Methodology via Liquid Chromatography-Mass Spectrometer

To quantify the amount of unreacted polyol within condensate, the condensate was taken to the liquid chromatography-mass spectrometer (LC-MS) in the Department of Chemistry at UofSC. The idea was to produce a calibration curve to quantify the amount of unreacted polyol within the condensate, which would allow for the quantification of reactant conversion. However, upon initial sampling of PPG standards, as shown in Figure 2.20, it became clear that PPG was far more of a number average than originally anticipated.

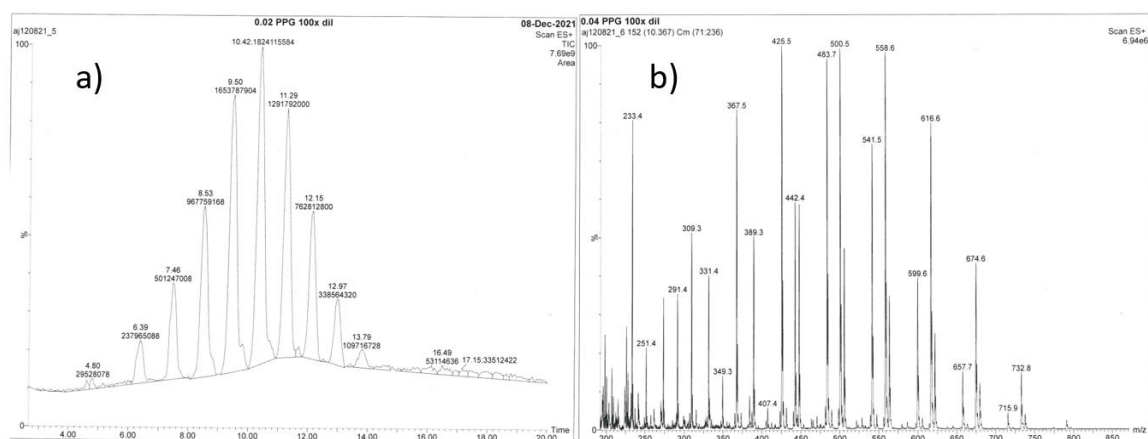


Figure 2.20: LCMS data for PPG a) the m/z from the mass spectrometer b) the LC-MS chromatogram

As seen in Figure 2.21 b, there are numerous peaks, which correspond to all different length propylene glycol chains. Additionally, Figure 2.21 a shows three separate m/z ratios for a single peak. This is due to the affinity for sodium and ammonium on the PPG chain. Given the wide range distribution of these chain lengths, di-propylene glycol could no longer be considered a product of the cracking reaction; in fact, the di-propylene glycol peaks observed in the GC-MS may have simply resulted from the reactant polyol. Therefore, it was decided that selectivity would simply be redefined to only incorporate the seven primary products of interest. Much like before, the areas of these seven products

were adjusted accordingly and their concentrations calculated. These concentrations were summed, and the selectivity was defined as the concentration of a single product over the total concentration. This methodology was applied to all sections following Section 3.6 of the Experimental Results and Discussion section.

After the initial PPG standard run in Figure 2.20, additional PPG Mn ~425 standards were synthesized and run using the LC-MS. These runs also displayed numerous peaks, whose peak areas were summed. Much like the previous calibration curves, a linear fit was produced using the calibration standards and their resulting summed, peak areas correlated to form the calibration curve shown in Figure 2.21.

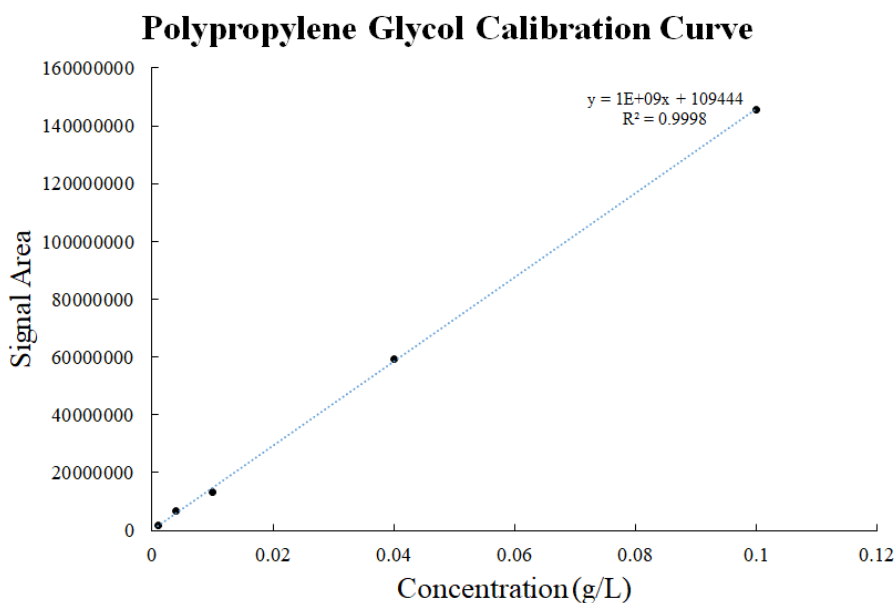


Figure 2.21: LC-MS calibration curve for PPG Mn ~425

Using this calibration curve, the concentration of PPG in the reactor condensate can be calculated. The concentration of PPG after the reaction can then be compared to the theoretical starting concentration of PPG prior to the reaction. This would allow one to quantitatively compute the conversion of PPG within the reaction. However, due to potentially large losses of unreacted PPG from the reactor bed to the condenser, the overall

conversions were extremely high. Therefore, a relative conversion comparison between samples can be calculated through peak area. A similar method can also be employed on the product concentrations of products in the GC-MS. A comparison between the total product peak areas for the seven products can be used to an overall conversion between the two samples.

2.7 General Economic Evaluation

As previously discussed, the catalytic cracking reaction of PPG resulted in seven primary products: propionaldehyde; 1,4-dioxane, 2,5-dimethyl; 1-propanol; 1,3-dioxolane, 2-ethyl-4-methyl; acetone; 2-ethyl-trans-2-butenal; and propylene glycol. The overall goal of this project is polyol upcycling; however, for such a process to be implemented on an industrial scale, its profitability will likely be a significant factor alongside its environmental benefits. Despite the eventual usage of waste polyols and polyurethanes, the operating costs of said process will be the difference between profitability or not. That is to say that although the eventual starting material will essentially be free, the required system units will dictate its economic viability. Therefore, a minimization of operation units, namely separation units, will likely benefit said process from an economic perspective. As such, the primary goal for the experimental work was primarily focused on improving the selectivity towards as few of products as possible. Thus, an economic evaluation of the products is necessary. Table 2.5 displays the 2019 global market value and the 2016 price per metric ton for the seven chemical products of interest⁸³⁻⁸⁶. The chemical price was estimated using the average price per kg of imported chemical found on Zaubia. The price was converted to USD from INR at a rate of 74.72 INR per USD. It should be noted that the price of chemicals can dramatically change from year to year;

therefore, this economic evaluation is to serve as a general estimate for discussion purposes.

Table 2.5: The 2019 global market value and 2016 chemical price of the seven primary products^{83–86}

Chemical Product	2019 Global Market Value (Billion USD)	2016 Price (USD/MT)
Propionaldehyde	1.4	~ 870
Acetone	4.59	~ 540
1-Propanol	2.63	~ 860
1,3-Dioxolane, 2-ethyl-4-methyl-	N/A	N/A
1,4-Dioxane, 2,5-dimethyl-	N/A	N/A
2-Ethyl-trans-2-butenal	N/A	N/A
Propylene Glycol	3.8	~ 1000

Based on Table 2.5, only four out of the seven products have a general market, 1,4-dioxane, 2,5-dimethyl; 1,3-dioxolane, 2-ethyl-4-methyl; and 2-ethyl-trans-2-butenal have no sizeable market. In fact, these three products have almost no use; therefore, further investigation into improving their selectivity would be meaningless. However, Table 2.5 indicates the potential economic feasibility for propionaldehyde, acetone, 1-propanol, and propylene glycol. These four chemicals all have market values above a billion USD. Acetone may have the largest market value compared to the other four products of interest, but it is a relatively cheap solvent with a 2016 price that is significantly lower than the other three products. 1-propanol and propionaldehyde have very similar chemical values while propylene glycol presents a slightly higher chemical value and global market value. Thus, propionaldehyde, 1-propanol, and propylene glycol may provide the economic

feasibility required for this reaction on an industrial scale. Upon initial testing with ZSM-5 catalysts, as seen in Table 2.3, the selectivity for 1-propanol and propylene glycol was low very compared to the selectivity of propionaldehyde. In fact, the primary products of interest, regarding their high selectivity, were 1,3-dioxolane, 2-ethyl-4-methyl and propionaldehyde. However, 1,3-dioxolane, 2-ethyl-4-methyl did not present any substantial market value, as previously discussed. Therefore, it was decided that propionaldehyde may provide the best economic feasibility given its relatively high market and chemical value. Thus, the primary objective for this project sought to increase the selectivity and yield of propionaldehyde within this reaction.

Since propionaldehyde is the primary focus of this reaction, it is important to understand its uses and alternative synthesis routes. Propionaldehyde is produced through hydroformylation, which is also known as the oxo process, like most aldehydes⁸⁷. This homogeneous reaction typically occurs at moderate pressures (1.8-6 MPa) and at low temperatures (85-130 °C) in the presence of a Rhodium based catalyst⁸⁷⁻⁸⁹. The reaction is typically limited by the product separation and the regioselectivity of linear and branched aldehydes⁸⁹⁻⁹⁴. Thus, the potential implementation of a heterogeneous reaction, such as the reaction of interest, may be significantly environmentally and economically favorable. Regardless, propionaldehyde is used in a wide range of products like fertilizers, chemicals used in rubber synthesis, and cellulose⁸⁴. Additionally, the market for propionaldehyde is expected to experience significant growth in the upcoming years due to its growing demand in the pharmaceutical and cosmetic industries. The global propionaldehyde market value is expected to grow from 1.4 billion USD in 2019 to 2 billion USD according to a growth report forecast, as displayed in Figure 2.22⁸⁴.

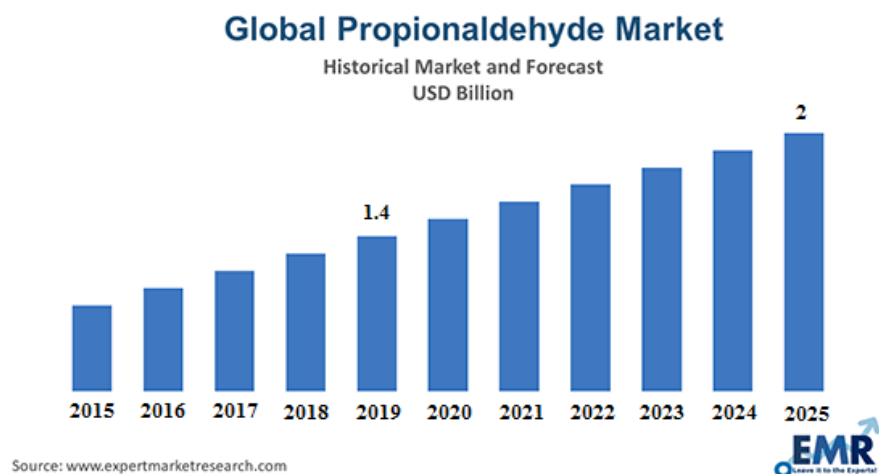


Figure 2.22: The yearly, global market value forecast for propionaldehyde⁸⁴

CHAPTER 3

EXPERIMENTAL RESULTS AND DISCUSSION

3.1 Design of Experiment (DOE) Using Reactor Setup Version 1.0

During the testing of version 1.0 of the reactor system, it was decided that the best way to gauge the impact of various parameters and improve the selectivity was to conduct a DOE. In short, a DOE is a statistical analysis method that allows for the quantification of parameter impact on an objective parameter as well as parameter significance within the model. A DOE not only allows for investigation into parameter impact, but it does so in an efficient manner, as opposed to an Edisonian approach. Thus, preliminary data regarding the parameters of interest is required. The patent examined several different parameters including the catalyst, the catalyst and polyol mixing, the steam percentage in the carrier gas, and the reaction temperature while keeping the catalyst to polyol ratio at a constant 10 to 1²⁸. It was decided that the steam percentage in the carrier gas, the temperature, and the reaction temperature were the most interesting parameters to experiment with. The reaction temperature was shown to drastically affect the product distribution in the patent; therefore, it was a key parameter to investigate. The catalyst to polyol ratio within the patent was unrealistically high; therefore, a potential optimization of said ratio was of high interest. Lastly, steam has been shown to inhibit secondary reaction that may potentially lead to coking⁴⁰⁻⁴²; therefore, steam was an important parameter to investigate its effect on the product distribution. Additionally, as previously stated, it is important to understand that selectivity here refers to the adjusted quantification of products seen in the GC system.

Using the calibration curves in the version 1.0 methodology section, a percentage of product gas was defined as propionaldehyde, and the remaining percentage defined as other products. Therefore, the selectivity of propionaldehyde refers to the amount of propionaldehyde with respect to the other observed product peaks.

Preliminary testing of the catalytic cracking of PPG and NH₄-ZSM-5 was conducted in version 1.0 of the reactor system. The resulting parameter scope results, prior to the DOE, are displayed in Figure 3.1. The goal of the preliminary parameter variation was to improve the selectivity of various products, namely propionaldehyde. When the reaction temperature was varied, the catalyst to polyol ratio was kept at a constant 2:1 and the steam percentage was kept at a constant 20%. While varying the catalyst to polyol ratio, the reaction temperature was kept at a constant 250 °C and a steam percentage of 20%. While varying the steam percentage in the carrier gas, the reaction temperature was kept at a constant 250 °C and a constant catalyst to polyol ratio of 2:1.

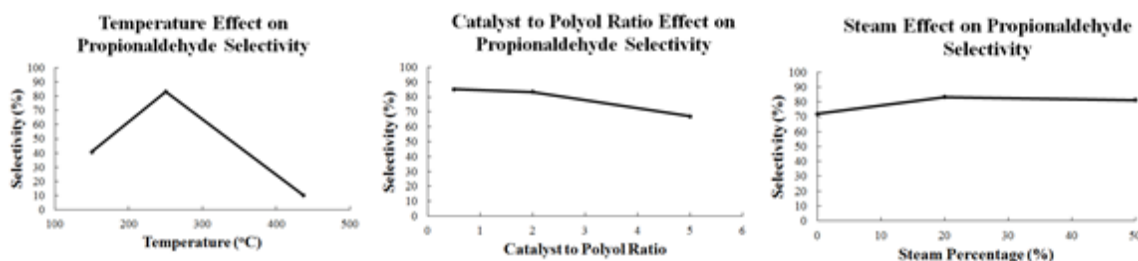


Figure 3.1: The preliminary testing of reaction temperature, the catalyst to polyol ratio, and the steam percentage in the carrier gas on the selectivity of propionaldehyde

Based on Figure 3.1, the reaction temperature had drastic effects on the selectivity of propionaldehyde. There appears to be a maximum value around 250 °C with sharp drop-off for selectivity at lower and higher temperatures. The catalyst to polyol ratio data seemed to indicate that a lower catalyst to polyol ratio would result in increased selectivity for propionaldehyde. The preliminary data for the steam percentage in the carrier gas did not

seem to indicate a strong trend for increasing propionaldehyde selectivity. However, it seemed as though steam might benefit the selectivity of propionaldehyde.

Based on the preliminary results, a DOE was setup using Minitab to investigate how temperature, steam percentage in the carrier gas, and catalyst to polyol ratio affected the overall selectivity of propionaldehyde. Given the time constraints of the various runs and the resulting conclusions to be drawn, a Box-Behnken response surface analysis was chosen as the type of DOE. This type of DOE not only allowed for the development of non-linear relationships, but it also allowed for co-factor interaction conclusions to be drawn from the results of the DOE. In total, 15 separate reactions were run and collected in gas sampling bags. The temperature was varied from 225, 250, and 275 °C; the steam percentage in the carrier feed was varied from 30, 50, and 70%; and the catalyst to polyol ratio varied from 1:3, 2:3, and 1:1. The total amount of catalyst and polyol injected for each run was 1.5 g. It should also be noted that the flow rate of carrier was not kept constant and ranged from 20-30 mL/min. The overall objective of the DOE was to optimize the reaction conditions by maximizing the overall selectivity of propionaldehyde within the vapor phase product. Additionally, the midpoint of the run was repeated three times for experimental error. The standard error for selectivity was determined to be 0.49% using the equation: $SE = \frac{\sigma}{\sqrt{n}}$, where SE represents the standard error, σ represents the standard deviation, and n represents the population size (three). The run parameters and results for each individual experiment are displayed in Table 3.1.

Table 3.1: The experimental parameters used for the DOE runs and their resulting propionaldehyde selectivity

Run	Temperature (°C)	Catalyst to Polyol Ratio	Steam in the Carrier Gas (%)	Propionaldehyde Selectivity (%)
1	225	0.33	50	82.9
2	275	0.33	50	88.6
3	225	1.00	50	81.1
4	275	1.00	50	88.9
5	225	0.67	30	85.2
6	275	0.67	30	88.2
7	225	0.67	70	91.9
8	275	0.67	70	91.1
9	250	0.33	30	88.0
10	250	1.00	30	86.4
11	250	0.33	70	84.2
12	250	1.00	70	89.8
13	250	0.67	50	91.5
14	250	0.67	50	90.4
15	250	0.67	50	89.8

Figure 3.2 also displays a visual representation of the data points conducted during the DOE. There are a total of 13 points, which represent the 13 unique data points collected, as the middle point was repeated three times.

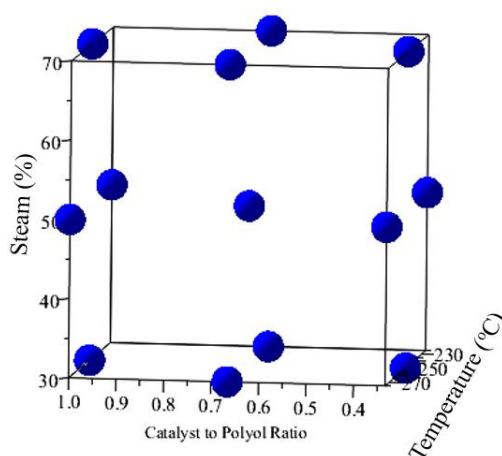


Figure 3.2: Visual representation of the DOE experimental points

To understand the meaning behind the DOE results, it is important to first examine the model's Pareto Chart displayed in Figure 3.3. The Pareto Chart puts the factors and their co-factor interactions into perspective by identifying the most statistically significant term within the model equation. The standardized effect is an arbitrarily calculated value based on the statistical significance of a parameter. In other words, the higher a parameter's standardized effect, the more significant said parameter is to the model equation.

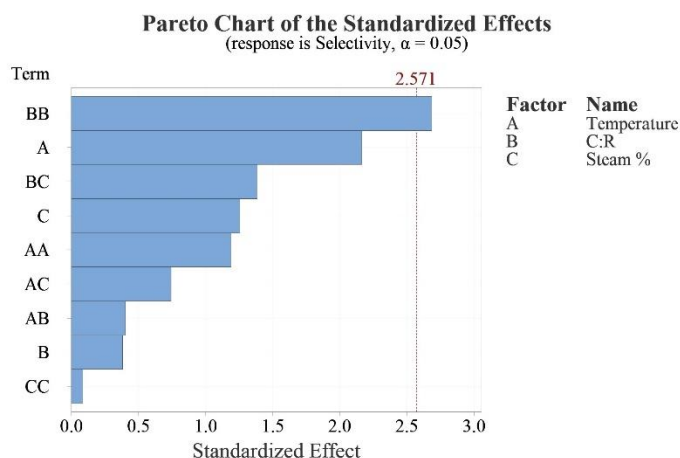


Figure 3.3: Pareto Chart for DOE results

Based on Figure 3.3, a p value, which is used to calculate the standardized effect, of 5% was chosen. This threshold is represented by the red dotted line at 2.571 in Figure 3.3. Thus, the catalyst to polyol ratio (C:R) squared was the only parameter that was deemed to be statistically significant within the model. However, temperature comes close, making it a significant term within the model as well. The other seven parameters fall drastically short of statistical significance within the model equation. Thus, it is important to keep the Pareto Chart in mind while drawing conclusions from the other DOE results.

The main effects plot, shown in Figure 3.4, represents the DOE model on a one-dimensional scale. Figure 3.4 displays the effect of each parameter on the selectivity of propionaldehyde.

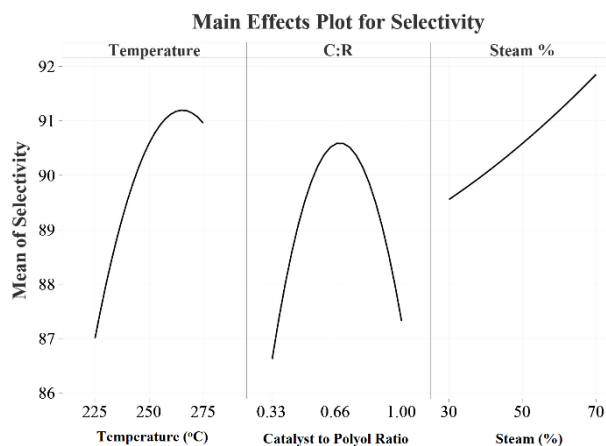


Figure 3.4: The main effects plot for the DOE

Temperature is shown to have a parabolic relationship with selectivity of propionaldehyde, resulting in a selectivity maximum at 265 °C. The catalyst to polyol ratio also demonstrates a parabolic relationship with selectivity, resulting in a selectivity maximum at the midpoint catalyst to polyol ratio, 0.66 or 2:3. The steam percentage is shown to have an almost linear relationship with selectivity, where the maximum lies at the high end of steam percent, 70%. Thus, from the Main Effects Plot, it can be concluded that the optimal temperature for this reaction lies at 265 °C, the optimal catalyst to polyol ratio lies at 2:3, and the greater the steam used in the carrier gas, the greater the selectivity. However, as previously mentioned, these relationships need to be taken into perspective with the Pareto Chart, Figure 3.3. Therefore, although steam demonstrated an increase in selectivity, the term is statistically insignificant within the model equation. Catalyst to polyol ratio is also insignificant by itself; however, the catalyst to polyol ratio term squared is the most significant term within the model. The parabolic relationship displayed by temperature is also of keen interest due to its significance within the model equation.

The contour plots, shown in Figure 3.5, represent the DOE model on a two-dimensional scale. Much like the Main Effects Plot, they display the optimal parameter conditions, except in two-dimensional regions.

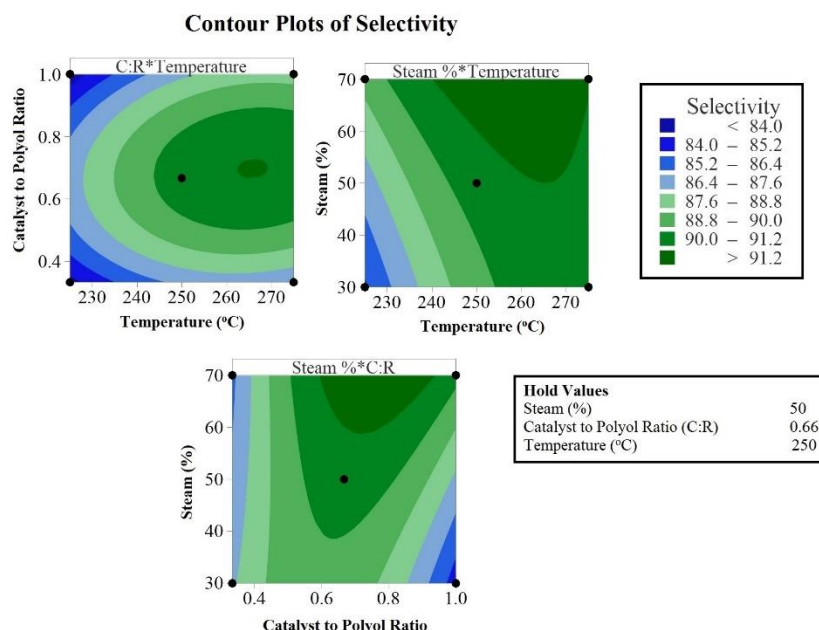


Figure 3.5: The Contour Plots for the DOE

The temperature vs. catalyst to polyol ratio contour plot displays a regional maximum at around 265 °C and 2:3, respectively. The temperature vs. steam percentage contour plot shows a regional maximum at 240-275 °C and 50-70%, respectively. The catalyst to polyol ratio vs. steam percentage contour plots displays a regional maximum from 0.6-0.9 and 60-70%, respectively. Similarly, to what was concluded from the Main Effects plots, there exist optimal reaction conditions for increasing the selectivity of propionaldehyde from the model equation. However, these optimal conditions are represented as regions rather than a global maximum.

The surface plot shown in Figure 3.6, represents the DOE model on a three-dimensional scale. Once again, there is a maximum selectivity displayed in the surface plot, but this point represents the absolute maximum interaction for temperature vs. the catalyst

to polyol ratio. The DOE produces three surface plots, but the most important is displayed in Figure 3.6, as temperature and the catalyst to polyol ratio squared terms are the only significant terms within the model.

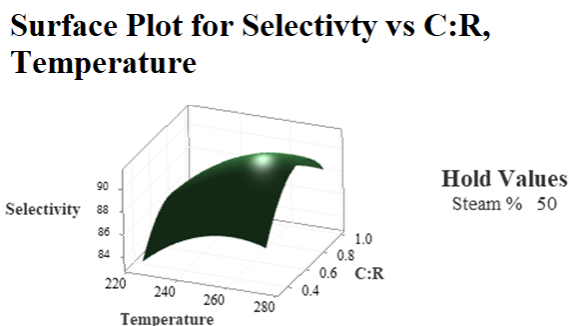


Figure 3.6: The Surface Plot for the catalyst to polyol ratio vs. temperature vs. propionaldehyde selectivity

In conclusion, the DOE has found the optimal reactions for the selectivity of propionaldehyde to be at a temperature of 265 °C, a catalyst to polyol of 0.66 or 2:3, and that the selectivity increases along with an increase in steam percentage within the carrier gas. Additionally, it is important to note that temperature and the catalyst to polyol ratio squared were deemed to be the only significant terms within the model equation.

Overall, the DOE was successful in optimizing the selectivity of propionaldehyde in the product gas. The optimal conditions that were found were significantly milder than those reported in the patent. The maximum propionaldehyde selectivity reported in the patent of 81.6% was achieved at a temperature of around 450 °C with a catalyst to polyol ratio of 10:1²⁸. A reduction from 10:1 to 2:3 is also an exceptional improvement as well. Despite the patent having minimal investigation of steam as a parameter, there was evidence within the patent that suggested steam may improve the overall selectivity of propionaldehyde²⁸. This was also proven within the DOE, as an increase in steam led to an increase of the selectivity of propionaldehyde.

Although this DOE presented similar results as displayed in the patent, the mass balance was still not closed. As such, these results were not taken as conclusive results. In fact, these results did not add up with the DOE that was later conducted using version 3.0 of the reactor setup, as will be discussed in the following subsection.

3.2 Design of Experiment (DOE) Using Reactor Setup Version 3.0

As previously discussed, the DOE from version 1.0 of the reactor setup did not result in conclusive results, given the lack of closure on the mass balance. However, the DOE was redone using version 3.0 of the reactor setup and product analysis methodology. The DOE, almost an exact replica of the first one previously described, sought to improve the product selectivity of propionaldehyde by varying reaction temperature, steam percentage in the carrier gas, and the catalyst to polyol ratio. However, the GC-MS and the product analysis methodology for version 3.0, which utilized seven calibration curves, was used to quantify the selectivity of propionaldehyde. The peak areas were adjusted using said calibration curves and the selectivity of propionaldehyde was defined as the adjusted peak area by the total peak area, including the peak area of other products.

Once again, preliminary data regarding steam percentage in the carrier gas, catalyst to polyol ratio, and the reaction temperature were required to define the DOE space of interest. PPG and NH₄-ZSM-5 were used in this DOE as well. The resulting parameter scope results, prior to the DOE, are displayed in Figure 3.7. Once again, when the reaction temperature was varied, the catalyst to polyol ratio was kept at a constant 2:1 and the steam percentage was kept at a constant 20%. While varying the catalyst to polyol ratio, the reaction temperature was kept at a constant 310 °C and a steam percentage of 20%. While

varying the steam percentage in the carrier gas, the reaction temperature was kept at a constant 310 °C and a constant catalyst to polyol ratio of 2:1.

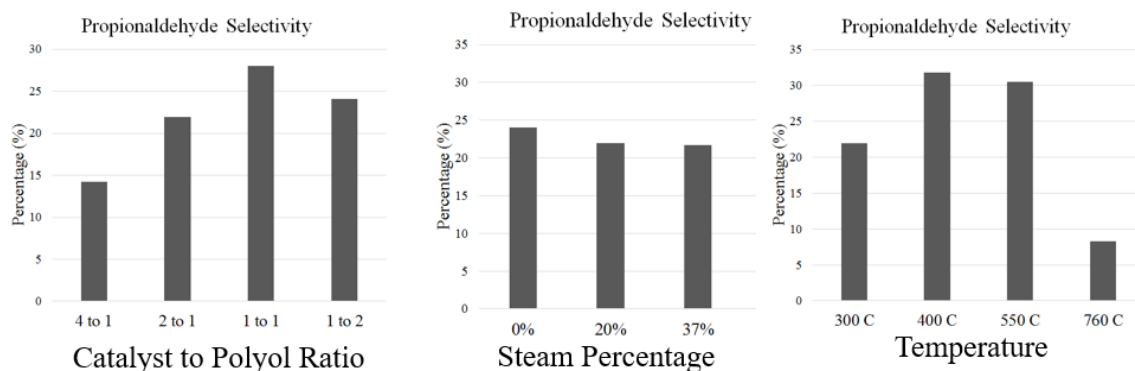


Figure 3.7: Preliminary results for the reactor setup version 3.0 DOE

Based on Figure 3.7, the reaction temperature had drastic effects on the selectivity of propionaldehyde. There appears to be a maximum value between 400 and 550 °C with sharp drop off for selectivity at the higher temperatures. The catalyst to polyol ratio also indicated a local maximum at around a 1:1 ratio for the selectivity for propionaldehyde. The preliminary data for the steam percentage in the carrier gas did not seem to indicate a strong trend for increasing propionaldehyde selectivity.

Based on the preliminary results, a DOE was setup using Minitab to investigate how temperature, steam percentage in the carrier gas, and catalyst to polyol ratio affected the overall selectivity of propionaldehyde. Given the time constraints of the various runs and the resulting conclusions to be drawn, a Box-Behnken response surface analysis was chosen as the type of DOE. This type of DOE not only allowed for the development of non-linear relationships, but it also allowed for co-factor interaction conclusions to be drawn from the results of the DOE. In total, 15 separate reactions were run and collected and analyzed via GC-MS. The temperature was varied from 300, 400, and 500 °C; the steam percentage in the carrier feed was varied from 0, 20, and 40%; and the catalyst to

polyol ratio was varied from 1:2, 1:1, and 1.5:1. The total amount mixed catalyst and polyol employed per run was 5 g, and the total flow through the system was kept constant at 100 mL/min. The overall objective of the DOE was to optimize the reaction conditions by maximizing the overall selectivity of propionaldehyde within the liquid phase product. Additionally, the midpoint of the run was repeated three times for experimental error. The standard error for selectivity was determined to be 0.28% using the equation: $SE = \frac{\sigma}{\sqrt{n}}$, where SE represents the standard error, σ represents the standard deviation, and n represents the population size (three). The run parameters and results for each individual experiment are displayed in Table 3.2.

Table 3.2: Individual run parameters and propionaldehyde selectivity for the DOE of reactor version 3.0

Run	Temperature (°C)	Catalyst to Polyol Ratio	Steam in the Carrier Gas (%)	Propionaldehyde Selectivity (%)
1	500	1.0	40	22.74
2	500	0.5	20	26.98
3	300	1.0	40	18.37
4	400	1.5	0	24.86
5	400	0.5	40	26.26
6	500	1.0	0	30.95
7	400	1.0	20	26.44
8	300	0.5	20	21.16
9	500	1.5	20	24.54
10	400	1.0	20	25.8
11	300	1.0	0	17.03
12	400	1.5	40	29.13
13	400	1.0	20	25.48
14	400	0.5	0	29.08
15	300	1.5	20	21.57

Figure 3.8 also displays a visual representation of the data points conducted during the DOE. There are a total of 13 points, which represent the 13 unique data points collected, as the middle point was repeated three times.

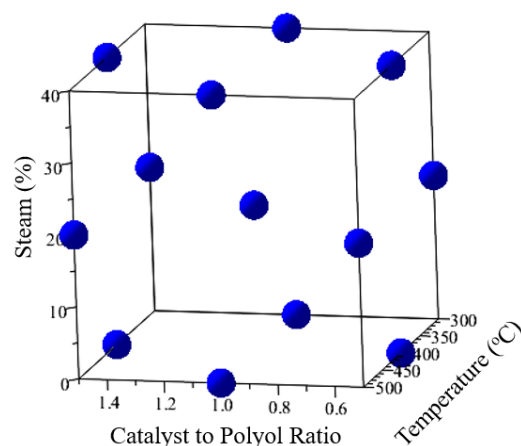


Figure 3.8: The design space for the DOE conducted on version 3.0 of the reactor system

Once again, to understand the meaning behind the DOE results, it is important to first examine the model's Pareto Chart displayed in Figure 3.9. The Pareto Chart puts the factors and their co-factor interactions into perspective by identifying the most statistically significant term within the model equation. The standardized effect is an arbitrarily calculated value based on the statistical significance of a parameter.

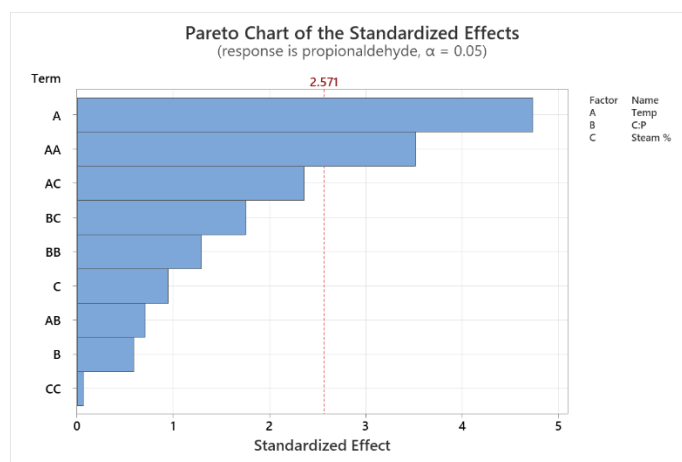


Figure 3.9: The Pareto chart for the DOE conducted on version 3.0 of the reactor system

Based on Figure 3.9, a p value, which is used to calculate the standardized effect, of 5% was chosen. This threshold is represented by the red dotted line at 2.571 in Figure 3.9. Thus, the temperature and the temperature squared were the only parameters deemed

to be statistically significant within the model. The other seven parameters fall short of the statistical significance threshold within the model equation. Thus, it is important to keep the Pareto Chart in mind while drawing conclusions from the other DOE results.

The main effects plot, shown in Figure 3.10, represents the DOE model on a one-dimensional scale. Figure 3.10 displays the effect of each parameter on the selectivity of propionaldehyde.

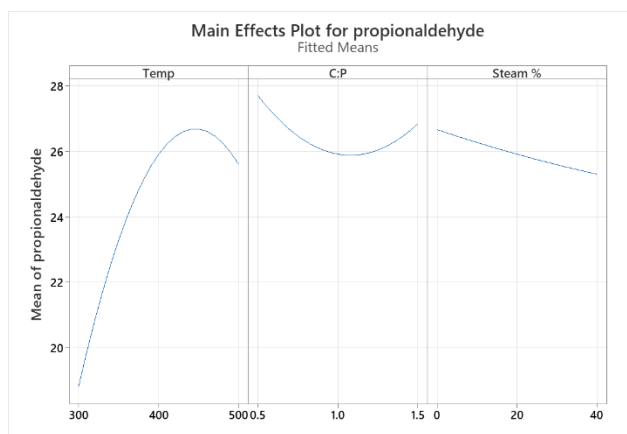


Figure 3.10: The main effects plot for the DOE in version 3.0 of the reactor setup

Temperature is shown to have a parabolic relationship with selectivity of propionaldehyde, resulting in a selectivity maximum at 440 °C. The catalyst to polyol ratio also demonstrates a parabolic relationship with selectivity, resulting in a selectivity minimum at the midpoint catalyst to polyol ratio 1:1 or 1. The steam percentage is shown to have an almost linear relationship with selectivity, where the maximum lies on the low end of steam percent, 0%. Thus, from the Main Effects Plot, it can be concluded that the optimal temperature for this reaction lies at 440 °C while the catalyst to polyol ratio maximum and steam percentage seem to indicate a slight variation in propionaldehyde selectivity, based on the y-axis of the main effects plot. However, these relationships need to be taken into perspective with the Pareto Chart, Figure 3.10. Therefore, although the

steam percentage and the catalyst to polyol ratio exhibited an arguable maximum, their significance within the model is quite low. Therefore, no information can be extracted from these variables regarding the selectivity of propionaldehyde. While the parabolic relationship displayed by temperature is of keen interest due to its significance within the model equation.

The contour plots, shown in Figure 3.11, represent the DOE model on a two-dimensional scale. Much like the Main Effects Plot, they display the optimal parameter conditions, except in two-dimensional regions.

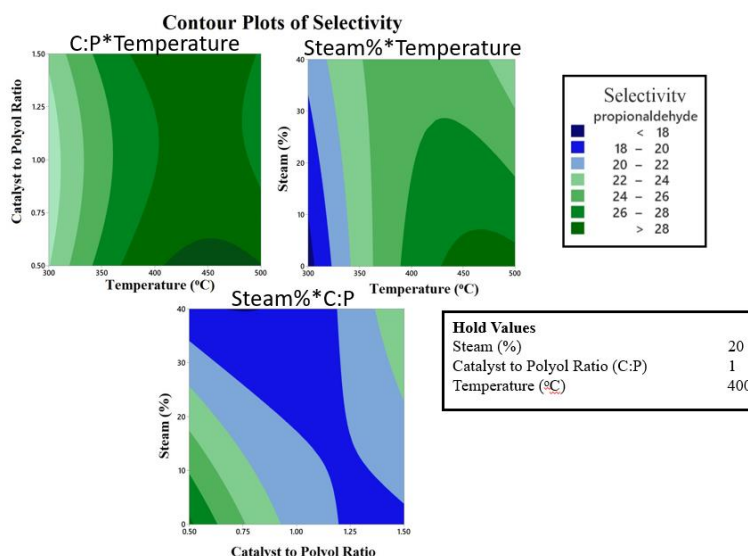


Figure 3.11: The contour plots for the DOE in version 3.0 of the reactor setup

The temperature vs. catalyst to polyol ratio contour plot displays a regional maximum at around 420-500 °C and 0.5-0.65, respectively. The temperature vs. steam percentage contour plot shows a regional maximum at 440-500°C and 0-7%, respectively. The catalyst to polyol ratio vs. steam percentage contour plot shows a very small regional maximum at around 0.5 and 0%, respectively. Similarly, to what was concluded from the Main Effects plots, there exist optimal reaction conditions for increasing the selectivity of

propionaldehyde from the model equation. However, these optimal conditions are represented as regions rather than a global maximum, as shown in the main effects plot.

The surface plot shown in Figure 3.12, represents the DOE model on a three-dimensional scale. Once again, there is a maximum selectivity displayed in the surface plot, but this point represents the absolute maximum interaction for temperature vs. the catalyst to polyol ratio. The DOE produces three surface plots, but the most important plot involves the temperature, as displayed in Figure 3.12. The other parameter, catalyst to polyol ratio in this case, is of little importance, as previously discussed.

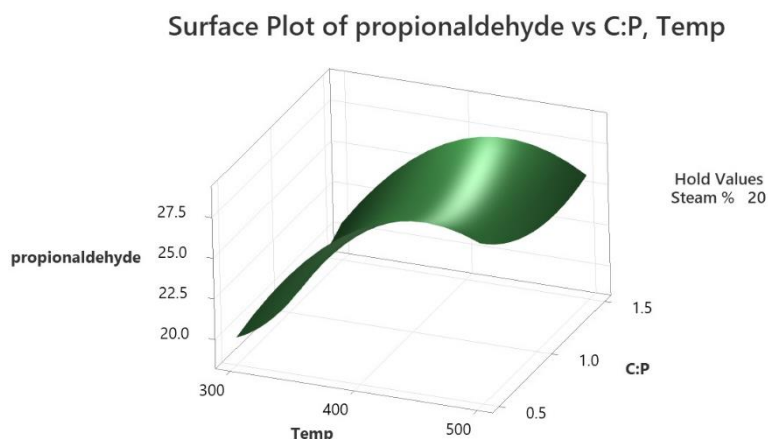


Figure 3.12: The Surface Plot for the catalyst to polyol ratio vs. temperature vs. propionaldehyde selectivity

In conclusion, the DOE has found the optimal reactions for the selectivity of propionaldehyde to be at a temperature of 450 °C while the catalyst to polyol ratio and the steam percentage had very little impact on the selectivity of propionaldehyde. Additionally, it is important to note that temperature and the temperature squared were deemed to be the only significant terms within the model equation.

Overall, the DOE was successful in optimizing the selectivity of propionaldehyde in the product gas. The optimal temperature found was to be the same as the seemingly

optimal temperature within the patent²⁸. The maximum propionaldehyde selectivity reported in the patent of 81.6% was achieved at a temperature of around 450 °C with a catalyst to polyol ratio of 10:1²⁸. A reduction from 10:1 to a much lower ratio, 1:2 at the lowest, is also an exceptional improvement. Despite the patent having minimal investigation of steam as a parameter, there was evidence within the patent that suggested steam may improve the overall selectivity of propionaldehyde²⁸. This was proven to not be the case; however, given the lack of correlation between the steam percentage and the selectivity of propionaldehyde within the model, experimental values within the patent may be within error.

3.3 Temperature Impact on Product Selectivity

Given the importance of temperature on this reaction based on the DOE conducted on version 3.0 of the reactor system, it is important to fully gauge its impact upon propionaldehyde as well as the other products. Using the experimental runs conducted in the preliminary phase of the DOE, Figure 3.7, temperature was plotted against selectivity of the seven main products, as seen in Figure 3.13.

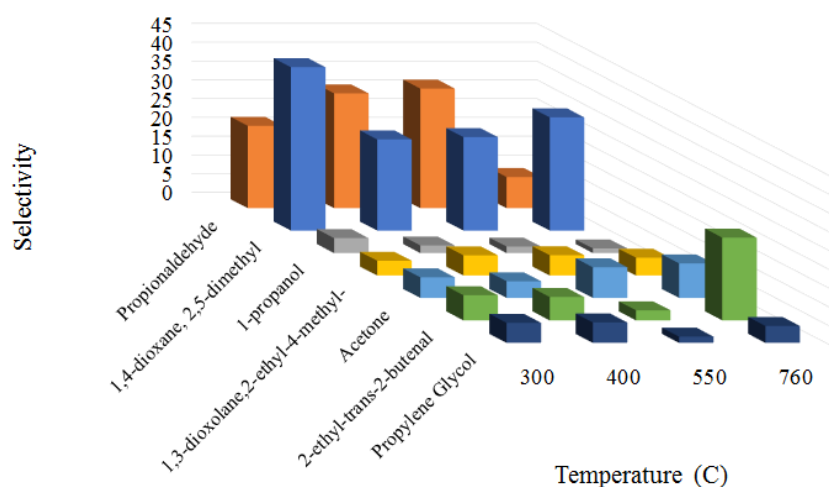


Figure 3.13: The effect of temperature on the selectivity of the primary seven products

It should be noted that these experiments were conducted with a 2:1 catalyst to polyol ratio and 20% steam in the carrier gas. As previously concluded from the DOE, the polyol ratio, and the steam percentage in the carrier gas result in little to no effect on the overall selectivity of propionaldehyde; therefore, the preliminary conditions for these said parameters were sufficient. Although clear trends are difficult to identify within Figure 3.13, temperature plays a large role on the selectivity of some of these products. Propionaldehyde exhibits a local maximum selectivity between 400 and 500 °C, much like the DOE results, while exhibiting a sharp decrease at the higher temperature. 1,4-dioxane, 2,5-dimethyl shows an unclear trend between temperature, as both low and high temperatures resulted in high selectivity. 1-propanol and propylene glycol show a decreasing trend in selectivity with increasing temperatures. 1,3-dioxolane, 2-ethyl-4-methyl; acetone; and 2-ethyl-trans-2-butenal show an increasing trend in selectivity with increasing temperatures. This is especially apparent with 2-ethyl-trans-2-butenal, which exhibits a very high selectivity at 760 °C compared to lower temperatures.

3.4 Initial Zeolite Testing

Prior to conducting the DOE on the reactor setup 3.0, a handful of zeolites with varying silica to alumina ($\text{SiO}_2/\text{Al}_2\text{O}_3$) ratios were tested. These zeolites included NH_4 -ZSM-5 (50:1) from Alpha Aesar, NH_4 -zeolite Y (5.1:1) from Alpha Aesar, and NH_4 -zeolite Beta (25:1) from Alpha Aesar. Additionally, gamma-phase Al oxide from Alpha Aesar was tested, as it has been shown to also have acidic sites⁹⁵. The selectivity of the seven products for these different zeolites and Al oxide are displayed in Table 3.3. It should also be noted that these samples were tested at a reaction temperature of 310 °C, a catalyst to polyol ratio of 2:1, and a steam percentage of 20% in the carrier gas on the model PPG polyol. The

total flow rate was 50 mL/min and the total polyol and catalyst mix added was 5 g. The propionaldehyde selectivity is also displayed in Figure 3.14.

Table 3.3: The selectivity of the primary seven products for different zeolites and gamma-phase Al oxide

Product	NH ₄ -ZSM-5 (50:1) Selectivity	NH ₄ -Zeolite Y (5.1:1) Selectivity	NH ₄ -Zeolite Beta (25:1) Selectivity	Al Oxide Selectivity
Propionaldehyde	26.91%	9.63%	20.37%	11.12%
Acetone	2.47%	2.63%	1.69%	2.42%
1-Propanol	4.36%	8.54%	4.31%	29.46%
1,3-Dioxolane, 2-ethyl-4-methyl-	6.69%	6.97%	4.42%	15.47%
1,4-Dioxane, 2,5-dimethyl-	34.01%	46.03%	34.63%	22.71%
2-Ethyl-trans-2-butenal	6.27%	9.18%	12.24%	2.52%
Propylene Glycol	5.22%	7.87%	6.26%	8.47%
Other Products	14.07%	9.15%	17.53%	7.83%

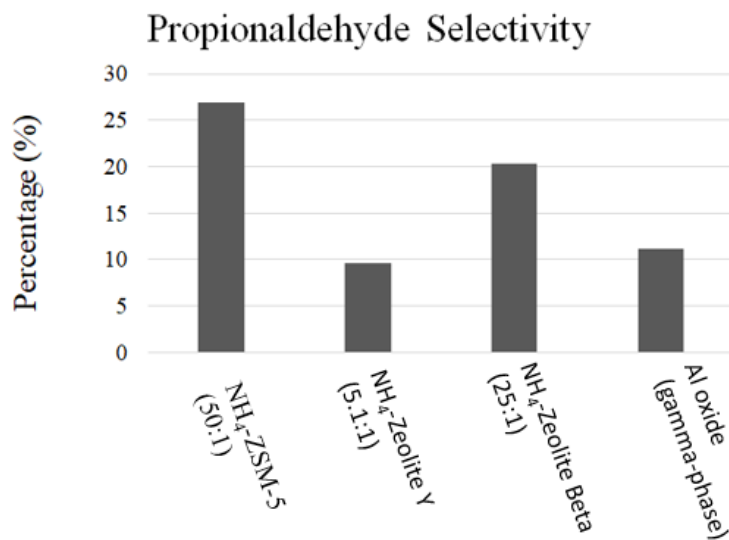


Figure 3.14: Propionaldehyde selectivity for different zeolites and gamma-phase Al oxide

Based on Figure 3.14 and Table 3.3, the NH₄-ZSM-5 (50:1) catalyst outperformed the NH₄-zeolite Y (5.1:1), NH₄-zeolite Beta (25:1), and the gamma-phase Al oxide

catalysts regarding the selectivity of propionaldehyde. Zeolite Y and the Al oxide catalysts showed very low selectivity to propionaldehyde. However, Al oxide demonstrated high selectivity toward 1-propanol while zeolite Y demonstrated high selectivity toward 1,4-dioxane, 2,5-dimethyl-. Zeolite Beta resulted in a propionaldehyde selectivity of over 20%; however, this is still quite lower than the 27% selectivity demonstrated by ZSM-5. The differences within the selectivity of these zeolites, can be largely attributed to the different structures of each zeolite and their concentration of acidic sites⁹⁶. Since the overall goal of the project is to maximize the selectivity of propionaldehyde, it was decided to solely focus on ZSM-5 as opposed to tested catalysts. Additionally, it should be noted that although these catalysts were not tested at the same silica to alumina ratios, a comparison between the catalysts were made to pre-maturely scan for catalyst with extremely high selectivity toward propionaldehyde. The only catalyst that really stood out from this initial comparison was ZSM-5. Pictures were also taken of the various pre-mixed catalysts and polyol prior to reaction, the spent catalysts, and the condenser fluid, as seen in Figure 3.15.

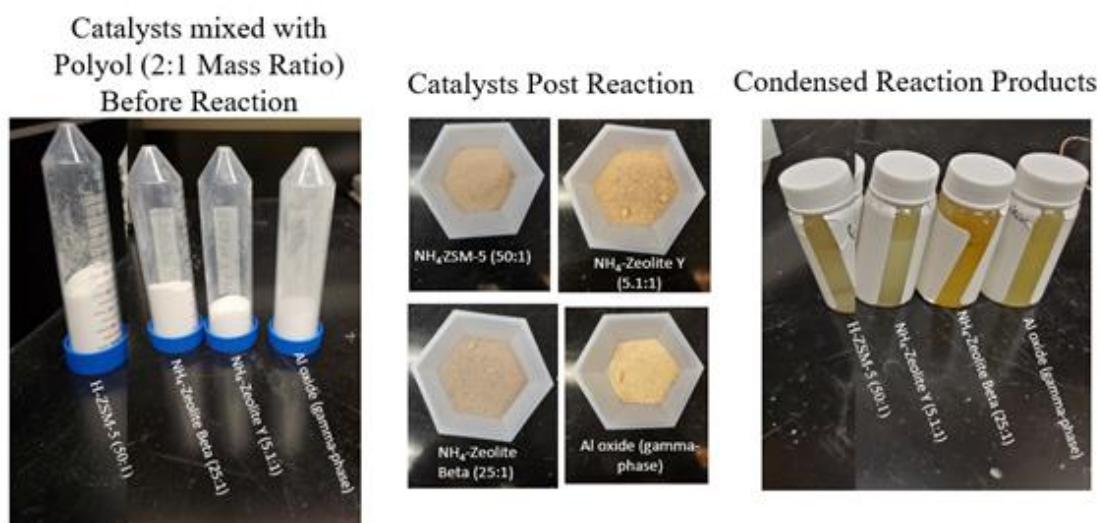


Figure 3.15: Pictures of the different catalysts tested and their respective condenser fluid

All the catalyst mixed with PPG appear white or off-white. However, upon reaction, ZSM-5 and zeolite-Beta turn a darker brown color while zeolite-Y and Al oxide turn more yellowish. The condenser fluids are of similar color, but the zeolite-Beta sample is slightly darker. This can be attributed to a higher selectivity toward 2-ethyl-trans-2-butenal, based on previous observations.

3.5 ZSM-5 Silica to Alumina Ratio Testing

Prior to conducting the DOE on the reactor setup 3.0, NH₄-ZSM-5 with varying silica to alumina (SiO₂/Al₂O₃) ratios were tested. These zeolites included the typical NH₄-ZSM-5 with silica to alumina ratios of 23:1, 30:1, 50:1, 80:1, and 200-400:1 all from Alpha Aesar. It should be noted that the NH₄-ZSM-5 from Zeolyst performed almost identically to the NH₄-ZSM-5 from Alpha Aesar, but for consistency, all the ZSM-5 samples were from Alpha Aesar. These samples were tested at a reaction temperature of 310 °C, a catalyst to polyol ratio of 2:1, and a steam percentage of 20% in the carrier gas on the model PPG polyol. The total flow rate was 50 mL/min and the total polyol and catalyst mix added was 5 g. The selectivity of the seven products for these different zeolites and Al oxide are displayed in Table 3.4. The propionaldehyde selectivity is also displayed in Figure 3.16.

Table 3.4: The selectivity of the primary seven products for NH₄-ZSM-5 of varying silica to alumina ratios

Product	NH ₄ -ZSM-5 (23:1) Selectivity	NH ₄ -ZSM-5 (30:1) Selectivity	NH ₄ -ZSM-5 (50:1) Selectivity	NH ₄ -ZSM-5 (80:1) Selectivity	NH ₄ -ZSM-5 (200-400:1) Selectivity
Propionaldehyde	11.03%	22.53%	26.91%	18.91%	18.01%
Acetone	3.5%	2.82%	2.47%	1.86%	5.88%
1-Propanol	3.05%	2.62%	4.36%	6.55%	2.12%
1,3-Dioxolane, 2-ethyl-4-methyl-	16.16%	8.21%	6.69%	18.97%	20.03%
1,4-Dioxane, 2,5-dimethyl-	30.54%	31.3%	34.01%	34.13%	34.53%
2-Ethyl-trans-2-butenal	12.63%	9.11%	6.27%	6.25%	4.04%
Propylene Glycol	12.96%	7.65%	5.22%	7.92%	10.33%
Other Products	10.13%	15.76%	14.07%	5.41%	5.06%

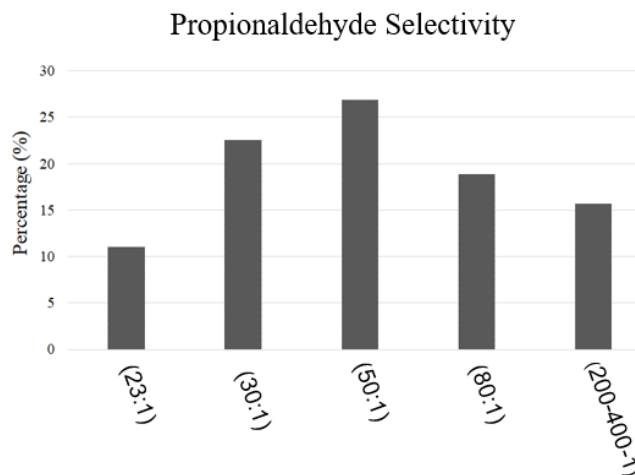


Figure 3.16: Propionaldehyde selectivity for varying silica to alumina ratios of NH₄-ZSM-5 catalysts

Based on Figure 3.16 and Table 3.4, the NH₄-ZSM-5 samples display a maximum propionaldehyde selectivity at the 50:1 ratio sample. The more alumina present within the catalyst, the more acidic sites are present. Thus, the lower the silica to alumina ratio, the greater the amount of catalytic cracking that occurs. However, this does not always lead to

an increase in selectivity for targeted products, as seen in Figure 3.16. Based on these results, the optimal silica to alumina ratio for increasing selectivity toward propionaldehyde is 50:1. Too low and too high of a silica to alumina ratio may present issues with reactant conversion and selectivity optimums, as has been observed in the conversion of methanol to propene over ZSM-5 catalysts⁹⁷.

Pictures were also taken of the various pre-mixed catalysts and polyol prior to reaction, the spent catalysts, and the condenser fluid, as seen in Figure 3.17.

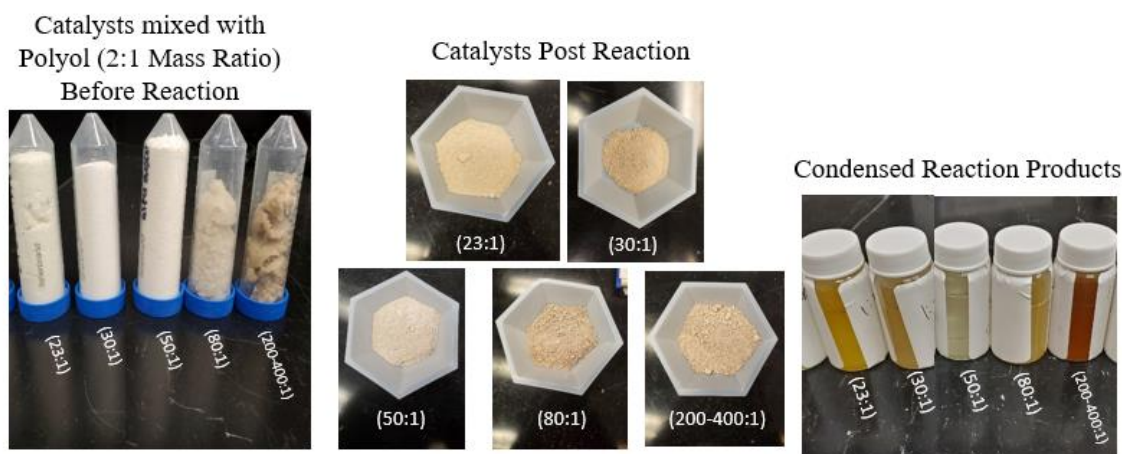


Figure 3.17: Pictures of the ZSM-5 catalysts tested with varying silica to alumina ratios and their respective condenser fluid

The ZSM-5 samples with low silica to alumina ratios appear to be slightly yellow in color while the higher silica to alumina ratios appear to be darker in color, almost brownish. It is interesting to note that this coloring is apparent from the pre-mixed catalysts before reaction, the spent catalyst, and the condenser fluid for all the samples. Another interesting phenomenon present within the pre-mixed catalyst samples are differences within wetting parameters between samples. The differences in wetting of ZSM-5 with varying silica to alumina ratios has been previously observed and described⁹⁸.

3.6 Meso-porous Zeolite-Y Testing

Prior to conducting the DOE on the reactor setup 3.0, zeolite-Y samples, synthesized at UC Berkeley as previously discussed in section 2.5.2 Mesoporous zeolite Synthesis Methodology, were tested along with their microporous counter parts. Mesoporous NH₄-zeolite-Y samples with alumina ratios of 15:1 and 30:1 were tested along with H-zeolite-Y samples with alumina ratios of 15:1 and 30:1. These samples were tested at a reaction temperature of 310 °C, a catalyst to polyol ratio of 2:1, and a steam percentage of 20% in the carrier gas on the model PPG polyol. The total flow rate was 50 mL/min and the total polyol and catalyst mix added was 5 g. The selectivity of the seven products for different zeolite-Y samples are displayed in Table 3.5. The propionaldehyde selectivity is also displayed in Figure 3.18.

Table 3.5: The selectivity of the primary seven products for the various zeolite-Y samples

Product	NH ₄ -Meso-Zeolite Y (15:1) Selectivity	NH ₄ -Meso-Zeolite Y (30:1) Selectivity	H-Zeolite Y (15:1) Selectivity	H-Zeolite Y (30:1) Selectivity
Propionaldehyde	22.93%	27.69%	12.68%	16.02%
Acetone	9.87%	13.81%	3.11%	9.31%
1-Propanol	5.33%	3.83%	3.39%	2.65%
1,3-Dioxolane, 2-ethyl-4-methyl-	7.77%	12.63%	26.35%	32.81%
1,4-Dioxane, 2,5-dimethyl-	27.18%	25.12%	38.91%	33.5%
2-Ethyl-trans-2-butenal	6.52%	5.3%	1.82%	1.71%
Propylene Glycol	5.95%	6.34%	2.42%	1.52%
Other Products	14.45%	5.28%	11.32%	2.48%

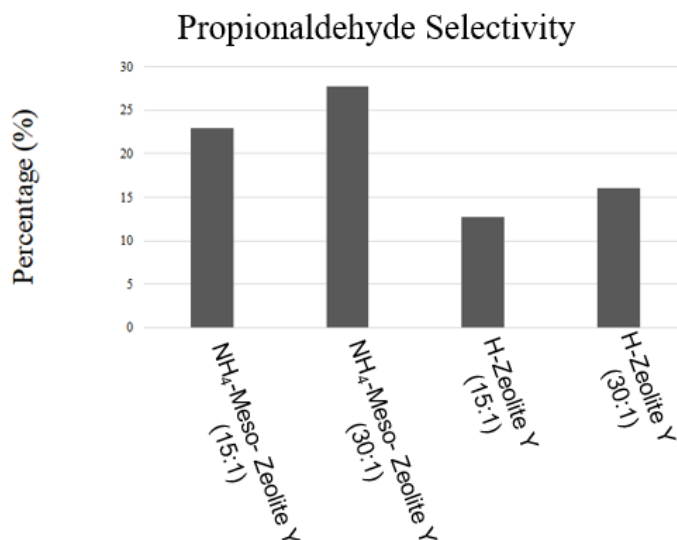


Figure 3.18: Propionaldehyde selectivity for various zeolite-Y samples

Based on Figure 3.18 and Table 3.4, the meso-porous variants of zeolite-Y outperformed their respective micro-porous variants regarding propionaldehyde selectivity. Additionally, both samples favored the 30:1 silica to alumina ratio compared to the 15:1 silica to alumina ratio sample regarding the selectivity of propionaldehyde. Overall, the microporous zeolite-Y samples had higher selectivity to large compounds such as 1,3-dioxolane, 2-ethyl-4-methyl- and 1,4-dioxane, 2,5-dimethyl- while the mesoporous samples had higher selectivity to smaller compounds such as propionaldehyde and acetone. That is to say that the meso-porous samples were likely more successful at allowing larger products and reactants to react to form acetone and propionaldehyde.

Pictures were also taken of the various pre-mixed catalysts and polyol prior to reaction, the spent catalysts, and the condenser fluid, as seen in Figure 3.19.

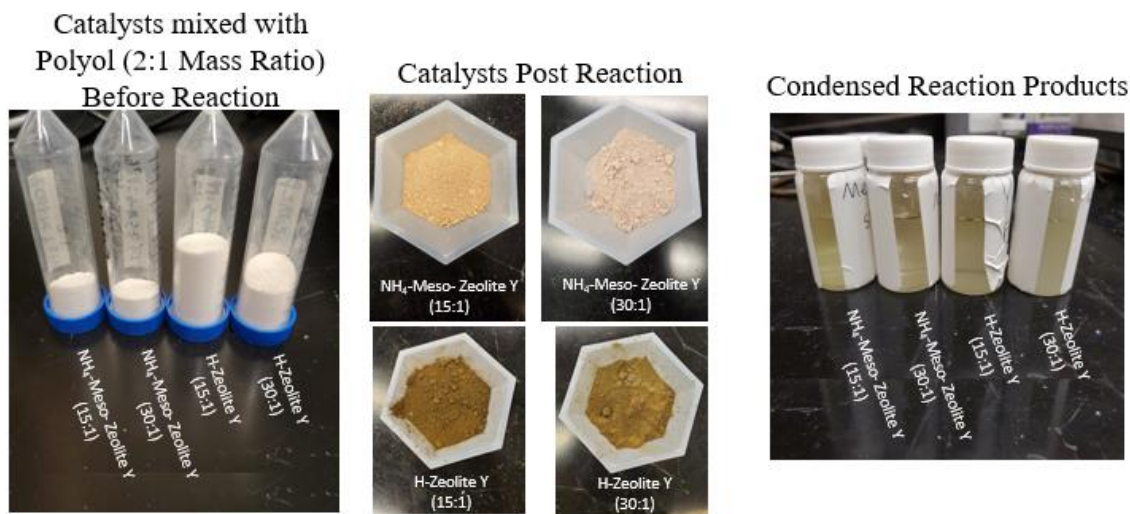


Figure 3.19: Pictures of the zeolite-Y catalysts tested with varying porosity and silica to alumina ratios and their respective condenser fluid

All pre-mixed samples appeared white or off-white prior to the reaction. The condenser fluid color, slightly yellow, was also uniform for all samples, which can once again be attributed to the low concentration of 2-ethyl-trans-2-butenal within the product condensate. Much like the low silica to alumina ratio ZSM-5 samples, the 15:1 silica to alumina ratio meso-porous zeolite-Y spent sample appeared yellow while the 30:1 sample appeared an almost cream color. For the microporous zeolite-Y samples, both the 15:1 and 30:1 spent samples appeared to be very brown in color, with almost no apparent distinction between the two samples.

3.7 Thermal Cracking of PPG

As previously discussed in 2.6 Reaction Conversion and Selectivity Methodology via Liquid Chromatography-Mass Spectrometer, the selectivity of the products was redefined for all remaining experimental data, unless otherwise specified. Much like before, the areas of these seven products were adjusted accordingly and their concentrations calculated. These concentrations were summed, and the selectivity was

defined as the concentration of a single product over the total concentration. This was done to prevent reactants, namely di-propylene glycol, from interfering with product selectivity.

To gauge the effect of the catalyst on the cracking reaction, a baseline for cracking due to thermal decomposition needed to be developed. Thus, PPG was mixed with sand instead of a catalyst to suspend it within the reactor. Since sand is inert, the resulting products should only be from thermal degradation. The results for this experiment are displayed in Table 3.6. These samples were tested at a reaction temperature of 400 °C, a steam percentage of 20% in the carrier gas, and a total flow rate of 100 mL/min on model PPG polyol. The catalyst sample also had a catalyst to polyol ratio of 1:1 and a total mass of mixed polyol and catalyst of 5 g.

Table 3.6: The selectivity of the primary seven products via NH₄-ZSM-5 catalyst and thermal cracking

Product	Thermal Cracking Selectivity	NH ₄ -ZSM-5 Selectivity
Propionaldehyde	7.11%	49.28%
Acetone	64.83%	6.85%
1-Propanol	6.31%	1.61%
1,3-Dioxolane, 2-ethyl-4-methyl-	10.70%	8.95%
1,4-Dioxane, 2,5-dimethyl-	Trace	22.03%
2-Ethyl-trans-2-butenal	Trace	4.17%
Propylene Glycol	11.05%	7.11%

Based on the results in Table 3.6, the thermal cracking resulted in a very high selectivity toward acetone when compared to the NH₄-ZSM-5 catalyst. It also resulted in very low selectivity of large products like 1,4-dioxane, 2,5-dimethyl-. However, the

conversion was the most important factor of this experiment; thus, these samples were also run through the LC-MS, as shown in Figure 3.20.

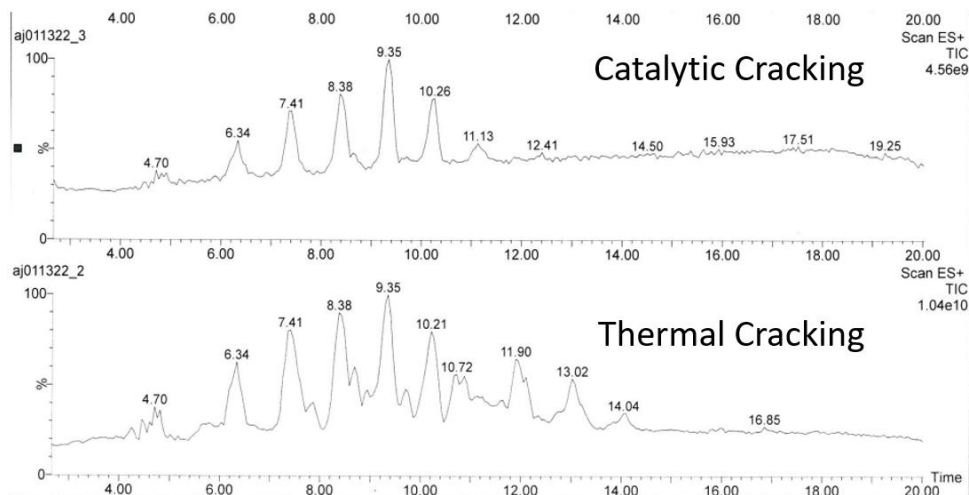


Figure 3.20: The LC-MS chromatogram for the catalytic and thermal cracking samples

The resulting peak areas shown in Figure 3.20 were summed for both samples. The concentration of the two samples was then calculated using the total peak area and the PPG calibration curve, Figure 2.18. The total peak area for the thermal cracking sample was about 18 times greater than the total peak area for the catalytic sample. Indicating that the catalyst improved the reactivity of cracking reaction by approximately 18 times. This was also in agreement with the GC-MS conversion methodology, which involved a comparison of the total product area for the primary seven products for the two samples. This comparison showed an increase in product conversion of about 20 times through the addition the catalyst.

3.8 H-ZSM-5 vs. NH_4 -ZSM-5

NH_4 -ZSM-5 is typically thermally decomposed to H-ZSM-5 via calcination prior to use^{99–102}. Calcination not only allows further stability enhancement, but it also allows the zeolite to become acidic in nature via the H^+ protonic species¹⁰². However, NH_4 -ZSM-

5 was predominately used for preliminary data and the DOEs. Thus, the true acid cracking potential of H-ZSM-5 may not have been completely realized in the previous experimental results. Thus, NH₄-ZSM-5 and H-ZSM-5 were directly compared in terms of selectivity, as seen in Table 3.7. H-ZSM-5 was produced via the calcination procedure discussed in Section 2.5.1 H-ZSM-5 Synthesis Methodology. Additionally, these samples were tested at a reaction temperature of 450 °C, a catalyst to polyol ratio of 1:1, and a steam percentage of 20% in the carrier gas on the model PPG polyol. The total flow rate was 100 mL/min and the total polyol and catalyst mix added was 5 g.

Table 3.7: The selectivity of the primary seven products via H-ZSM-5 and NH₄-ZSM-5 catalysts

Product	NH ₄ -ZSM-5 Selectivity	H-ZSM-5 Selectivity
Propionaldehyde	49.28%	49.64%
Acetone	6.85%	4.43%
1-Propanol	1.61%	1.18%
1,3-Dioxolane, 2-ethyl-4-methyl-	8.95%	12.38%
1,4-Dioxane, 2,5-dimethyl-	22.03%	25.36%
2-Ethyl-trans-2-butenal	4.17%	5.21%
Propylene Glycol	7.11%	1.77%

Based on the results in Table 3.7, it can be concluded that the NH₄-ZSM-5 resulted in nearly identical results as H-ZSM-5. Based on previous results, these values can likely all be considered within experimental error of one another. Additionally, both these catalysts were run several times; thus, solidifying the evidence that NH₄-ZSM-5 produces nearly the same product selectivity as H-ZSM-5. The conversion was estimated to also be similar based on the peak area of products resulting from the GC-MS. This is likely due to

the conversion of NH₄-ZSM-5 to H-ZSM-5 during the reaction. At a reaction temperature of 450 °C, the thermal decomposition of ammonium to hydrogen should readily proceed^{99–102}. It is also interesting to note that the stability and the framework structure of a zeolite can be affected by the calcination temperature^{99–102}. Thus, it stands to reason that the reaction temperature may affect the selectivity of the products when comparing NH₄-ZSM-5 to H-ZSM-5. It has also been shown that steam may drastically increase the activity of a zeolite⁹⁹.

3.9 Pt-H-ZSM-5 vs. H-ZSM-5

Pt-H-ZSM-5 was synthesized following the procedure described in 2.5.3 Pt-H-ZSM-5 Synthesis Methodology. As previously discussed, the introduction of precious metals into a zeolite's framework, can drastically improve its longevity in cracking reactions while having no adverse effects on product yield⁵¹. As such, Pt-H-ZSM-5 was tested with the catalytic cracking of PPG reaction to investigate potential benefits of Pt within the framework of ZSM-5; the resulting product selectivity is shown in Table 3.8. These samples were tested at a reaction temperature of 450 °C, a catalyst to polyol ratio of 1:1, and a steam percentage of 20% in the carrier gas on the model PPG polyol. The total flow rate was 100 mL/min and the total polyol and catalyst mix added was 5 g.

Table 3.8: The selectivity of the primary seven products via H-ZSM-5 and Pt-H-ZSM-5 catalysts

Product	H-ZSM-5 Selectivity	Pt-H-ZSM-5 Selectivity
Propionaldehyde	49.28%	25.62%
Acetone	6.85%	Trace
1-Propanol	1.61%	1.86%
1,3-Dioxolane, 2-ethyl-4-methyl-	8.95%	13.02%
1,4-Dioxane, 2,5-dimethyl-	22.03%	52.87%
2-Ethyl-trans-2-butenal	4.17%	6.22%
Propylene Glycol	7.11%	2.95%

Based on the results in Table 3.8, Pt-H-ZSM-5 resulted in a much lower propionaldehyde selectivity compared to H-ZSM-5. Pt-H-ZSM-5 also resulted in higher selectivity toward larger molecules like 1,3-dioxolane, 2-ethyl-4-methyl and 1,4-dioxane, 2,5-dimethyl-. Additionally, the GC-MS total peak areas for the products indicated an approximate 80% lower conversion for the Pt-H-ZSM-5 sample when compared to ZSM-5 catalyst. Thus, it can be concluded the catalytic cracking potential of H-ZSM-5 was not improved through the incorporation of Pt into its framework for this particular reaction.

3.10 2-D MFI Zeolite Testing

2-D MFI zeolites nanosheets have been shown to drastically improve the reactivity of the catalyst in certain reactions⁶⁷. This increase in activity can be attributed to the removal of internal diffusion limitations, as the catalytic sites on the zeolite now reside on the surface. Thus, it is of great interest to test the capabilities of these 2-D MFI zeolites for the catalytic cracking of PPG reaction. Unfortunately, the synthesized amount of 2-D MFI

zeolite with a silica to alumina ratio of 5:1 without stirring was not enough for a reaction run. However, there was enough sample to test the mixed and non-mixed MFI nanosheets with a silica to alumina ratio of 25:1. These samples were tested at a reaction temperature of 450 °C, a catalyst to polyol ratio of 1:1, and a steam percentage of 20% in the carrier gas on the model PPG polyol. The total flow rate was 100 mL/min and the total polyol and catalyst mix added was 5 g. The results of these two experimental tests as well as H-ZSM-5 are displayed in Table 3.9.

Table 3.9: The selectivity of the primary seven products via the non-mixed and mixed MFI zeolites as well as H-ZSM-5

Product	H-ZSM-5 (50:1) Selectivity	W/O stirring MFI Zeolite (Si/Al=50)	W Stirring MFI Zeolite (Si/Al=50)
Propionaldehyde	49.28%	58.42%	69.30%
Acetone	6.85%	9.69%	10.91%
1-Propanol	1.61%	1.05%	0.80%
1,3-Dioxolane, 2-ethyl-4-methyl-	8.95%	8.42%	5.41%
1,4-Dioxane, 2,5-dimethyl-	22.03%	18.39%	6.09%
2-Ethyl-trans-2-butenal	4.17%	2.66%	5.56%
Propylene Glycol	7.11%	1.37%	1.93%

Based on Table 3.9, the of MFI zeolites with and without stirring both displayed higher selectivity for propionaldehyde than H-ZSM-5. Although the MFI zeolite sample without stirring performed only slightly better than H-ZSM-5, the MFI zeolite with stirring performed significantly better than H-ZSM-5. In fact, out of all the zeolites tested thus far, this synthesized MFI zeolite with stirring outperformed all previous zeolites quite significantly with a propionaldehyde selectivity of nearly 70%. However, both catalysts

seem to have low conversion (approximately 25% for mixed and 34% for non-mixed) compared to H-ZSM-5 according to the GC-MS peak areas.

3.11 Additional Polyols Tested

Besides polypropylene glycol Mn ~425, polyurethane (Texin® 950 D from Covestro) was tested. The testing of this compound was done using version 1.0 of the experimental setup. As such, the resulting GC-MS chromatogram, in Figure 3.21, displays the result of the products in the gas phase. For this particular run, the catalyst and polyol mixture reacted at a temperature of 250 °C, a steam percentage of 20% in the carrier gas, and a catalyst to polyol ratio of 2:1. Also, the total flow rate of the experimental run was 25 mL/min with a total catalyst and polyol mass of 1.5 g. It should also be noted that the polyurethane used for this reaction was a solid, thus it simply thrown in with NH₄-ZSM-5 catalyst and reacted.

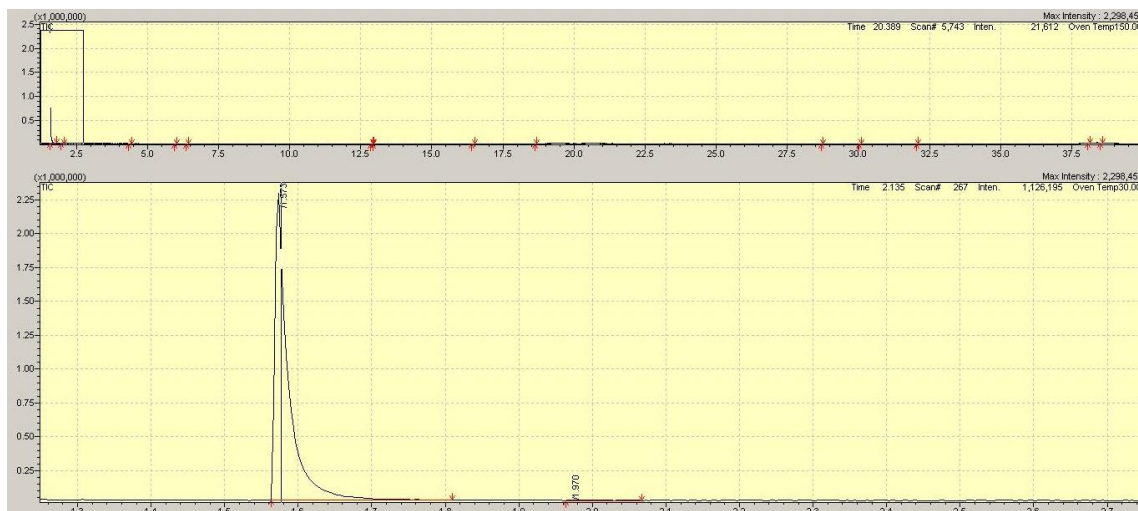


Figure 3.21: GC-MS chromatogram of the catalytic cracking of polyurethane reaction

Based on Figure 3.21, there exists one primary volatile product for this reaction, which was identified to be tetrahydrofuran (THF). Although version 1.0 of the reactor setup presented many errors, the potential for the catalytic breakdown of polyurethane into THF

seemed promising. Additionally, one more experiment regarding polyurethane was conducted without a catalyst. The results are almost identical, but reduced in peak area, as that displayed in Figure 3.21. Although further experimentation was not conducted, it was hypothesized that the polyurethane was furan based, which was based on a literature search regarding the THF product¹⁰³.

3.12 Spent Catalyst Characterization

An important aspect of understanding the overall chemistry of this catalytic cracking reaction involves the characterization of the spent zeolite catalysts. Various characterization methods were employed on the spent zeolites such as thermogravimetric analysis (TGA), X-ray powder diffraction (XRPD), diffuse reflectance for infrared Fourier transform spectroscopy (DRIFTS), and positron annihilation lifetime spectroscopy (PALS). An in-depth look at the results of these characterization methods will be discussed in the proceeding subsections. One of the primary concerns regarding catalytic chemistry of hydrocarbons is coking⁷⁷. Coking, which is the buildup of carbonaceous materials on a catalyst surface, can greatly hinder the catalytic performance of a catalyst^{50,51,77,78}. As such, these characterization methods primarily focus on the characterization of potential coke buildup on/in the zeolite structure.

3.12.1 PXRD Characterization of Spent ZSM-5

It has been reported in the literature that zeolites can incur crystallographic changes during cracking reactions^{51,104}. Thus, X-ray powder diffraction was performed on a fresh ZSM-5 sample and the five times reacted sample. These experiments occurred in version 1.0 of the reactor system; however, this should not change the outcome of the spent catalyst. The ZSM-5 samples were run with polypropylene glycol Mn ~425 and were conducted

with a steam percentage of 20%, a temperature of 250 °C, a catalyst to polyol ratio of 2:1, and with a total carrier gas flow of 25 mL/min. Additionally, this catalyst was reacted a total of five times within the reactor. This was done by removing the top piece of quartz wool in the reactor tube and adding additional polyol at the top of the tube following each run. This five times reacted experiment was conducted to increase the overall coke deposits on/in the zeolite, as this characterization method was almost inconclusive with a singularly reacted sample.

Figure 3.22 displays the normalized PXRD pattern for the two samples of interest. Despite the large 2-theta region analyzed, crystalline changes in the zeolite structure, due to the deposition of coke, have been reported in the literature to occur on the largest peaks, which occur at about 22.5-25⁵¹. Thus, Figure 13 only displays the region of interest. Additionally, the fresh ZSM-5 sample was shifted to the left by about 0.27° due to calibration error for comparison purposes. Literature values for spent ZSM-5 samples resulted in a lower intensity, about 20-30%, when compared to the unreacted sample⁵¹. Based on Figure 3.22, there is no substantial changes in intensity from fresh ZSM-5 compared to the five times reacted ZSM-5 sample. Thus, it can be concluded that there are no substantial crystalline changes in the structure of ZSM-5 during the catalytic cracking reaction.

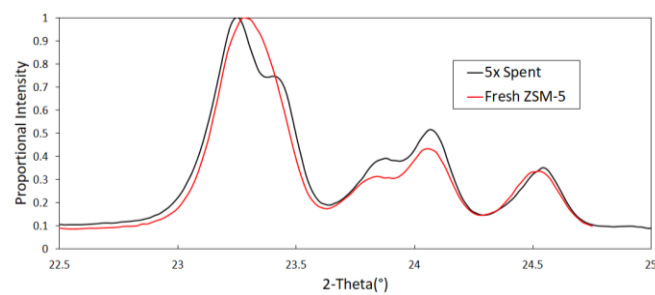


Figure 3.22: PXRD pattern for the 5x reacted ZSM-5 sample and a fresh ZSM-5 sample

3.12.2 DRIFTS Characterization of Spent ZSM-5

Diffuse reflectance for infrared Fourier transform spectroscopy (DRIFTS) was conducted to identify coke and the potential types of coke deposited on the zeolite. Initially, a fresh ZSM-5 sample was loaded and used as the background for the five times reacted ZSM-5 sample scan. These experiments occurred in version 1.0 of the reactor system; however, this should not change the outcome of the spent catalyst. The ZSM-5 samples were run with polypropylene glycol Mn ~425 and were conducted with a steam percentage of 20%, a temperature of 250 °C, a catalyst to polyol ratio of 2:1, and with a total carrier gas flow of 25 mL/min. Additionally, this catalyst was reacted a total of five times within the reactor for reasons explained previously.

Figure 3.23 displays the infrared spectrum for the five times reacted ZSM-5 sample after baseline adjustment. The broad peak at around 3200-3650 cm^{-1} corresponds to O-H bonds and the other broad peak at 2800-3050 corresponds to C-H bonds¹⁰⁵⁻¹⁰⁷. The largest peak at 1700 cm^{-1} corresponds to C=O bonds¹⁰⁵⁻¹⁰⁷. The two smaller peaks at 1550 cm^{-1} and 1450 cm^{-1} correspond to C=C and C-H bonds, respectively¹⁰⁵⁻¹⁰⁷. Additionally, this C=C double bond is likely due to the presence of an alkene functional group as opposed to an aromatic, as an aromatic would occur closer to 1600-1650 cm^{-1} ¹⁰⁶. Lastly, the peaks at 1250 and 1150 cm^{-1} correspond to C-O bonds¹⁰⁵⁻¹⁰⁷. A more in-depth analysis of these bands could result in the identification of the type of coke being formed; regardless, the infrared spectrum gives evidence of carbonaceous species on the surface of the spent ZSM-5 catalyst.

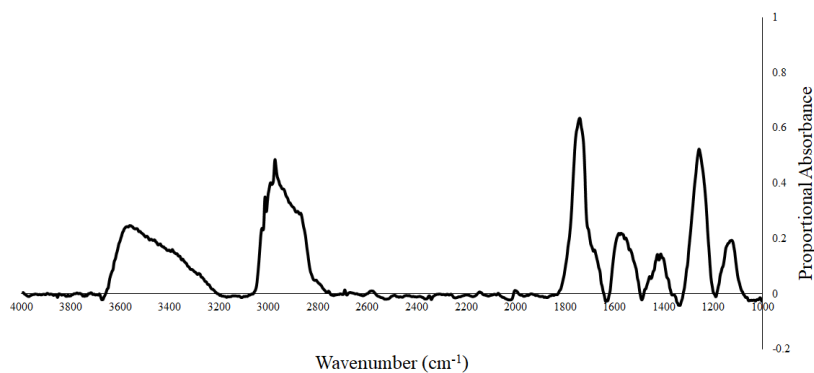


Figure 3.23: Baseline adjusted IR spectrum of 5x reacted ZSM-5

3.12.3 TGA Characterization of Spent Zeolites

3.12.3.1 5x Reacted ZSM-5

TGA was conducted on many of the catalyst samples previously discussed. However, an initial investigation regarding the identification of coke was conducted on the 5x reacted spent ZSM-5 catalyst. These experiments occurred in version 1.0 of the reactor system; however, this should not change the outcome of the spent catalyst. The ZSM-5 samples were run with polypropylene glycol Mn ~425 and were conducted with a steam percentage of 20%, a temperature of 250 °C, a catalyst to polyol ratio of 2:1, and with a total carrier gas flow of 25 mL/min. Additionally, this catalyst was reacted a total of five times within the reactor for reasons explained previously.

Figure 3.24 displays the normalized results from TGA run with the five times reacted ZSM-5 in air and argon. The total run constitutes a mass loss of almost 30% for both gases; however, there was a significantly more abrupt mass loss in the presence of air compared to argon at a temperature of around 150 °C. This abrupt mass loss can be contributed to the reduction of energy required to burn carbon off the ZSM-5 than what is required to thermally desorb it¹⁰⁸. Thus, these results indicate the presence of carbonaceous species on the spent ZSM-5 sample.

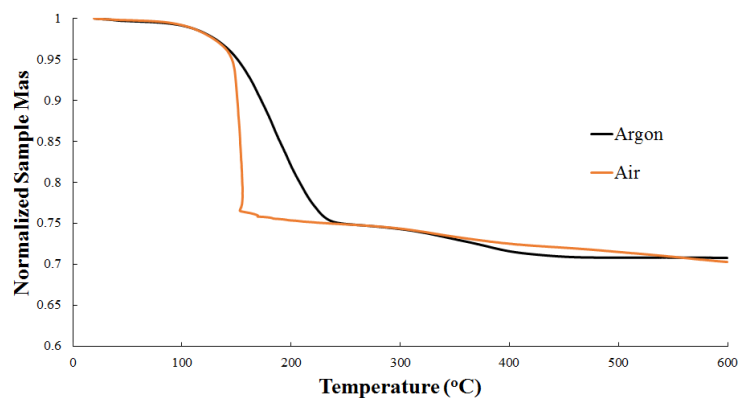


Figure 3.24: TGA for the 5x reacted ZSM-5 catalyst in argon and air

3.12.3.2 Effect of Steam Percentage on Coking

The NH_4 -ZSM-5 samples tested during the preliminary testing for the DOE conducted in version 3.0 of the reactor system were also investigated. As previously discussed, steam has been shown to inhibit secondary reaction that may potentially lead to coking.^{40–42} Therefore, TGA was conducted on the three preliminary spent NH_4 -ZSM-5 samples with varying steam percentages. These samples were run at a reaction temperature of 310 °C, a catalyst to polyol ratio of 2:1, and with steam percentages in the carrier gas of 0%, 20%, and 37%. The resulting normalized mass losses are displayed in Figure 3.25.

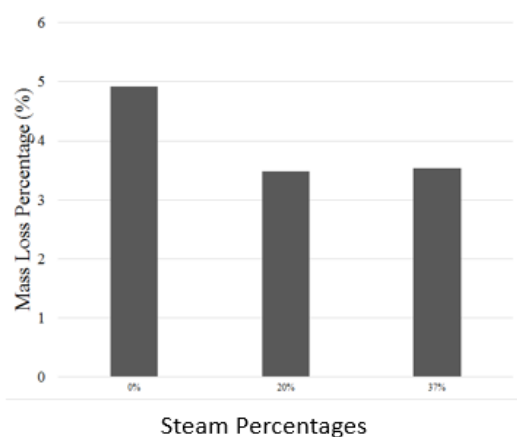


Figure 3.25: TGA mass loss of spent NH_4 -ZSM-5 samples with varying steam percentages

Based on Figure 3.25, there is a noticeable decrease in mass loss as the steam percentage increased. Thus, it can be concluded that the addition of steam can reduce the overall coking on/in the zeolite. This is an agreement to the previously discussed benefits of steam regarding the inhibition of secondary reactions that may potentially lead to coking⁴⁰⁻⁴².

3.12.3.3 Coking on Various Catalysts

TGA was conducted on the various zeolites discussed in section 3.4 Initial Zeolite Testing. These zeolites included NH₄-ZSM-5 (50:1) from Alpha Aesar, NH₄-zeolite Y (5.1:1) from Alpha Aesar, and NH₄-zeolite Beta (25:1) from Alpha Aesar. Additionally, gamma-phase Al oxide from Alpha Aesar was tested, as it has been shown to also have acidic sites⁹⁵. The selectivity of the seven products for these different zeolites and Al oxide are displayed in Table 3.3. It should also be noted that these samples were tested at a reaction temperature of 310 °C, a catalyst to polyol ratio of 2:1, and a steam percentage of 20% in the carrier gas on the model PPG polyol. The total flow rate was 50 mL/min and the total polyol and catalyst mix added was 5 g. The TGA curves for these catalysts are displayed in Figure 3.26 and their respective normalized mass losses are displayed in Figure 3.27.

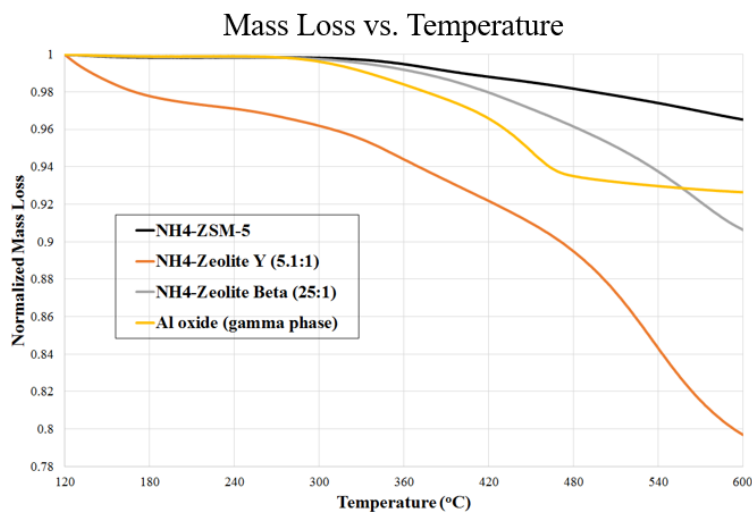


Figure 3.26: TGA curves for various spent catalysts

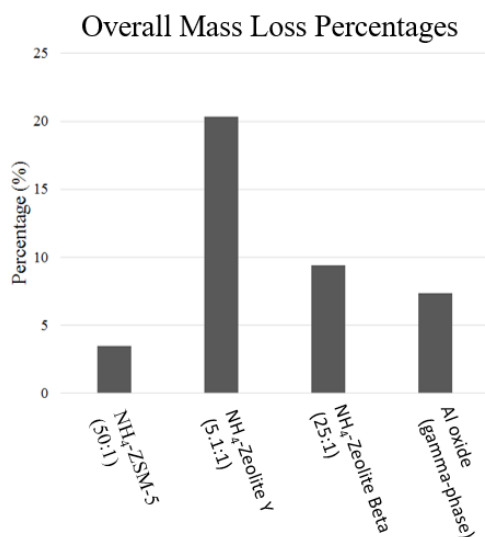


Figure 3.27: Normalized TGA mass loss of various spent catalysts

Based on Figure 3.26 and 3.27, the zeolite Y catalyst experienced an extremely mass loss compared to the other catalysts, which was assumed to be from the result of coking. Zeolite Beta also experienced a high amount of coking compared to NH₄-ZSM-5, which experienced the lowest amount of coke of all four catalysts. This can be attributed to the different zeolite structures as well as the higher concentration of Brønsted acid sites within

zeolite Beta compared to ZSM-5¹⁰⁹. Pictures of all the various spent catalysts are also displayed in Figure 3.15.

3.12.3.4 Effect of Silica to Alumina Ratio of NH₄-ZSM-5 on Coking

TGA was conducted on the NH₄-ZSM-5 catalysts with varying silica to alumina ratios discussed in section 3.5 ZSM-5 Silica to Alumina Ratio Testing. These zeolites included the typical NH₄-ZSM-5 with silica to alumina ratios of 23:1, 30:1, 50:1, 80:1, and 200-400:1 all from Alpha Aesar. It should be noted that the NH₄-ZSM-5 from Zeolyst performed almost identically to the NH₄-ZSM-5 from Alpha Aesar, but for consistency, all the ZSM-5 samples were from Alpha Aesar. These samples were tested at a reaction temperature of 310 °C, a catalyst to polyol ratio of 2:1, and a steam percentage of 20% in the carrier gas on the model PPG polyol. The total flow rate was 50 mL/min and the total polyol and catalyst mix added was 5 g. The resulting TGA curves for the spent NH₄-ZSM-5 catalysts are displayed in Figure 3.28 and their respective normalized mass losses are displayed in Figure 3.29.

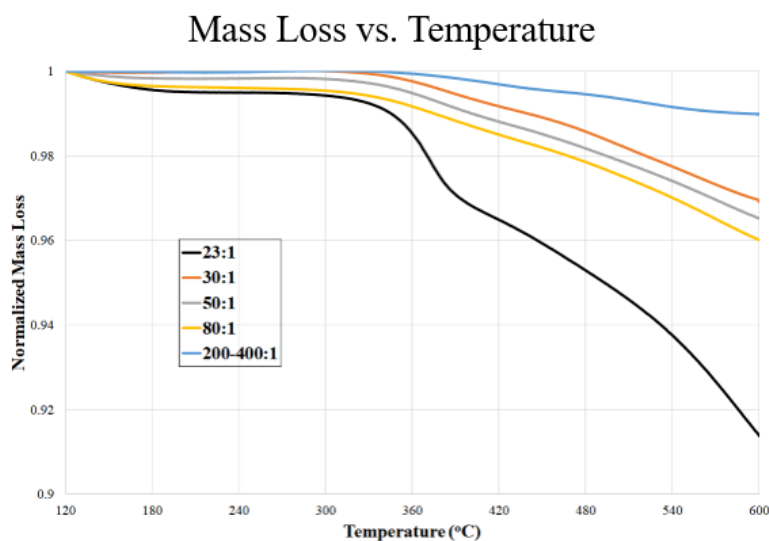


Figure 3.28: TGA curves for spent NH₄-ZSM-5 catalysts with varying silica to alumina ratios

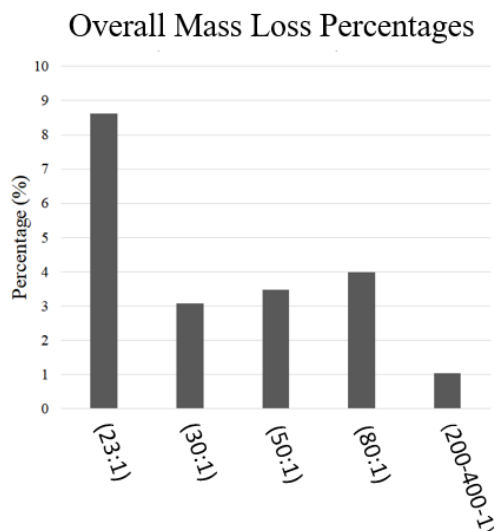


Figure 3.29: Normalized TGA mass loss for spent NH₄-ZSM-5 catalysts with varying silica to alumina ratios

Based on Figure 3.28 and 3.29, there is likely a trend between the alumina to silica ratio and the amount of coke formed on the catalyst. Based on the experimental data, the more alumina present within the zeolite sample, which can be correlated to the amount of acidic sites present, the more coking on/in the catalysts resulted from the reaction. Although the trend for the ratios is not as clear for the 30:1, 50:1, and 80:1 catalysts, the coking amount of said catalysts is still within experimental error; as such, the observed trend still holds. The observed trend is in agreement with the hypothesis that an increased number of acidic sites will result in an increased amount of coke. Therefore, it can be concluded that ZSM-5 samples with a large amount of alumina present will result in a large amount of coke on/in the spent zeolite due to the higher concentration of acidic sites¹¹⁰.

3.12.3.5 Meso-porous Zeolite Y Catalysts

TGA was conducted on the meso-porous and microporous zeolite-Y samples synthesized at UC Berkeley discussed in section 2.5.2 Mesoporous zeolite Synthesis Methodology and section 3.5 ZSM-5 Silica to Alumina Ratio Testing. Meso-porous NH₄-zeolite-Y samples with alumina ratios of 15:1 and 30:1 were tested along with H-zeolite-

Y samples with alumina ratios of 15:1 and 30:1. These samples were tested at a reaction temperature of 310 °C, a catalyst to polyol ratio of 2:1, and a steam percentage of 20% in the carrier gas on the model PPG polyol. The total flow rate was 50 mL/min and the total polyol and catalyst mix added was 5 g. The TGA curves for the spent zeolite-Y mesoporous and microporous catalysts are displayed in Figure 3.30 and their respective normalized mass losses are displayed in Figure 3.31.

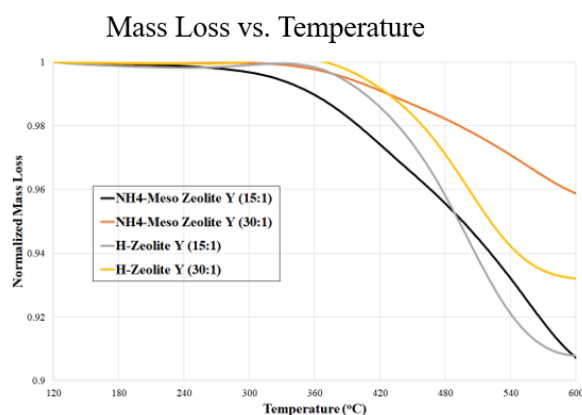


Figure 3.30: TGA curves for the spent meso-porous and microporous zeolite-Y catalysts

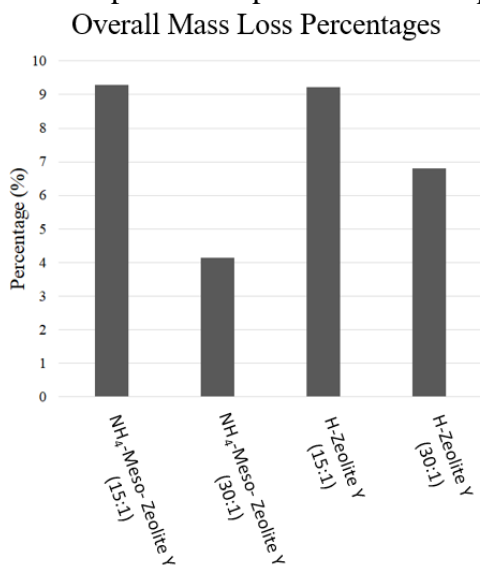


Figure 3.31: Normalized TGA mass loss for spent meso-porous and microporous zeolite-Y catalysts

Based on Figure 3.30 and 3.31, the meso-porosity of the zeolite-Y samples may have decreased the coking on/in the zeolite compared to the microporous zeolite-Y samples. This statement holds true for the 30:1 sample but not for the 15:1 sample; although the differences between the 15:1 samples may simply be within experimental error. Regardless, the microporous and meso-porous samples showed that a higher alumina to silica ratio (15:1) resulted in a greater amount of coking than a lower alumina to silica ratio (30:1). Much like the silica to alumina variations within the spent ZSM-5 catalysts, the observed trend agrees with the hypothesis that an increased number of acidic sites will result in an increased amount of coke¹¹⁰.

3.12.3.6 Pt-H-ZSM-5

TGA was conducted on the spent Pt-H-ZSM-5 sample discussed in section 2.5.3 Pt-H-ZSM-5 Synthesis Methodology and section 3.9 Pt-H-ZSM-5 vs. H-ZSM-5. This samples was tested at a reaction temperature of 450 °C, a catalyst to polyol ratio of 1:1, and a steam percentage of 20% in the carrier gas on the model PPG polyol. The total flow rate was 100 mL/min and the total polyol and catalyst mix added was 5 g.

The TGA displayed virtually no coke formation on/in the zeolite catalyst. Although this is in agreement with the literature regarding the addition of precious metals to ZSM-5,⁵¹ the TGA results cannot be taken conclusively. As previously discussed, the Pt-H-ZSM-5 resulted in very low product conversion compared to H-ZSM via the GC-MS total peak area methodology. Which means that the catalyst partook in very few catalytic cracking reactions overall, which would likely result in fewer coke deposits on/in the spent zeolite. Additionally, the spent catalyst, as shown in Figure 3.32, appears as a grey color. Given the color change from off-white to grey with very minimal catalytic interactions, there was likely catalyst deactivation that occurred during the calcination procedure or during the

reaction. This may be attributed to the grey color of the catalyst, which may have resulted from Pt particle formation. Sintering of Pt particles, as suggested by the grey color, may have resulted in the nearly complete deactivation of the catalyst.

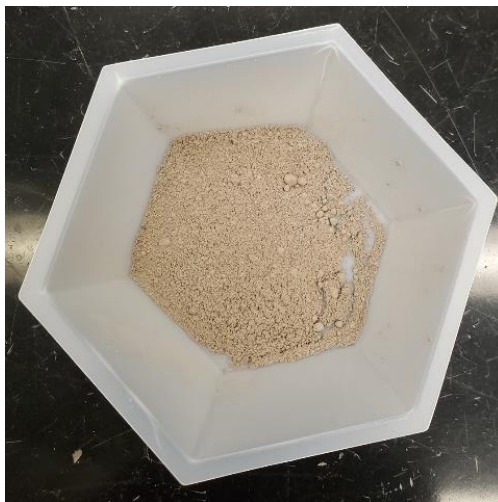


Figure 3.32: Spent Pt-H-ZSM-5 catalyst

3.12.4 PALS Spent ZSM-5 Characterization

PALS was conducted following the methodology discussed in section 2.4.6 Positron Annihilation Lifetime Spectroscopy (PALS). A total of four samples were characterized using PALS. The first sample was fresh ZSM-5, which was to act as the reference point. The second sample was ZSM-5 that had undergone a catalytic cracking reaction with polyurethane. The third sample was ZSM-5 that had undergone a catalytic cracking reaction with PPG. Fourth and final sample was a 5x reacted ZSM-5 sample with PPG, as previously discussed. Additionally, these catalysts had been reacted with 20% steam, a 2:1 catalyst to polyol ratio, and a reaction temperature of 260 °C. These experimentations were conducted on version 1.0 of the reactor system with a total flow rate of 25 mL/min and a total mixed catalyst and polyol mass of 1.5 g.

The PAL analysis was conducted in two regimes: “with” and “without” matrix correction effects, that take into account the contribution from the Na-22 source and the Ti thin cover. PAL results from both series of measurements, with source corrections, are presented in Table 3.10. The PAL values for the second series are highlighted in blue. The PAL results for the same samples are averaged and their standard deviation, along with the percentage standard error, are determined to remediate any outliers within the measurements. The last column includes values of the products with the longest lifetimes and intensities that are correlated with the ortho-Positronium pick-off annihilation, which is related to the micro-pore trapping size and intensity.

Table 3.10: PAL results for the four ZSM-5 samples with source correction

Sample	ID	τ_1	I_1	τ_2	I_2	τ_3	I_3
ZSM-5	48	0.151	26.11	0.500	64.52	2.7	9.37
	50	0.158	26.84	0.510	64.12	2.73	9.04
	123	0.157	31.66	0.479	57.96	2.68	10.38
	average	0.155	28.20	0.496	62.20	2.704	9.60
	stdeva	0.004	3.016	0.016	3.677	0.024	0.698
	rate	2.41%	9.53%	3.30%	6.34%	0.89%	6.73%
ZSM-5 polyurethane 1 run	51	0.155	30.25	0.437	56.15	2.081	13.6
	52	0.162	32.3	0.452	53.94	2.196	13.76
	54	0.161	32.77	0.457	53.36	2.26	13.87
	average	0.159	31.77	0.449	54.48	2.179	13.74
	stdeva	0.004	1.340	0.010	1.472	0.091	0.136
	rate	2.38%	4.22%	2.32%	2.70%	4.16%	0.99%
ZSM-5 polyprop. g. 1 run	55	0.162	28.38	0.488	62.55	2.58	9.07
	56	0.162	28.38	0.488	62.55	2.58	9.07
	57	0.174	30.85	0.496	61.14	2.52	8.01
	average	0.166	29.20	0.491	62.08	2.56	8.72
	stdeva	0.007	1.426	0.005	0.814	0.035	0.612
	rate	4.17%	4.88%	0.94%	1.31%	1.35%	7.02%
ZSM-5 polyprop. g. 5 runs	125	0.171	32.03	0.451	60.72	2.34	7.25
	127	0.162	36.17	0.448	56.96	2.32	6.87
	average	0.167	34.10	0.450	58.84	2.33	7.06
	stdeva	0.006	2.927	0.002	2.659	0.016	0.269
	rate	3.82%	8.58%	0.47%	4.52%	0.70%	3.81%

Based on Table 3.10, the PAL results vary from specimen to specimen, indicating changes due to the catalytic cracking, with the exception of the singularly reacted ZSM-5

polypropylene glycol sample. Regarding the results for fresh ZSM-5, the trapping and o-Ps pickoff lifetime values are consistent with the literature values for, with τ_2 at about 500 ns and $\tau_3 = 2.6\text{-}2.7$ ns range¹¹. The resulting PAL values for the reacted ZSM-5 with polyurethane are quite different than fresh ZSM-5, with trapping positronium lifetimes decreasing: $\tau_2 \sim 450$ ps and $\tau_3 = 2.179 \pm 0.091$ ns; however, the o-Ps annihilation fraction increased to 13.7% from 9.6 (± 0.7)%. A more concise summary of the results in Table 3.10 are displayed in Table 3.11.

Table 3.11: Average PAL results for the four ZSM-5 samples with source correction

Sample	τ_1	I_1	τ_2	I_2	τ_3	I_3	$\tau_3 \cdot I_3$
ZSM-5	0.155	28.203	0.496	62.200	2.704	9.597	25.953
ZSM-5*1 run polyurethane	0.159	31.773	0.449	54.483	2.179	13.743	29.947
ZSM-5*1 run polypropyl. g.	0.166	29.203	0.491	62.080	2.560	8.717	22.315
ZSM-5*5 r w/polypropyl. g.	0.167	34.100	0.450	58.840	2.329	7.060	16.439

According to Table 3.11, there are substantial changes between the fresh ZSM-5 sample and the polyurethane reacted ZSM-5 sample. In fact, these changes are significantly higher than the once reacted PPG ZSM-5 sample as well. The observed changes can be correlated with morphological changes and changes in the catalyst's structure due to coking. It is hypothesized that coking may result in filled void spaces in the microporous ZSM-5 samples due to a decrease in the longer lifetime PAL values for also samples. The ZSM-5 samples reacted with PPG also resulted in lower intensities for I_3 , which can be attributed to the filled void spaces due to coking. However, the ZSM-5 sample that reacted with polyurethane resulted in a large I_3 value compared to the fresh ZSM-5. It is hypothesized that this affect is due to the creation of addition smaller size voids due to

divisions within the existing voids; therefore, causing an increase in the I_3 intensity for the polyurethane reacted ZSM-5 sample. This phenomenon was also observed for the conversion of methanol-to-hydrocarbons (MTH) reaction using a ZSM-5 with silica gel catalyst¹¹².

Based on Table 3.11, the PAL values for ZSM-5 reacted once with PPG do not change substantially from fresh ZSM-5. After one reaction, the trapping site lifetimes (τ) resulted in changes less than 10%. Thus, a ZSM-5 sample that reacted a total of five times with PPG was investigated as well. The five times reacted sample resulted in more pronounced alterations in the PAL values due to morphological alterations and coking. However, the five times reacted ZSM-5 sample with PPG still resulted in less substantial changes to the PAL values compared to the polyurethane reacted ZSM-5 sample. This indicates that the structure of ZSM-5 is altered significantly faster in the polyurethane reaction compared to the PPG reaction. A more in-depth comparison of the changes within the samples is displayed in Table 3.12, where the relative change for $\tau_1 = (\tau_{1\text{sample}} - \tau_{1\text{ZSM}}) / \tau_{1\text{sample}}$. This calculation is repeated for all I and remaining τ values, as shown in Table 3.12.

Table 3.12: The relative change in PAL values compared to the fresh ZSM-5 sample

sample	T1	I1	T2	I2	T3	I3	T3*I3
ZSM-5 reference	0.155	28.203	0.496	62.200	2.704	9.597	25.953
ZSM-5*1 polyurethane	2.6%	12.7%	-9.6%	-12.4%	-19.4%	43.2%	15.4%
ZSM-5*1 polypropylene	6.9%	3.5%	-1.1%	-0.2%	-5.3%	-9.2%	-14.0%
ZSM-5*5 polypropylene	7.2%	20.9%	-9.4%	-5.4%	-13.9%	-26.4%	-36.7%

Table 3.12 also displays the direction of change within the reacted ZSM-5 samples. The singularly reacted PPG ZSM-5 sample resulted in changes within intensity and lifetime values of less than 10%. The five time reacted PPG ZSM-5 sample and the polyurethane

reacted ZSM-5 sample show far greater changes in PAL values. The most significant difference between the polyurethane reacted and the five times PPG reacted ZSM-5 samples is within their respective I_3 values. As previously discussed, an increase in the I_3 may be the result of an increase in the number of void spaces while a decrease in I_3 may be the result of coke buildup within these void spaces. This may also indicate permanent structural changes within the PPG reacted ZSM-5 sample, which would lead to permanent catalyst deactivation. These changes are also shown in Figure 3.33 for the most prominent PAL values (I_2 , I_3 , and τ_3).

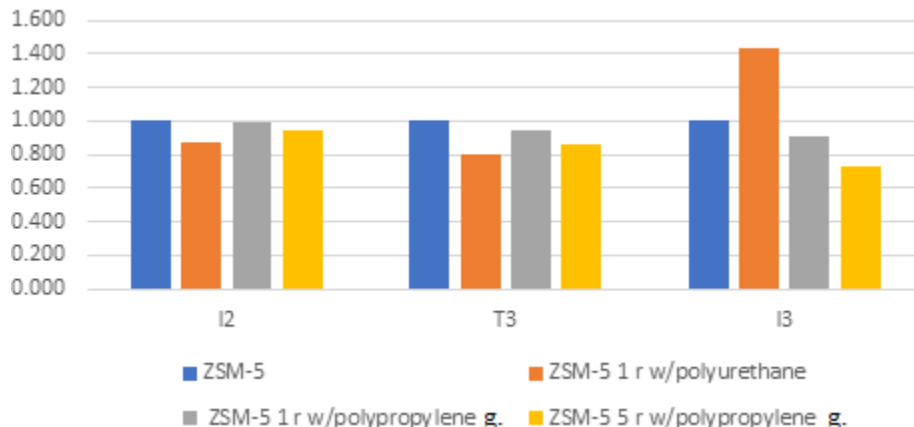


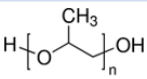
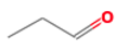

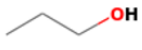
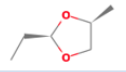
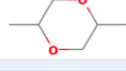
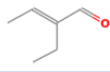

Figure 3.33: PAL results for the four ZSM-5 catalysts normalized to ZSM-5 for I_2 , τ_3 (T_3), and I_3

Figure 3.33 represents a histogram for the prominent PAL values (I_2 , I_3 , and τ_3) for the four ZSM-5 samples, which have all been normalized to the fresh ZSM-5 sample. Based Figure 3.33, there is very little evidence of change in the single reacted PPG ZSM-5 sample compared to ZSM-5; however, these changes are far more pronounced for the polyurethane and five times reacted PPG ZSM-5 samples for the potential reasons explained above.

3.13 General Reaction Pathway Discussion

Although the exact nature of catalytic cracking reaction of PPG is not well understood, a postulated discussion of said reaction, based on the reported results, would be appropriate. As such, the chemical structure of PPG and the seven primary products are displayed in Table 3.13¹¹³.

Table 3.13: The chemical formula and structure for PPG and the primary seven products¹¹³

Reactant/ Products	Chemical Formula	Chemical Structure
Polypropylene Glycol	$\text{H}[\text{C}_3\text{H}_6\text{O}]_n\text{OH}$	
Propionaldehyde	$\text{C}_3\text{H}_6\text{O}$	
Acetone	$\text{C}_3\text{H}_6\text{O}$	
1-Propanol	$\text{C}_3\text{H}_8\text{O}$	
1,3-Dioxolane, 2-ethyl-4-methyl-	$\text{C}_6\text{H}_{12}\text{O}_2$	
1,4-Dioxane, 2,5-dimethyl-	$\text{C}_6\text{H}_{12}\text{O}_2$	
2-Ethyl-trans-2-butenal	$\text{C}_6\text{H}_{10}\text{O}$	
Propylene Glycol	$\text{C}_3\text{H}_8\text{O}_2$	

Focusing on the chemical structure of the seven products, there are two distinct categories that can be observed: a product containing six carbon atoms and a product containing three carbon atoms. It is also interesting to note that the repeating unit within the PPG reactant contains three carbons as well. In fact, the repeating unit within PPG, acetone, and propionaldehyde are isomers of each other while 1,4-dioxane, 2,5-dimethyl

and 1,3-dioxolane, 2-ethyl-4-methyl are isomers of one another. The chemical formula for propylene glycol and 2-ethyl-trans-butenal are slightly different from the all the other compounds. Regarding the chemical structure, 1,4-dioxane, 2,5-dimethyl and 1,3-dioxolane, 2-ethyl-4-methyl both contain a ring-like structure, which have exactly two times the atomic elements as acetone and propionaldehyde, which both have a double bonded oxygen. The only other product compound with a double bond is 2-ethyl-trans-butenal, which has two double bonds.

Based on these chemical structures and the results, it is hypothesized that the repeating unit in polypropylene glycol may be directly converted into acetone by forming a double bond and rearranging the hydrogen atoms. However, this conversion may be limited to the pyrolytic cracking reaction only, as there is only a large selectivity of acetone during the thermal cracking reaction while minimal selectivity toward acetone during the catalytic cracking reaction. It has been shown that the pyrolytic cracking of monopropylene glycol results in the production of propylene oxide intermediate via dehydration, which is then converted to propionaldehyde and/or acetone⁶⁶. It is also interesting to note that the selectivity toward 1,4-dioxane, 2,5-dimethyl is high when the selectivity of propionaldehyde is high, this may indicate that polypropylene glycol can be converted into 1,4-dioxane, 2,5-dimethyl, which is cracked and converted to propionaldehyde. While in the thermal cracking reaction, there almost no 1,4-dioxane, 2,5-dimethyl, but there is a fair amount of 1,3-dioxolane, 2-ethyl-4-methyl. This may indicate that 1,3-dioxolane, 2-ethyl-4-methyl can also be cracked and converted acetone or propionaldehyde, depending on which carbon is cracked. Much like the postulated direct conversion of the repeating unit in PPG, it may be possible to directly convert said unit into propionaldehyde as well. It

may be a sort of regioselective reaction much like the hydroformylation reaction previously discussed⁸⁹⁻⁹⁴. 1-propanol was one of the most non-selective products for all catalytic and thermal cracking runs, except for the reaction where the gamma phase Al oxide acted as the catalyst. Given its chemical structure, 1-propanol may result from the cracking of 1,4-dioxane, 2,5-dimethyl or 1,3-dioxolane, 2-ethyl-4-methyl or the hydrogenation of propionaldehyde or even directly polypropylene glycol. Propylene glycol is likely from the cracked polypropylene glycol structure; it may also be possible that the PPG itself has a very small amount of monopropylene glycol, which would contribute to the overall selectivity of the propylene glycol product. 2-ethyl-trans-butenal saw a large increase in selectivity at a very high reaction temperature (760 °C), which indicates a large energy barrier requirement. 2-ethyl-trans-butenal is the only chemical product with a double bonded carbon and the only product with six carbons and a single oxygen atom. It is likely that 2-ethyl-trans-butenal is formed from the conversion of propionaldehyde, as pentanaldehyde has been shown to be converted into 2-ethyl-2-hexanal¹¹⁴. Figure 3.34 displays a more concise summary of this discussion. However, 1-propanol are not included due to the vast uncertainty of their reaction mechanisms.

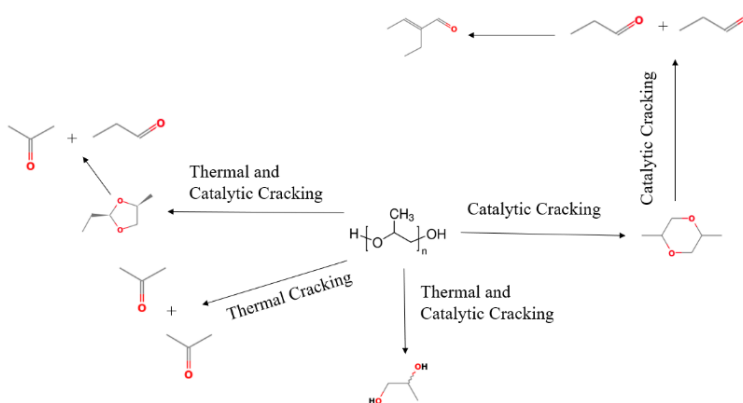


Figure 3.34: Proposed reaction mechanism of the catalytic and thermal cracking of polypropylene glycol

CHAPTER 4

CONCLUSIONS AND FUTURE DIRECTIONS

The work presented in this thesis explored the catalytic cracking reactions of waste polyol plastics. Given, the many issues with modern day recycling efforts, new and improved recycling methodologies are a necessity for environmental longevity. The primary objective of this project was to build a foundational platform for recyclability for overlooked plastics such as polyols and polyurethanes. Thus, initial reactor and analytical system development, reaction parameter optimization, and catalyst testing embody the bulk of the work discussed.

Initially, a reactor system was designed to facilitate the catalytic cracking of waste plastics through a fluidized bed reactor with a dual column GC analytical system. However, due to large issues in product recovery, the reactor system was redesigned a total of three times. The resulting final version of the reactor system is a semi-batch, plug flow reactor system with two condensers. The reactor is a vertically mounted, stainless steel tube that is encased by a furnace and loaded with a pre-mixed catalyst and polyol mixture. A carrier gas, which is comprised of a nitrogen and steam mixture, is flown through the reactor tube. The resulting product gas is then condensed through a series of two condensers. The first condenser operates to condense majority of the product and nearly all of the steam out of the system while the second condenser operates to condense out any remaining volatile products within the system. Using this setup, a mass balance closure of around 96-98% was achieved. Alongside the development of the reactor system, an analytical system was

modified and finalized. The resulting final version of the analytical system analyzed the liquid condensate via GC-MS. Additional analytical methods using LC-MS were also developed to investigate reactant conversion, as previously discussed.

Nearly all the experimental results discussed were produced using polypropylene glycol (PPG) Mn ~425 as the starting reactant polyol. PPG, alongside NH₄-ZSM-5 catalyst, served as model polyol and starting catalyst for this project. Using the developed reactor and analytical systems, seven primary products (propionaldehyde; 1,4-dioxane, 2,5-dimethyl; 1-propanol; 1,3-dioxolane, 2-ethyl-4-methyl; acetone; 2-ethyl-trans-2-butenal; and propylene glycol) that resulted from the catalytic cracking of PPG via a ZSM-5 catalyst were identified and calibrated for. Through an economic evaluation of these seven products, only propionaldehyde, 1-propanol, and propylene glycol were deemed economically feasible. However, given the selectivity of these products during preliminary testing, propionaldehyde was deemed to be the most realistic product to pursue further optimization of its selectivity.

The first step in selectivity optimization for propionaldehyde was an investigation of reaction parameter impact, such as the reaction temperature, the catalyst to polyol ratio, and the steam percentage in the carrier gas. After initial parameter experimentations, a Box-Behnken design of experiment (DOE) was employed to gather information regarding factor significance and co-factor interactions within the model. This design of experiment was conducted two times; however, the first time yielded no significant findings due to non-optimized reactor and analytical systems. The spent NH₄-ZSM-5 catalysts were tested via thermogravimetric analysis (TGA), diffuse reflectance for infrared Fourier transform spectroscopy (DRIFTS), and powder X-ray diffraction (PXRD). TGA and DRIFTS

concluded the evidence of coke on/in the zeolite catalyst due to the catalytic cracking reaction. PXRD also concluded that the catalyst was not losing crystallinity due to the reaction.

Prior to the second DOE, various catalysts such as zeolite Y, zeolite Beta Al oxide, and ZSM-5 were investigated. At the discussed conditions, NH_4 -ZSM-5 yielded a higher propionaldehyde selectivity than the other tested catalysts. However, Al oxide did result in a high selectivity toward 1-propanol, which was never further explored. TGA also yielded that NH_4 -ZSM-5 resulted in the least amount of coke buildup on/in the catalyst compared to the other tested catalysts.

Given the results of the various catalyst testing, NH_4 -ZSM-5 catalyst with different the silica to alumina ratios were tested. The NH_4 -ZSM-5 catalyst with a silica to alumina ratio of 50:1 resulted in the best propionaldehyde selectivity. It was shown that a low and high silica to alumina ratio did not lead to a substantial increase in selectivity of any of the products. Additionally, TGA of these catalysts showed a clear trend of an increased amount of coke for low silica to alumina ratios; thus, the higher the amount of alumina within the NH_4 -ZSM-5 sample, the greater the amount of coke within the sample.

Hierarchical meso-porous and microporous zeolite-Y samples with two different silica to alumina ratios were synthesized by UC Berkeley and tested in the reactor system for the discussed reaction. As it turns out, the meso-porous zeolite-Y samples significantly outperformed the microporous zeolite-Y samples. However, the silica to alumina ratio of 30:1 for both the meso-porous and microporous sample outperformed the 15:1 samples. In fact, the meso-porous 30:1 zeolite-Y sample outperformed the 50:1 ZSM-5 sample for propionaldehyde selectivity, making it the best catalyst tested thus far for this reaction.

Additionally, TGA resulted in more coking for the 15:1 samples compared to the 30:1 samples.

The second DOE conducted on this reaction concluded that temperature and temperature squared were the only statistically significant parameters within the model. Thus, the optimized conditions for this reaction were at a reaction temperature of 450 °C. Given the importance of temperature for this reaction, a relationship between the seven products and temperature was developed, which displayed many trends for various products.

Using the LC-MS methodology discussed, the selectivity was redefined to only compare the selectivity of the seven products rather than additional products. After this change, the thermal cracking of this reaction was investigated. The selectivity for acetone due to thermal cracking was extremely high, but the conversion was also around 18 times lower for the thermal cracking vs the catalytic cracking reaction with NH₄-ZSM-5.

Given the extensive usage of NH₄-ZSM-5 throughout the testing and optimization of this reaction, it was hypothesized that NH₄-ZSM-5 was converted into H-ZSM-5 during the reaction. This was proved by comparing the product selectivity of NH₄-ZSM-5 and H-ZSM-5, which yielded results all within experimental error. The H-ZSM-5 catalyst was also compared to Pt-H-ZSM-5. The Pt-H-ZSM-5 was hypothesized to potentially reduce the coke on/in the zeolite sample; however, due to the very low conversion of the Pt-H-ZSM-5, likely due to catalyst deactivation, this hypothesis was never tested. Synthesized MFI zeolite also showed significant promise with very high achievable selectivity's for propionaldehyde from this reaction.

The additional characterization of the ZSM-5 catalyst that had reacted with PPG and polyurethane was also tested using positron annihilation lifetime spectroscopy (PALS). PAL results indicated that the rate of structural changes within the catalyst was significantly higher for that of the polyurethane reaction compared to PPG. Additionally, the polyurethane reaction resulted in the partitioning of void spaces within the microporous structure due to coking and irreversible structure changes. However, the reaction with PPG results in the decrease of void space volume due to coking and reversal structural changes.

Based on these results, a brief discussion on the catalytic cracking mechanisms for this reaction was also presented. However, there are many more experimentations required before a definitive reaction mechanism can be proposed for the catalytic cracking of polypropylene glycol. Beyond additional characterization and spectroscopy experiments regarding mechanism concerns, additional zeolites with varying morphologies and porosities can be tested for this reaction. These different zeolites, such as 2-D MFI zeolites, may zeolite in significantly improved selectivity and conversion for this reaction.

Although briefly discussed, catalyst longevity will be primary concern for this reaction on an industrial scale application. Thus, additional experimentation regarding the longevity and revitalization of the catalyst involved in this reaction will be required. Reactivation of the catalyst due to coking may present degradation issues for the zeolite catalyst. Additionally, with the implementation of steam within this reaction, concerns regarding the dealumination of the zeolite catalyst may arise.

Lastly, PPG Mn ~425 acted as the model polyol for this reaction. Realistically, this reactant is likely considered an oligomer given its size. Thus, an investigation into longer

chain PPGs will be required for this reaction. Beyond just the size of polyol, testing of additional polyols and polyurethanes will also be of interest in future experimentations.

REFERENCES

1. Hahladakis, J. N., Iacovidou, E. & Gerassimidou, S. Plastic waste in a circular economy. in *Plastic Waste and Recycling* 481–512 (Elsevier, 2020). doi:10.1016/B978-0-12-817880-5.00019-0.
2. Geyer, R., Jambeck, J. R. & Law, K. L. *Production, use, and fate of all plastics ever made*. <http://advances.sciencemag.org/> (2017).
3. Garcia, J. M. & Robertson, M. L. The future of plastics recycling. *Science* **358**, (2017).
4. Shent, H., Pugh, R. J. & Forssberg, E. *A review of plastics waste recycling and the flotation of plastics*. vol. 25 (1999).
5. Royal Dutch Shell. Polyols. <https://www.shell.com/business-customers/chemicals/our-products/polyols.html>.
6. Garrido, M. A. & Font, R. Pyrolysis and combustion study of flexible polyurethane foam. *Journal of Analytical and Applied Pyrolysis* **113**, 202–215 (2015).
7. Dutta, A. S. Polyurethane Foam Chemistry. in *Recycling of Polyurethane Foams* 17–27 (Elsevier, 2018). doi:10.1016/b978-0-323-51133-9.00002-4.
8. Ragaert, K., Delva, L. & van Geem, K. Mechanical and chemical recycling of solid plastic waste. *Waste Management* **69**, 24–58 (2017).
9. van Bruggen, E. P. A., Koster, R. P., Picken, S. J. & Ragaert, K. Influence of Processing Parameters and Composition on the Effective Compatibilization of Polypropylene–Poly(ethylene terephthalate) Blends. *International Polymer Processing* **31**, (2016).
10. Singh, N. *et al.* Recycling of plastic solid waste: A state of art review and future applications. *Composites Part B: Engineering* **115**, 409–422 (2017).
11. Wong, S. L., Ngadi, N., Abdullah, T. A. T. & Inuwa, I. M. Current state and future prospects of plastic waste as source of fuel: A review. *Renewable and Sustainable Energy Reviews* vol. 50 1167–1180 (2015).

12. Tournier, V. *et al.* An engineered PET depolymerase to break down and recycle plastic bottles. *Nature* **580**, 216–219 (2020).
13. Tennakoon, A. *et al.* Catalytic upcycling of high-density polyethylene via a processive mechanism. *Nature Catalysis* **3**, 893–901 (2020).
14. López, A., de Marco, I., Caballero, B. M., Adrados, A. & Laresgoiti, M. F. Deactivation and regeneration of ZSM-5 zeolite in catalytic pyrolysis of plastic wastes. *Waste Management* **31**, 1852–1858 (2011).
15. Buekens, A. G. & Huang, H. Catalytic plastics cracking for recovery of gasoline-range hydrocarbons from municipal plastic wastes. *Resources, Conservation and Recycling* **23**, 163–181 (1998).
16. Blevins, J. L. & Martinez, K. A Political-Economic History of FCC Policy on Minority Broadcast Ownership. *The Communication Review* **13**, 216–238 (2010).
17. Vogt, E. T. C. & Weckhuysen, B. M. Fluid catalytic cracking: recent developments on the grand old lady of zeolite catalysis. *This journal is Cite this: Chem. Soc. Rev* **44**, 7342 (2015).
18. Biswas, J. & Maxwell, I. E. Recent process- and catalyst-related developments in fluid catalytic cracking. *Applied Catalysis* vol. 63 197–258 (1990).
19. Armor, J. N. New catalytic technology commercialized in the USA during the 1980's. *Applied Catalysis* vol. 78 141–173 (1991).
20. Vogt, E. T. C., Whiting, G. T., Dutta Chowdhury, A. & Weckhuysen, B. M. Zeolites and zeotypes for oil and gas conversion. in *Advances in Catalysis* vol. 58 143–314 (Academic Press Inc., 2015).
21. Rodríguez, E. *et al.* Fuel production by cracking of polyolefins pyrolysis waxes under fluid catalytic cracking (FCC) operating conditions. *Waste Management* **93**, 162–172 (2019).
22. Ali, M. F. & Siddiqui, M. N. Thermal and catalytic decomposition behavior of PVC mixed plastic waste with petroleum residue. in *Journal of Analytical and Applied Pyrolysis* vol. 74 282–289 (Elsevier, 2005).
23. Wong, S. L., Ngadi, N., Abdullah, T. A. T. & Inuwa, I. M. Current state and future prospects of plastic waste as source of fuel: A review. *Renewable and Sustainable Energy Reviews* vol. 50 1167–1180 (2015).

24. Pinho, A. de R. *et al.* Fast pyrolysis oil from pinewood chips co-processing with vacuum gas oil in an FCC unit for second generation fuel production. *Fuel* **188**, 462–473 (2017).
25. Xing, C. *et al.* Hierarchical zeolite y supported cobalt bifunctional catalyst for facilely tuning the product distribution of Fischer-Tropsch synthesis. *Fuel* **148**, 48–57 (2015).
26. Sartipi, S. *et al.* Hierarchical H-ZSM-5-supported cobalt for the direct synthesis of gasoline-range hydrocarbons from syngas: Advantages, limitations, and mechanistic insight. *Journal of Catalysis* **305**, 179–190 (2013).
27. Jae, J. *et al.* Investigation into the shape selectivity of zeolite catalysts for biomass conversion. *Journal of Catalysis* **279**, 257–268 (2011).
28. Gaffney, A. & Jones, A. Process for Treating Polyether Polyols. (1995).
29. Muhammad, C., Onwudili, J. A. & Williams, P. T. Catalytic pyrolysis of waste plastic from electrical and electronic equipment. *Journal of Analytical and Applied Pyrolysis* **113**, 332–339 (2015).
30. Li, Y., Chung, T. S., Cao, C. & Kulprathipanja, S. The effects of polymer chain rigidification, zeolite pore size and pore blockage on polyethersulfone (PES)-zeolite A mixed matrix membranes. *Journal of Membrane Science* **260**, 45–55 (2005).
31. Weitkamp, J. Zeolites and catalysis. *Solid State Ionics* **131**, 175–188 (2000).
32. Tao, Y., Kanoh, H., Abrams, L. & Kaneko, K. Mesopore-Modified Zeolites: Preparation, Characterization, and Applications. (2006) doi:10.1021/cr040204o.
33. Lago, R. M. *et al.* The nature of the catalytic sites in HZSM-5 - Activity enhancement. in *Studies in Surface Science and Catalysis* vol. 28 677–684 (Elsevier Inc., 1986).
34. Greensfelder, B. S., Voge, H. & Good, G. M.). (26) *Ibid.*, 2,416. *J. Am. Chem. Soc* vol. 2 <https://pubs.acs.org/sharingguidelines> (1941).
35. Dupain, X., Makkee, M. & Moulijn, J. A. Optimal conditions in fluid catalytic cracking: A mechanistic approach. *Applied Catalysis A: General* **297**, 198–219 (2006).
36. Corma, A. & Orchillés, A. v. Current views on the mechanism of catalytic cracking. *Microporous and Mesoporous Materials* **35–36**, 21–30 (2000).

37. Kotrel, S., Knözinger, H. & Gates, B. C. The Haag-Dessau mechanism of protolytic cracking of alkanes. *Microporous and Mesoporous Materials* **35–36**, 11–20 (2000).
38. Corma, A., Planelles, J., Sánchez-Marín, J. & Tomás, F. The role of different types of acid site in the cracking of alkanes on zeolite catalysts. *Journal of Catalysis* **93**, 30–37 (1985).
39. Kazansky, V. B. The Catalytic Site from a Chemical Point of View. in *Studies in Surface Science and Catalysis* vol. 85 251–272 (Elsevier, 1994).
40. Xue, N. *et al.* Understanding the enhancement of catalytic performance for olefin cracking: Hydrothermally stable acids in P/HZSM-5. *Journal of Catalysis* **248**, 20–28 (2007).
41. Liu, S., Ohnishi, R. & Ichikawa, M. Promotional role of water added to methane feed on catalytic performance in the methane dehydroaromatization reaction on Mo/HZSM-5 catalyst. *Journal of Catalysis* **220**, 57–65 (2003).
42. Depeyre, D., Flicoteaux, C. & Chardalre, C. *Kirk-Othmer's Encyclopedia of Chemical Technology-Supplementary Edition. Ialso, S. B. Water Resour. Res* vol. 24 <https://pubs.acs.org/sharingguidelines> (1985).
43. Bhat, Y. S., Das, J., Rao, K. v. & Halgeri, A. B. Inactivation of external surface of ZSM-5: Zeolite morphology, crystal size, and catalytic activity. *Journal of Catalysis* **159**, 368–374 (1996).
44. OLSON, D. H. & HAAG, W. O. Structure-Selectivity Relationship in Xylene Isomerization and Selective Toluene Disproportionation. in 275–307 (1984). doi:10.1021/bk-1984-0248.ch014.
45. Meshram, N. R., Hegde, S. G. & Kulkarni, S. B. Active sites on ZSM-5 zeolites for toluene disproportionation. *Zeolites* **6**, 434–438 (1986).
46. Uguina, M. A., Sotelo, J. L. & Serrano, D. P. Toluene disproportionation over ZSM-5 zeolite. Effects of crystal size, silicon-to-aluminum ratio, activation method and pelletization. *Applied Catalysis* **76**, 183–198 (1991).
47. Sriningsih, W. *et al.* Fuel Production from LDPE Plastic Waste over Natural Zeolite Supported Ni, Ni-Mo, Co and Co-Mo Metals. *Procedia Environmental Sciences* **20**, 215–224 (2014).
48. Ratnasari, D. K., Nahil, M. A. & Williams, P. T. Catalytic pyrolysis of waste plastics using staged catalysis for production of gasoline range hydrocarbon oils. *Journal of Analytical and Applied Pyrolysis* **124**, 631–637 (2017).

49. Al-Shammari, A. A. *et al.* Catalytic cracking of heavy naphtha-range hydrocarbons over different zeolites structures. *Fuel Processing Technology* **122**, 12–22 (2014).
50. Durmuş, A., Koç, S. N., Pozan, G. S. & Kaşgöz, A. Thermal-catalytic degradation kinetics of polypropylene over BEA, ZSM-5 and MOR zeolites. *Applied Catalysis B: Environmental* **61**, 316–322 (2005).
51. Kim, S., Sasmaz, E. & Lauterbach, J. Effect of Pt and Gd on coke formation and regeneration during JP-8 cracking over ZSM-5 catalysts. *Applied Catalysis B: Environmental* **168–169**, 212–219 (2015).
52. Wan, Z., Li, G. K., Wang, C., Yang, H. & Zhang, D. Relating coke formation and characteristics to deactivation of ZSM-5 zeolite in methanol to gasoline conversion. *Applied Catalysis A: General* **549**, 141–151 (2018).
53. Triantafillidis, C. S., Vlessidis, A. G., Nalbandian, L. & Evmiridis, N. P. Effect of the degree and type of the dealumination method on the structural, compositional and acidic characteristics of H-ZSM-5 zeolites. *Microporous and Mesoporous Materials* **47**, 369–388 (2001).
54. Corma, A., Fornés, V., Martínez-Triguero, J. & Pergher, S. B. Delaminated zeolites: Combining the benefits of zeolites and mesoporous materials for catalytic uses. *Journal of Catalysis* **186**, 57–63 (1999).
55. Groen, J. C., Moulijn, J. A. & Pérez-Ramírez, J. Decoupling mesoporosity formation and acidity modification in ZSM-5 zeolites by sequential desilication-dealumination. *Microporous and Mesoporous Materials* **87**, 153–161 (2005).
56. Yan, Z. *et al.* On the acid-dealumination of USY zeolite: A solid state NMR investigation. *Journal of Molecular Catalysis A: Chemical* **194**, 153–167 (2003).
57. Wouters, B. H., Chen, T.-H. & Grobet, P. J. Reversible Tetrahedral–Octahedral Framework Aluminum Transformation in Zeolite Y. *Journal of the American Chemical Society* **120**, (1998).
58. Peters, A. W. & Wu, C. C. Selectivity effects of a new aluminum species in strongly dealuminated USY containing FCC catalysts. *Catalysis Letters* **30**, (1995).
59. Borade, R., Sayari, A., Adnot, A. & Kaliaguine, S. *Characterization of Acidity in ZSM-5 Zeolites: An X-ray Photoelectron and IR Spectroscopy Study*. *J. Phys. Chem* vol. 94 <https://pubs.acs.org/sharingguidelines> (1990).
60. Naranov, E. R., Sadovnikov, A. A., Vatsouro, I. M. & Maximov, A. L. The mechanism of promoter-induced zeolite nanosheet crystallization under

hydrothermal and microwave irradiation conditions. *Inorganic Chemistry Frontiers* **7**, (2020).

61. Zhang, Y., Xia, Z., Huang, H. & Chen, H. Thermal degradation of polyurethane based on IPDI. *Journal of Analytical and Applied Pyrolysis* **84**, 89–94 (2009).
62. Font, R., Fullana, A., Caballero, J. A., Candela, J. & García, A. Pyrolysis study of polyurethane. *Journal of Analytical and Applied Pyrolysis* **58–59**, 63–77 (2001).
63. Ballistreri, A., Foti, S., Maravigna, P., Montaudo, G. & Scamporrino, E. Mechanism of thermal degradation of polyurethanes investigated by direct pyrolysis in the mass spectrometer. *Journal of Polymer Science: Polymer Chemistry Edition* **18**, (1980).
64. Lattimer, R. P., Polce, M. J. & Wesdemiotis, C. MALDI-MS analysis of pyrolysis products from a segmented polyurethane. *Journal of Analytical and Applied Pyrolysis* **48**, 1–15 (1998).
65. Garrido, M. A., Font, R. & Conesa, J. A. Pollutant emissions during the pyrolysis and combustion of flexible polyurethane foam. *Waste Management* **52**, 138–146 (2016).
66. Laino, T. *et al.* Mechanisms of Propylene Glycol and Triacetin Pyrolysis. (2012) doi:10.1021/jp300997d.
67. Naranov, E. R., Sadovnikov, A. A., Vatsouro, I. M. & Maximov, A. L. The mechanism of promoter-induced zeolite nanosheet crystallization under hydrothermal and microwave irradiation conditions. *Inorganic Chemistry Frontiers* **7**, (2020).
68. Choi, M. *et al.* Stable single-unit-cell nanosheets of zeolite MFI as active and long-lived catalysts. **461**, (2009).
69. Ni, Y. *et al.* Preparation of hierarchical mesoporous Zn/HZSM-5 catalyst and its application in MTG reaction. *Journal of Natural Gas Chemistry* **20**, 237–242 (2011).
70. Wei, R., Yang, H., Scott, J. A., Aguey-Zinsou, K.-F. & Zhang, D. Synthesis of 2D MFI zeolites in the form of self-interlocked nanosheet stacks with tuneable structural and chemical properties for catalysis. *Applied Materials Today* **11**, 22–33 (2018).
71. Omais, B. Is Water Safe To Inject In Gas Chromatography? - Science Unfiltered - Phenomenex. (2018).

72. Fogler, H. S. *Elements of Chemical Reaction Engineering*. (Pearson, 2016).
73. Park, M. *et al.* Practical Challenges Associated with Catalyst Development for the Commercialization of Li-air Batteries. *Journal of Electrochemical Science and Technology* **5**, 1–18 (2014).
74. Ross, J. R. H. Mass and Heat Transfer Limitations and Other Aspects of the Use of Large-Scale Catalytic Reactors. in *Contemporary Catalysis* 187–213 (Elsevier, 2019). doi:10.1016/B978-0-444-63474-0.00008-4.
75. Brown, R. L. & Stein, S. E. “Boiling Point Data.” in *NIST Chemistry WebBook, NIST Standard Reference Database Number 69* (eds. Linstrom, P. J. & Mallard, W. G.) vol. 69 (National Institute of Standards and Technology, 2022).
76. ZSM-5 (CBV 5524G). (2014).
77. Wolf, E. E. & Alfani, F. Catalysts Deactivation by Coking. *Catalysis Reviews* **24**, (1982).
78. Wang, C. *et al.* Integrated harvest of phenolic monomers and hydrogen through catalytic pyrolysis of biomass over nanocellulose derived biochar catalyst. *Bioresource Technology* **320**, 124352 (2021).
79. Jean, Y. C., Mallon, P. E. & Schrader, D. M. *Principles and Applications of Positron and Positronium Chemistry*. (WORLD SCIENTIFIC, 2003). doi:10.1142/5086.
80. TechnoAP. Digital Positron Annihilation Lifetime Measurement System.
81. Kansy, J. Microcomputer program for analysis of positron annihilation lifetime spectra. *Nuclear Instruments and Methods in Physics Research Section A: Accelerators, Spectrometers, Detectors and Associated Equipment* **374**, 235–244 (1996).
82. Meng, L., Mezari, B., Goesten, M. G. & Hensen, E. J. M. One-Step Synthesis of Hierarchical ZSM-5 Using Cetyltrimethylammonium as Mesopore and Structure-Directing Agent. *Chemistry of Materials* **29**, (2017).
83. Markets and Markets. *Propylene Glycol Market by Source (Petroleum-based, Bio-based), Grade (Industrial, Pharmaceutical), End-use Industry (Transportation, Building & Construction, Food & Beverage, Pharmaceuticals, Cosmetics & Personal Care), Region - Global Forecast to 2024*. (2020).
84. Expert Market Research. *Global Propionaldehyde Market to Grow at a Healthy Pace During 2021-2026, Aided by the Growing R&D Activities*.

85. Grand View Research. *Propanol Market Size, Share & Trends Analysis Report By Product (N-propanol, Isopropyl Alcohol), By Region (North America, Europe, APAC, CSA, MEA), And Segment Forecasts, 2020 - 2027*. (2020).
86. Fernández, L. *Market value of acetone worldwide from 2015 to 2020, with a forecast for 2021 to 2026*. (2021).
87. Franke, R., Selent, D. & Börner, A. Applied Hydroformylation. *Chemical Reviews* **112**, 5675–5732 (2012).
88. Gellrich, U., Seiche, W., Keller, M. & Breit, B. Mechanistic Insights into a Supramolecular Self-Assembling Catalyst System: Evidence for Hydrogen Bonding during Rhodium-Catalyzed Hydroformylation. *Angewandte Chemie International Edition* **51**, 11033–11038 (2012).
89. Bohnen, H.-W. & Cornils, B. Hydroformylation of alkenes: An industrial view of the status and importance. in 1–64 (2002). doi:10.1016/S0360-0564(02)47005-8.
90. Hou, C. *et al.* Hydroformylation of alkenes over rhodium supported on the metal-organic framework ZIF-8. *Nano Research* **7**, 1364–1369 (2014).
91. Wang, Y. *et al.* Heterogeneous Rh/CPOL-BP&P(OPh)₃ catalysts for hydroformylation of 1-butene: The formation and evolution of the active species. *Journal of Catalysis* **368**, 197–206 (2018).
92. Zhang, J. *et al.* Enhancing regioselectivity via tuning the microenvironment in heterogeneous hydroformylation of olefins. *Journal of Catalysis* **387**, 196–206 (2020).
93. Amsler, J. *et al.* Prospects of Heterogeneous Hydroformylation with Supported Single Atom Catalysts. *Journal of the American Chemical Society* **142**, 5087–5096 (2020).
94. Alsalahi, W. & Trzeciak, A. M. Rhodium-catalyzed hydroformylation under green conditions: Aqueous/organic biphasic, “on water”, solventless and Rh nanoparticle based systems. *Coordination Chemistry Reviews* **430**, 213732 (2021).
95. Siva Kumar, V. *et al.* Role of acidic and basic sites of Al₂O₃ in predicting the reaction pathway of isophorone transformation. *Journal of Molecular Catalysis A: Chemical* **223**, 283–288 (2004).
96. Denayer, J. F., Souverijns, W., Jacobs, P. A., Martens, J. A. & Baron, G. v. High-Temperature Low-Pressure Adsorption of Branched C₅–C₈ Alkanes on Zeolite Beta, ZSM-5, ZSM-22, Zeolite Y, and Mordenite. *The Journal of Physical Chemistry B* **102**, 4588–4597 (1998).

97. HUANG, H., ZHU, H., ZHANG, S., ZHANG, Q. & LI, C. Effect of silicon to aluminum ratio on the selectivity to propene in methanol conversion over H-ZSM-5 zeolites. *Journal of Fuel Chemistry and Technology* **47**, 74–82 (2019).
98. Fu, D. *et al.* Uniformly Oriented Zeolite ZSM-5 Membranes with Tunable Wettability on a Porous Ceramic. *Angewandte Chemie International Edition* **57**, 12458–12462 (2018).
99. Kunkeler, P. J. *et al.* Zeolite Beta: The Relationship between Calcination Procedure, Aluminum Configuration, and Lewis Acidity. *Journal of Catalysis* **180**, 234–244 (1998).
100. RAJADHYAKSHA, R. Activation of ZSM-5 catalysts. *Journal of Catalysis* **63**, 510–514 (1980).
101. NAYAK, V. Acid strength distribution and catalytic properties of H-ZSM-5: Effect of deammoniation conditions of NH₄-ZSM-5. *Journal of Catalysis* **81**, 26–45 (1983).
102. Bourgeat-Lami, E. *et al.* Study of the state of aluminium in zeolite- β . *Applied Catalysis* **72**, 139–152 (1991).
103. Zhang, L., Luo, X., Qin, Y. & Li, Y. A novel 2,5-furandicarboxylic acid-based bis(cyclic carbonate) for the synthesis of biobased non-isocyanate polyurethanes. *RSC Advances* **7**, 37–46 (2017).
104. Wragg, D. S., Grønvold, A., Voronov, A., Norby, P. & Fjellvåg, H. Combined XRD and Raman studies of coke types found in SAPO-34 after methanol and propene conversion. *Microporous and Mesoporous Materials* **173**, 166–174 (2013).
105. Dostert, K.-H., O'Brien, C. P., Mirabella, F., Ivars-Barceló, F. & Schauermaun, S. Adsorption of acrolein, propanal, and allyl alcohol on Pd(111): a combined infrared reflection–absorption spectroscopy and temperature programmed desorption study. *Physical Chemistry Chemical Physics* **18**, (2016).
106. Solomon, P. R. & Carangelo, R. M. FT-i.r. analysis of coal. 2. Aliphatic and aromatic hydrogen concentration. *Fuel* **67**, 949–959 (1988).
107. Cerqueira, H. S., Ayrault, P., Datka, J. & Guisnet, M. Influence of coke on the acid properties of a USHY zeolite. *Microporous and Mesoporous Materials* **38**, 197–205 (2000).

108. Trejo, F., Rana, M. S. & Ancheyta, J. Thermogravimetric determination of coke from asphaltenes, resins and sediments and coking kinetics of heavy crude asphaltenes. *Catalysis Today* **150**, 272–278.
109. VILLEGAS, J. *et al.* Isomerization of n-butane to isobutane over Pt-modified Beta and ZSM-5 zeolite catalysts: Catalyst deactivation and regeneration. *Chemical Engineering Journal* **120**, 83–89 (2006).
110. Yu, X., Liu, B. & Zhang, Y. Effect of Si/Al ratio of high-silica HZSM-5 catalysts on the prins condensation of isobutylene and formaldehyde to isoprene. *Heliyon* **5**, e01640 (2019).
111. Dutta, D., Sachdeva, A. & Pujari, P. K. Positron annihilation studies on the phase transition of benzene and reactivity of nitrobenzene in confined framework of ZSM-5 zeolite. *Chemical Physics Letters* **432**, 116–121 (2006).
112. Taylor, C. N. *et al.* Catalyst Deactivation Probed by Positron Annihilation Spectroscopy. *ACS Catalysis* **11**, 14967–14976 (2021).
113. Stein, S. E. & Brown, R. L. “Structures and Propeties Group Additivity Model.” in *NIST Chemistry WebBook, NIST Standard Reference Database Number 69* vol. 69 (National Institute of Standards and Technology, 2022).
114. Kruse, A., Bernolle, P., Dahmen, N., Dinjus, E. & Maniam, P. Hydrothermal gasification of biomass: consecutive reactions to long-living intermediates. *Energy Environ. Sci.* **3**, 136–143 (2010).